A Study on Convective Turbulent Dust Dry Deposition:

Parameterization and Application

Inaugural Dissertation

zur

Erlangung des Doktorgrades

der Mathematisch-Naturwissenschaftlichen Fakulät

der Universität zu Köln

vorgelegt von

Xin Yin

aus Shangqiu, China

Köln 2023

BERICHTERSTATTER:

PROF. DR. YAPING SHAO

PROF. DR. ROEL NEGGERS

Abstract

Current dust deposition schemes rarely consider the influence of atmospheric boundary layer (ABL) stability. However, it is increasingly recognized that ABL stability plays an important role in the dry deposition process of dust particles. Specifically, the deposition velocity is found to be greatly enhanced under convective conditions. The cause for this enhancement is not completely understood. This thesis aims to investigate why dust deposition velocity is affected by ABL stability and enhanced under convective conditions, and how these effects can be parameterized and incorporated into the dust deposition scheme.

To achieve the goals, this thesis presents a WRF-LES/D that couples the Weather Research and Forecasting (WRF) Model in its large-eddy simulation (LES) mode with the dust deposition scheme of Zhang and Shao (2014) (ZS14). The ZS14 scheme is physics-based, developed and calibrated using wind-tunnel experimental data. WRF-LES/D is then applied to investigate the deposition process under different surface-heat-flux and friction-velocity conditions. The high-resolution atmospheric flow is simulated using WRF-LES, and the convective diffusion process of dust is represented using a coupled Chemistry (WRF-Chem) module, while the deposition velocity is calculated using the ZS14 scheme.

The simulations indicate that deposition velocity depends on ABL stability as it is determined by the local vertical momentum flux (or shear stress), which is a stochastic quantity with statistical moments depending on ABL stability. The effects of ABL stability on particle deposition are most obvious for particles in the size range of 0.04 to 5 μm and can be estimated by considering instantaneous aerodynamic shear stress in the dust deposition scheme. Statistical analysis of the simulation results shows that the probability distribution of instantaneous aerodynamic shear stress can be well expressed as a Weibull distribution. The shape and scale parameters of this distribution can be described in terms of regional friction velocity and vertical scaling velocity. On this basis, a new dust deposition scheme is proposed. This scheme includes an ABL stability correction by introducing a shear stress distribution into the ZS14 scheme. The new dust deposition scheme is validated using measurements and WRF-LES/D predictions. The new scheme exhibits a relative difference of approximately 12% in settling velocities compared to the numerical experiments, whereas the original ZS14 scheme shows a relative difference of around 50% when compared to the numerical experiments. Finally, we apply both the ZS14 scheme and the newly developed scheme to regional-scale dust simulations. It is found that with the new deposition scheme, a greater amount of dust deposition is predicted in the near field, accompanied by lower dust concentration in the atmosphere in the far field. This work constitutes a further progression in the development of deposition schemes that account for the stochastic nature of the deposition process. The results hold notable implications for refining the accuracy of predictions pertaining to the dust cycle, spanning across both regional and global scales.

Kurzfassung

Aktuelle Staubablagerungsschemata berücksichtigen selten den Einfluss der Stabilität der atmosphärischen Grenzschicht (ABL). Es wird jedoch zunehmend erkannt, dass die ABL-Stabilität eine wichtige Rolle im Trockenablagerungsprozess von Staubpartikeln spielt. Insbesondere wird festgestellt, dass die Ablagerungsgeschwindigkeit unter konvektiven Bedingungen erheblich erhöht ist. Die Ursache für diese Steigerung ist noch nicht vollständig verstanden. Diese Arbeit zielt darauf ab zu untersuchen, warum die Staubablagerungsgeschwindigkeit von der ABL-Stabilität beeinflusst wird und unter konvektiven Bedingungen verstärkt ist, sowie wie diese Effekte parametrisiert und in das Staubablagerungsschema integriert werden können.

Um diese Ziele zu erreichen, präsentiert diese Arbeit ein WRF-LES/D, das das Weather Research and Forecasting (WRF) Model im Modus der Large-Eddy-Simulation (LES) mit dem Staubablagerungsschema von Zhang und Shao (2014) (ZS14) koppelt. Das ZS14 Schema basiert auf physikalischen Prinzipien, wurde entwickelt und mit Windkanalexperimenten kalibriert. WRF-LES/D wird dann angewendet, um den Ablagerungsprozess unter verschiedenen Bedingungen von Oberflächen-Wärmefluss und Reibungsgeschwindigkeit zu untersuchen. Die hochauflösende atmosphärische Strömung wird mit WRF-LES simuliert, und der konvektive Diffusionsprozess von Staub wird mithilfe eines gekoppelten Chemie-Moduls (WRF-Chem) dargestellt, während die Ablagerungsgeschwindigkeit mithilfe des ZS14-Schemas berechnet wird.

Die Simulationen zeigen, dass die Ablagerungsgeschwindigkeit von der ABL-Stabilität abhängt, da sie durch den lokalen vertikalen Impulsfluss (oder Scherspannung) bestimmt wird, der eine stochastische Größe mit statistischen Momenten ist, die von der ABL-Stabilität abhängen. Die Auswirkungen der ABL-Stabilität auf die Partikelablagerung sind besonders deutlich für Partikel im Größenbereich von 0,04 bis 5 µm und können geschätzt werden, indem der momentane aerodynamische Scherstress im Staubablagerungsschema berücksichtigt wird. Statistische Analysen der Simulationsergebnisse zeigen, dass die Wahrscheinlichkeitsverteilung des momentanen aerodynamischen Scherstresses gut durch eine Weibull-Verteilung ausgedrückt werden kann. Die Form- und Skalenparameter dieser Verteilung können in Bezug auf die regionale Reibungsgeschwindigkeit und die vertikale Skalierungsgeschwindigkeit

beschrieben werden. Auf dieser Grundlage wird ein neues Staubablagerungsschema vorgeschlagen. Dieses Schema umfasst eine ABL-Stabilitätskorrektur, indem eine Scherspannungsverteilung in das ZS14-Schema eingeführt wird. Das neue Staubablagerungsschema wird mit Messungen und WRF-LES/D-Vorhersagen validiert. Das neue Schema weist eine relative Abweichung von etwa 12% in den Setzgeschwindigkeiten im Vergleich zu den numerischen Experimenten auf, während das ursprüngliche ZS14-Schema eine relative Abweichung von etwa 50% im Vergleich zu den numerischen Experimenten zeigt.

Schließlich wenden wir sowohl das ZS14-Schema als auch das neu entwickelte Schema auf regional-skalige Staubsimulationen an. Es wird festgestellt, dass mit dem neuen Ablagerungsschema eine größere Menge an Staubablagerung im Nahbereich vorhergesagt wird, begleitet von einer geringeren Staubkonzentration in der Atmosphäre im Fernbereich. Diese Arbeit stellt eine weitere Fortentwicklung in der Entwicklung von Ablagerungsschemata dar, die die stochastische Natur des Ablagerungsprozesses berücksichtigen. Die Ergebnisse haben bemerkenswerte Auswirkungen auf die Verbesserung der Genauigkeit von Vorhersagen im Zusammenhang mit dem Staubkreislauf, die sich über regionale und globale Maßstäbe erstrecken.

Contents

1. Introduction

Atmospheric dust plays a crucial role in the Earth system for reasons such as aerosol-radiation and aerosol-cloud interactions (Boucher et al., 2013; Rosenfeld et al., 2001; Tegen and Lacis, 1996). The scattering and absorption of shortwave radiation, as well as the re-emission of longwave radiation by aerosols, may result in changes in atmospheric radiative forcing (Heinold et al., 2011; Sokolik and Toon, 1996). Due to their small sizes, typically less than 20 μm in diameter (Zhang, 2013), dust particles are easily mixed into atmospheric turbulence and thus penetrate the planetary boundary layer, and then transported by wind to locations several thousand kilometers away from the source region (Shao, 2008). The transported dust particles are then deposited back to the ground through wet deposition (precipitation washout) and dry deposition, forming a part of the dust cycle (Shao et al., 2011a). Dry deposition is the removal of particulates and gases (here focusing on dust) at the air-surface interface by turbulent transfer and gravitational settling (Droppo, 2006; Hicks et al., 2016; Sehmel, 1980). Dry deposition constitutes a significant fraction of the total deposition, occasionally exceeding fifty percent (Lovett, 1994). The effects of dust deposition are manifold, for example, the deposition of dust-borne phosphorus is critical for ecosystem productivity (i.e., primary biomass production), as the long-term productivity of many land ecosystems is limited by the availability of phosphorus (Okin et al., 2004). It is hypothesized that the supply of bioavailable iron by dust deposition is an important control on ocean productivity (Jickells et al., 2005), as many marine biotas are iron-dependent (Martin et al., 1994). Furthermore, the stimulation of terrestrial and marine ecosystem productivity by dust deposition also affects the biogeochemical cycle of carbon and nitrogen (Mahowald et al., 2009), and thus, it has been suggested that changes in atmospheric CO_2 concentrations between glacial and interglacial periods (Broecker and Henderson, 1998; Martin et al., 1994) and over the past century (Mahowald et al., 2009) have been attributed to changes in global dust deposition on ecosystems.

1.1 Limitations of dust deposition models

Dry deposition is commonly characterized by the bulk deposition velocity (Chamberlain, 1953), the ratio of the vertical flux F_d through a horizontal plane in the air to the concentration at the same height, $c(z)$ (for height z), i.e., $V_d = F_d / c(z)$. Since the early 1940s, numerous experimental (Chamberlain, 1967; Damay, 2010; Gregory, 1945; Wesely et al., 1983, 1985a) and theoretical (Seinfeld et al., 2016; Slinn and Slinn, 1980; Slinn, 1982; Walcek and Taylor, 1986; Zhang and Shao, 2014; Zhang et al., 2001) studies have mostly focused on dry deposition (Chamberlain, 1967; Gregory, 1945; Petroff and Zhang, 2010; Seinfeld et al., 2016; Slinn and Slinn, 1980; Slinn, 1982; Walcek et al., 1986; Zhang and Shao, 2014). Existing models describing particle deposition are divided into two categories: bulk resistance models (Hicks et al., 1987; Voldner and Sirois, 1986; Wesely et al., 1983, 1985b) and process-oriented models (Davidson et al., 1982; Hummelshøj et al., 1992; Peters and Eiden, 1992; Slinn and Slinn, 1980; Slinn, 1982; Williams, 1982). The former models, commonly used for gas deposition, are extended to particle deposition over the entire particle size range. These models are derived from limited experimental data sets, and express particle deposition velocity in terms of micrometeorological concepts (e.g., friction velocity and atmospheric stability). Particle size is not considered in these models. The process-oriented models are based on a removal process described by mathematical relationships that give deposition velocity for different particle sizes. All particle collecting mechanisms, including turbulent transport, sedimentation, impaction, interception, Brownian diffusion, rebound, and hygroscopic growth, are to be included in such models. Some of the models are validated against wind-tunnel measurements, and, therefore, typically address neutral atmospheric conditions. However, existing experimental (e.g., based on eddy correlation methods) evidence for fine particles shows that atmospheric stability has a significant influence on dry deposition. Several experiments (Damay, 2010; Hicks, 1979; Lamaud et al., 1994; Wesely et al., 1977, 1983; Wesely and Hicks, 1979) indicate that the deposition velocities for fine particles in the daytime are considerably greater than that in nighttime and tend to follow a diurnal pattern similar to that of the surface heat energy cycle (small near dusk and dawn and rising to a maximum near noon). By summarizing the experimental data (Gallagher et al., 1997; Nemitz and Sutton, 2004), Fowler et al. (2009) found that when the background wind speeds are similar, deposition velocities under convective conditions are larger than those under neutral and stable conditions. Pellerin et al. (2017) suggested that cospectral similarities exist between heat and particle-deposition fluxes. Thus, later models (Petroff and Zhang, 2010; Zhang et al., 2001) account for the effects of atmospheric stability by applying the Monin-Obukhov similarity theory (MOST, Monin and Obukhov, 1954; Monin and Yaglom, 2013) corrections to eddy diffusivity, utilizing the framework of the Slinn (1982) scheme. The ZS14 scheme further considered the heterogeneity of obstacles on the surface.

The issue of scale is a major problem for theoretical deposition schemes when predicting deposition on a regional or global scale. Currently, these deposition schemes consider atmospheric turbulence as a whole in the delivery of particles to the ground under the assumption of steady-state and homogeneous ABL winds. The atmospheric turbulence is characterized by the friction velocity obtained from Reynolds-averaged wind (typically averaged over 15-30 min) in large-scale models. However, the predictions of deposition using large-scale models show a discrepancy with field experiments, especially for particles with size in accumulation mode (100 nm-2 μm) under convective conditions (Fowler et al., 2009; Hicks et al., 2016), which can be attributed to intermittent gusts of wind. According to their measurements, Wesely et al. (1985a) pointed out that convective motions increase wind gustiness near the surface, which, in turn, considerably increases particle deposition velocities. Wesely et al. (1983) suggested that some effects of convective mixings, such as rapid multidirectional flow around surface elements, enhance particle deposition in the surface layer. Porch (1974) indicated that low wind speed usually alternates with strong intermittent gusts. The gusts at the ground are caused by turbulence due to friction, wind shear, or solar heating of the ground. These local intermittent strong wind gusts are sudden but short-lived peaks in wind speed. The Reynolds-averaging method is unable to represent the information of instantaneous changes in the wind field, especially as the winds are multidirectional and can be canceled out by averaging over a period of 15-30 min. Overall, in current large-scale simulations, the theoretical models only account for the time-averaged wind speed, disregarding the gusts that can significantly enhance dust deposition. This oversight leads to a misrepresentation of the dust deposition magnitude. Therefore, a more accurate description of dust deposition requires the inclusion of this omitted information, i.e., the description of instantaneous wind field information.

1.2 Thesis objectives and outline

This thesis investigates the influence of ABL stability on dust deposition and attempts to improve an existing particle-deposition scheme for convective conditions in large-scale models. The WRF-LES/D, which couples the WRF model in LES mode with dust modules including the dust deposition scheme of ZS14, is used here. The WRF-LES (hereafter LES) is used to simulate high-resolution turbulence under various ABL stability conditions. LES is chosen because it explicitly predicts the turbulence parameters required to parameterize the deposition process, such as sensible heat flux, which are difficult to reproduce in the laboratory. The ZS14 scheme is used to calculate the surface deposition for each simulation grid. Particle deposition rates resulting from the simulation of the WRF-LES/D model and the prediction by using the ZS14 scheme with friction velocity that is obtained by spatially and temporally averaging the vector winds are compared with each other and with measurements. A physically integrated parameterization scheme that quantifies the level of wind turbulence intensity and considers the corresponding particle deposition processes is then developed. The new parameterization is developed because of physical processes and evaluated experimentally in high-resolution large eddy simulations. Furthermore, it is generally applicable to large-scale regional models. Specifically, this thesis addresses the following four objectives:

1) Investigation of the dependency of turbulence on atmospheric stability and background wind field.

2) Improvement of the deposition scheme of ZS14 based on WRF-LES/D experiments, considering the effects of turbulence under different ABL stability and wind conditions.

3) Evaluation of the improved scheme through WRF-LES/D experiments.

4) Implementation of the improved scheme into a regional atmospheric model.

The structure of this thesis is as follows: Chapter 2 introduced the basic background and theory, including the definitions of meteorological parameters used in the thesis and the particle deposition process. Chapter 3 describes the WRF-LES/D model. Chapter 4 details the design of the numerical experiments conducted under various wind conditions and ABL stabilities. It then discusses the findings of the numerical experiments and finally proposes improvements to the ZS14 scheme. Chapter 5 applies the new improved scheme to predict dust deposition on a regional scale. Finally, Chapter 6 summarizes the aforementioned work and provides an outlook for future research.

2. Scientific background and schemes review

Turbulence in the ABL is crucial for particle diffusion and deposition. Several factors, such as surface structure, ABL stability, and wind speed can influence ABL turbulence. Depending on the way turbulence is generated, ABLs can be classified as stable, unstable, and neutral. This chapter begins with an introduction to atmospheric turbulence and its key concepts (Section 2.1). This is followed by a description of the physical deposition process of dust particles and a review of several well-known deposition schemes (Section 2.2). Subsequently, the effects of the ABL stability on the deposition velocity are presented (Section 2.3). Lastly, the differences in deposition velocity resulting from the turbulent fluctuations in friction velocity are discussed (Section 2.4).

2.1 Atmospheric turbulence

2.1.1 The definition of turbulence

Figure 2-1 illustrates the energy spectrum representing the typical timescales for atmospheric flows. As seen, the turbulence (or turbulent flow) field is largely composed of vertical motions (structures or eddies) of different sizes. Eddies are airflows whose direction differs from the general flow, but the net result of the motions of the eddies that make up the air is the motion of the air as a whole. For example, the gusts superimposed on the mean wind are eddies that can be visualized as irregular swirls of motion. The generation of turbulence is usually related to surface forces, such as radiative heating of the surface, wind shear due to the friction of air on the surface, large wind gradients, or surface obstructions (Damay, 2010). In the ABL, the vertical transport of momentum, mass, and energy occurs through turbulence whose magnitude is less than or similar to the depth of the ABL (Shao, 2008).

Due to random fluctuations of turbulence, statistical methods are often used to describe turbulence. According to the Reynolds averaging method, any atmospheric or scalar variable X (e.g., wind speed, temperature, scalar concentration), can be decomposed into a time-averaged term ($\overline{X}$) and a turbulence term (X') as follows:

$$X = \overline{X} + X' \tag{2.1}$$

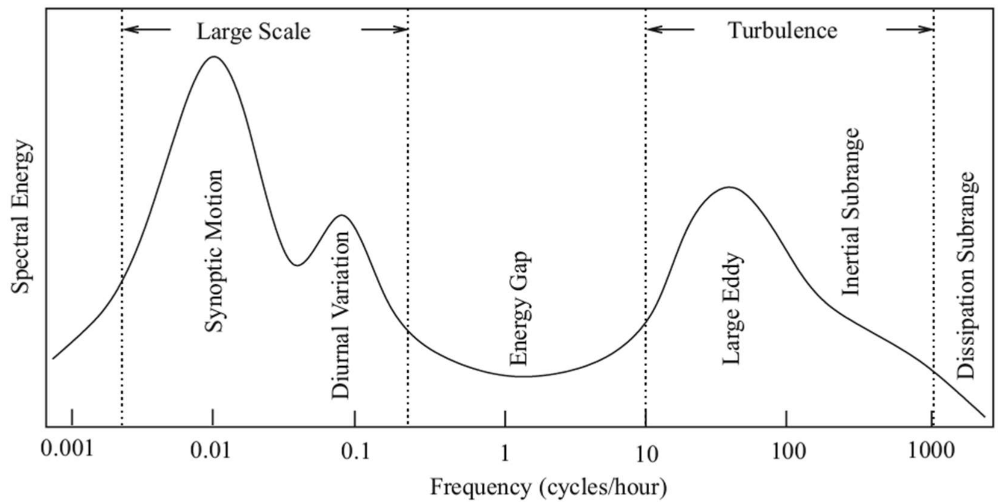

Figure 2-1: Schematic energy spectrum of atmospheric flows, showing the distinct regimes of synoptic scale motion, energy gap, large eddy, inertial subrange and dissipation subrange (from Shao (2008)).

The average time is typically chosen to range between 15 and 30 minutes, which is shorter than the temporal scales for large-scale motion yet longer than those for turbulence. This means that the Reynolds averaging method filters out the turbulent eddies. As Figure 2-1 shows, the turbulent fluctuation X' consists of large eddies and inertial subrange turbulence. The grid filtering method provides a solution for identifying eddies that are spatially larger than the filter grid. Thus, the variable X can be expressed as a superposition of a Reynolds averaged term $\overline{X}$, a turbulent fraction $\widetilde{X}$ on scales larger than the filter grid size, and a turbulent fraction X_{sg} on scales smaller than the filter grid size, as follows:

$$X = \overline{X} + \tilde{X} + X_{sg} \tag{2.2}$$

Comparing Equation (2.1) and Equation (2.2), we see that the turbulence term consists of eddies of different sizes superimposed on each other, as follows:

$$X' = \tilde{X} + X_{sg} \tag{2.3}$$

The characteristics of a typical ABL flow are strongly dependent on the heat flux at the lower boundary, and thus on the stability (Garratt, 1994). Thus, the next section will introduce the relevant concepts of ABL stability.

2.1.2 Atmospheric stability

Several stability parameters can be used to express the ABL stability, such as static stability, Richardson number, and Obukhov length. Static stability is a measure of the capacity for buoyant convection. It is defined by the vertical gradient of the potential temperature $\partial\bar{\theta}/\partial z$ or the surface heat flux $\overline{w'\theta'}$. If $\partial\bar{\theta}/\partial z > 0$ or $\overline{w'\theta'} < 0$, the ABL is statically stable, if $\partial\bar{\theta}/\partial z < 0$ or $\overline{w'\theta'} > 0$, the ABL is statically unstable, if $\partial\bar{\theta}/\partial z = 0$ or $\overline{w'\theta'} = 0$, the ABL is neutral. However, neither $\partial\bar{\theta}/\partial z$ nor $\overline{w'\theta'}$ show the mechanical generation of turbulence, hence the static stability does not depend on the wind. Dynamic stability is partly dependent on the wind. It can cause turbulence even in statically stable ABL. In static unstable ABL, convection occurs, which tends to move more buoyant air upward to stabilize the system, and in dynamic instabilities, turbulence tends to reduce the wind shear to stabilize the system. Thus, thermally generated turbulence tends to have a large vertical extent compared to mechanically generated turbulence.

The Richardson number, Ri, is a more accurate indicator for the development of turbulence. Ri denotes the ratio of the magnitudes of the shear production and buoyant consumption terms within the turbulent kinetic energy (TKE) equation (which is described in the next chapter). It has several forms, one of which is the gradient Richardson number as follows:

$$\mathrm{Ri} = \frac{g}{\bar{\theta}} \frac{\partial\bar{\theta} / \partial z}{\left(\partial\bar{u} / \partial z\right)^2 + \left(\partial\bar{v} / \partial z\right)^2} \tag{2.4}$$

For statically unstable flows, Ri is negative. For neutral flows, it is zero. For statically stable flows, Ri is positive. A critical value of 0.25, at which the mechanical production rate balances the buoyant consumption of TKE, exists. When $0 < \mathrm{Ri} < 0.25$, static stability suppresses the mechanical generation of turbulence. When Ri < 0, turbulence is contributed by both mechanical force and convection. When Ri = 0, there is only mechanical turbulence. A detailed stability classification is summarized in Table 2-1.

The Obukhov length within the surface layer, L_O, as defined in Equation (2.5), serves as a stability indicator, with its sign indicating static stability: a negative value signifies instability, a positive value denotes stability, and it approaches infinity under neutral stratification conditions.

$$L_O = -\frac{u_*^3}{\kappa\left(g/\bar{\theta}\right)\overline{w'\theta'}_0} \tag{2.5}$$

where κ is the von Karman constant, g (= 9.81 m s^{-2}) is the gravitational acceleration, u_* is the friction velocity (or the shear stress velocity), and $\overline{w'\theta'}_0$ is the kinematic temperature flux at the surface. The Obukhov length is proportional to the height above the surface at which the buoyant factors begin to dominate over the mechanical generation of turbulence. The structures of the ABL and turbulent wind under different ABL stability conditions are discussed below.

Table 2-1: The stability classification with corresponding critical values of Ri.

Stability classification	Richardson number	Comment
Stable	Ri > 0.25	No vertical mixing, winds weak, strong inversion, mechanical turbulence dampened, negligible spreading of the smoke plume.
Stable	0 < Ri < 0.25	Mechanical turbulence weakened by stable stratification
Neutral	Ri = 0	Mechanical turbulence only
Unstable	-0.03 < Ri < 0	Mechanical turbulence and convection
Unstable	Ri < -0.04	Convection predominant, winds weak, strong vertical motion, smoke rapidly spreading vertically and horizontally

2.1.3 Features of different ABL stability

As stated in the previous sections, both buoyant convective processes (i.e., thermals of warm air rising) and mechanical processes (e.g., wind shear) can generate turbulence. However, the structure of the ABL generated by these two processes is different. Figure 2-2 shows a clear distinction in turbulence structure between the convective ABL and the stable ABL. As depicted in Figure 2-2a, in the convective ABL, the structure of horizontal wind droop eddy is integrated at a height that extends through the depth of the ABL. While Figure 2-2b indicates that the statically stable stratification restricts integral scales. The integral-scale eddies (large eddies) in Figure 2-2a carry most of the turbulent kinetic energy and perform most of the turbulent transport.

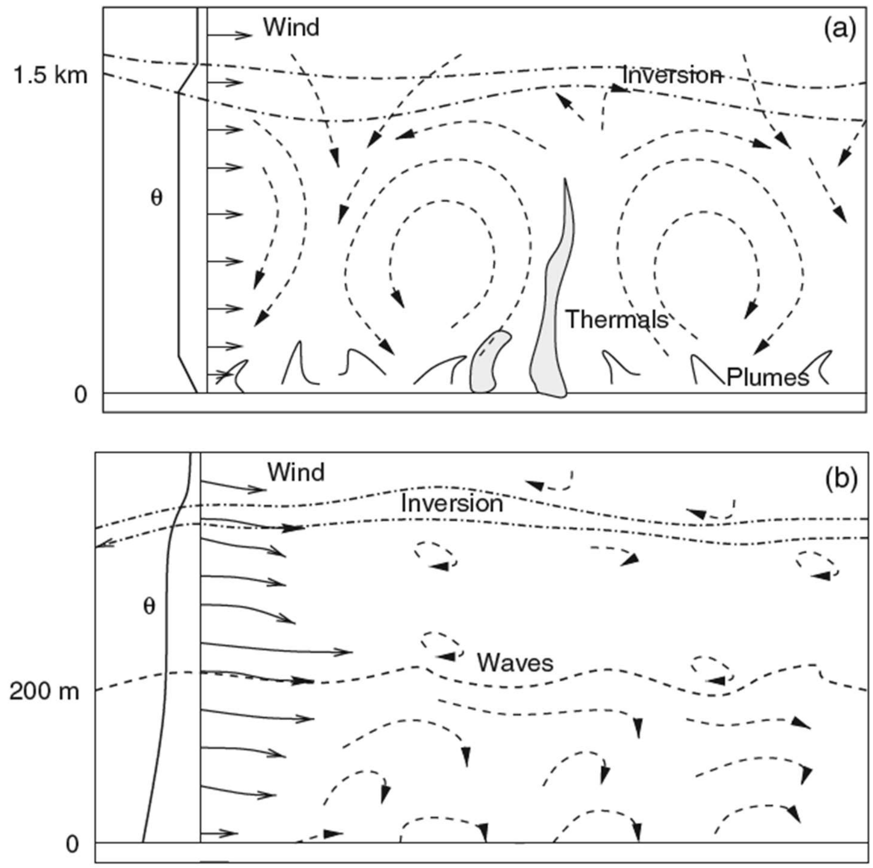

Figure 2-2: (a) Schematic diagram of the convective ABL characterized by large eddies, capping inversion, and well-mixed mean profiles of wind and potential temperature. (b) Schematic diagram of the stable ABL characterized the small eddies, shallow depth, low-level jet, and mean wind temperature gradients (Shao (2008), modified from Wyngaard (1990)).

Furthermore, the range of turbulent wind speed fluctuations varies with different stability. Figure 2-3 shows the instantaneous turbulent horizontal and vertical wind speeds measured in situ in the stable and unstable ABL. The data are from a field experiment in Yuzhong County performed by this study, which will be presented in Section 2.3.3. The vertical and horizontal wind velocities are measured by an ultrasonic anemometer at a height of 5.29 m. As can be seen in Figure 2-3a, the perturbations of both the turbulent horizontal wind speed and the turbulent vertical wind speed, as shown in Figure 2-3b, are greater in the unstable ABL than in the stable ABL.

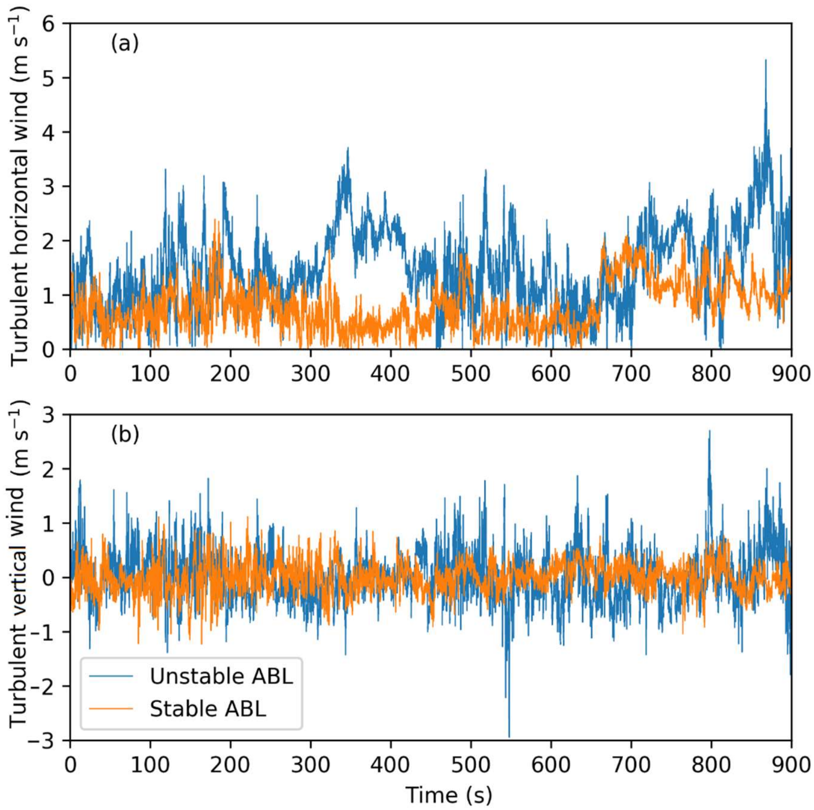

Figure 2-3: (a) Turbulent horizontal wind speed in the unstable ABL (blue line) and that in stable ABL (orange line). (b) Same as (a), but for turbulent vertical wind speed.

2.2 Dust deposition process

2.2.1 Airborne dust particles

The interaction between dust particles and airflow dominates the movement of dust in the air. This interaction, in turn, is highly dependent on the physical properties of the particles, such as size, shape, and density. The size of atmospheric aerosol (including dust particles) is distributed over a considerable range, from a few nanometers (nm) to several tens of micrometers (μm). Figure 2-4 shows an idealized atmospheric aerosol size distribution in which particles tend to appear in five characteristic modes. Nucleation mode particles are usually considered to be smaller than 10 nm. Aitken (or nuclei) mode particles range from 10 to 100 nm in diameter. Accumulation mode particles range from about 100 nm to 2 μm and are observed to be influenced by the ABL stability. Coarse mode particles with sizes typically larger than 2 μm are often emitted into the atmosphere due to mechanical forces (Buseck and Schwartz, 2013).

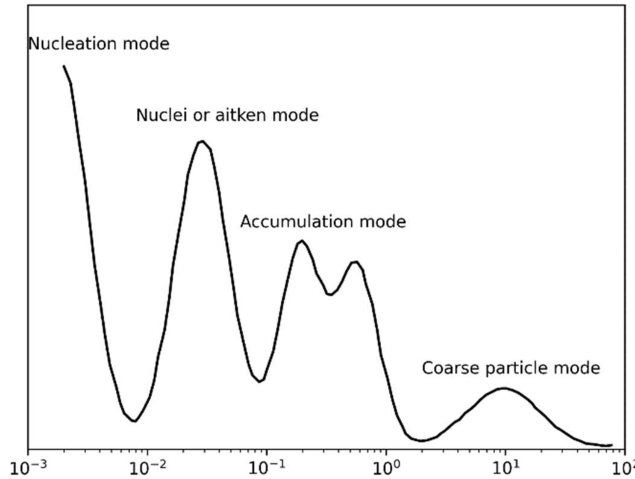

Figure 2-4: The idealized particle size distribution of atmospheric aerosols varies with the source and is classified into five typical modes: Nucleation mode ($D_p \leq 10$ nm), Nuclei or Aitken mode (10 nm < $D_p \leq 100$ nm), Accumulation mode (100 nm < $D_p \leq 2$ μm), and Coarse particle mode ($D_p > 2$ μm) (modified from Buseck and Schwartz (2013)).

The shape of airborne dust is observed to be highly irregular, ranging from spherical to slab-like and from very angular to well-rounded (Gieré and Querol, 2010). In practice, most theoretical models use the equivalent particle size of spheres, which have the same aerodynamic or optical properties as irregular particles. The mass-equivalent particle size is also adopted in this thesis and is given by

$$D_{\mathrm{p}} = \left(\frac{6m_p}{\pi\rho_p} \right)^{1/3} \tag{2.6}$$

with m_p being the mass of any shaped particle and ρ_p being the particle density. Figure 2-5 shows an irregularly shaped particle with its equivalent particle size. Assuming that the mass distribution of the particles is uniform, the density of dust particles ρ_p is usually taken to be 2650 kg m^{-3}. In the following discussion, dust particles are considered to be homogeneous, and their equivalent diameters are used in the associated calculations.

The motion of particles in the air is governed by several forces, of which gravity and aerodynamic drag are the dominant forces, as shown in Figure 2-5. The gravity of a particle with a diameter of D_p can be obtained from

$$G = \frac{1}{6}\rho_p D_p^{\ 3} g \tag{2.7}$$

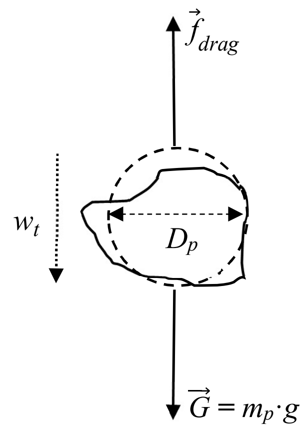

Figure 2-5: Schematic representation of the equivalent particle size, D_p, of any particle. G is the gravity acting on the particle, f_{drag} is the aerodynamic drag force, and w_t is the terminal velocity.

The magnitude of the aerodynamic drag force, denoted as f_{drag}, depends critically on the flow pattern around the particle. For dust particles that measure less than 20 µm, their capacity to track the airflow is notable. Consequently, it is postulated that the horizontal velocity of these dust particles parallels the horizontal airflow, resulting in a horizontal relative velocity of zero. Consequently, the relative velocity between the dust and the air is considered identical to the vertical relative velocity w_r. Precisely calculating the aerodynamic drag force, f_{drag}, is achievable through the application of the Stokes formula (Hinds, 1982), which is articulated as follows:

$$f_{\mathrm{drag}} = -\frac{3\pi\mu_{\mathrm{a}} D_p w_r}{C_u} \tag{2.8}$$

where μ_a is the aerodynamic viscosity, w_r denotes the vertical relative velocity between the particle and the surrounding air, C_{u} is the Cunningham correction factor that accounts for the slipping effect on fine particles (Seinfeld and Pandis, 2006),

$$C_u = 1 + \frac{2\lambda_m}{D_p}\left(1.257 + 0.4e^{-0.55 D_p/\lambda_m}\right) \tag{2.9}$$

with $\lambda_m = \frac{K_B T}{\sqrt{2}\pi D_a^2 p}$ being the mean free path of the dust particles. K_B is Boltzmann constant, T is temperature, p is pressure and D_a is the effective diameter of the air molecule.

The aerodynamic drag force on the particle is present whenever there is a particle-to-air relative motion. The direction of drag force is opposite to the direction of the particle-to-air relative velocity. When the aerodynamic drag is equal to its gravity, the airborne particle is in equilibrium, i.e., $\vec{f}_{drag} + \vec{G} = 0$. The calculation of particles' terminal velocity is based on the work of Malcolm and Raupach (1991) as well as Seinfeld and Pandis (2006), with the corresponding expression being as follows:

$$w_t = \frac{C_u \rho_p D_p^2}{18\mu_a} g \tag{2.10}$$

where $\frac{C_u \rho_p D_p^2}{18\mu_a} = T_p$ is defined as particle relaxation time. Thus, the velocity of dust particles (in vector form) is

$$\vec{U}_p = u \cdot \vec{i} + v \cdot \vec{j} + (w - w_t) \cdot \vec{k} \tag{2.11}$$

where u, v, and w are the instantaneous wind speeds along the x, y, and z axes, respectively. w is positive when pointing upwards. The minus here represents the downward gravity. It is theoretically possible to use the direct numerical simulation (DNS) method to solve the velocity of the airflow around each particle. However, due to the very high computational cost, which will be explained in the next chapter, using the DNS method is not suitable for simulating the flow in the ABL. A popular approach to this issue is to treat the dust concentration in the ABL as a continuous variable.

2.2.2 Surface collection efficiency

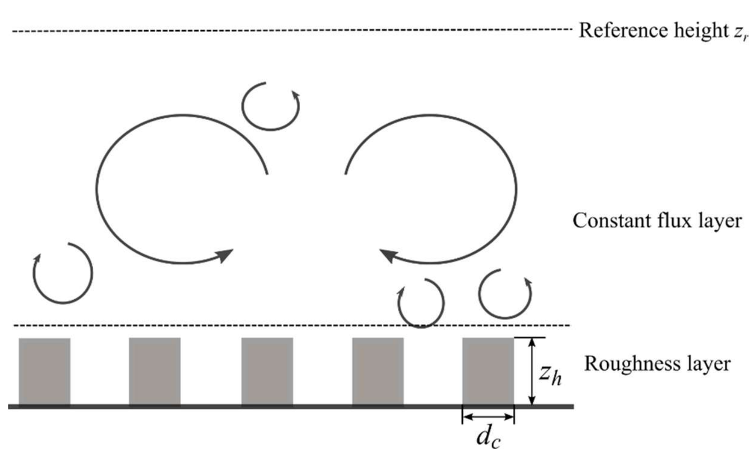

Figure 2-6: Illustration of the two-layer model with rough surface. The roughness element with height h_c and diameter d_c (modified from Zhang and Shao (2014)).

Figure 2-6 illustrates a two-layer model characterizing the atmospheric boundary layer. The upper layer is named the transfer layer, while the lower layer is referred to as the roughness layer. The complexity of the roughness layer is evident across the natural landscape, where a diverse array of surfaces displays heterogeneity due to the presence of various roughness elements (grass, trees, rocks, etc.). Thus, the rough surface needs to be simplified in the dust deposition study. A simplified heterogeneous surface conceptualizes the ground as a composition of the same roughness elements, randomly distributed across an initially bare terrain (Raupach, 1992; Shao and Yang, 2008; Zhang and Shao, 2014).

Dust deposition occurs when the suspended dust particles in the air enter the roughness layer and are captured by the roughness elements. Extensive research has delved into the efficiency of dust collection by the roughness elements, denoted as E. A widely accepted understanding is that E encompasses the combined contributions of Brownian motion E_{B}, impaction E_{im}, and interception E_{in}, i.e., $E = E_B + E_{im} + E_{in}$. The proportions of each contribution depend on the micrometeorological elements, the physical characteristics of the airborne particles, and the properties of the surface (Petroff et al., 2008a; Sportisse, 2007). Although numerous studies have assessed the effectiveness of molecular diffusion, impaction, and interception as dust collection mechanisms, the expressions differ significantly across these studies. Table 2-2 provides a summary of various well-known collection efficiency mechanisms. Figure 2-7 illustrates the procedures involved in dust collection through filter material. Elaborate insights into these collection processes are expounded upon in the subsequent discussion.

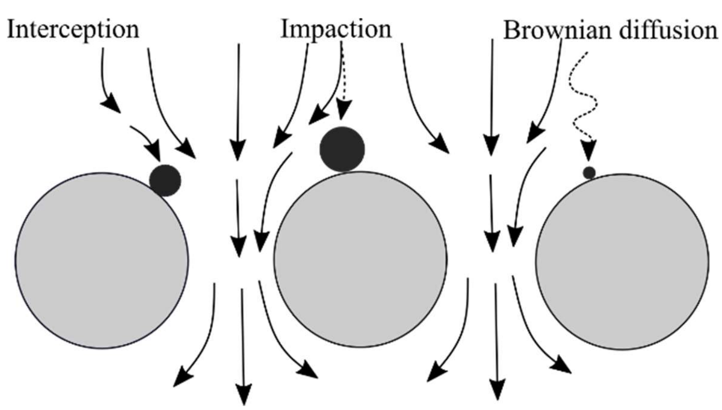

Figure 2-7: Schematic illustration showcasing the collection processes of dust particles (black-filled circles) through interception, impaction, and Brownian diffusion by obstacles (gray-filled circles).

a. Brownian diffusion

Airborne dust particles are subjected to continuous interactions with the surrounding air molecules. When these particles are sufficiently small, often falling within the nanometer to submicrometer range, collisions with neighboring molecules trigger a state of erratic and irregular movement, known as Brownian diffusion. The equations governing Brownian diffusion, outlined in detail in Table 2-2, encompass a range of parameters: the Schmidt number, Sc, which represents the ratio of air's kinematic viscosity (ν) to the particle's molecular diffusivity (k_p); c_v, signifying the average viscous drag coefficient for vegetation; c_d, representing the average drag coefficient for vegetation; a, indicating an empirical coefficient that escalates with heightened surface roughness; Re, standing for the Reynolds number relevant to the obstacle; and finally, parameters C_B and n_B, which are contingent upon the flow regime and their respective values are presented in Table 2-3.

Table 2-2: Comparison of collection parameterizations in mechanistic models.

	E_B	E_{im}	E_{in}
Slinn and Slinn (1980)	$Sc^{-1/2}$	$10^{-3/\hat{T}_p}$	0
Slinn (1982)	$\frac{c_v}{c_d} Sc^{-2/3}$	$\frac{St^2}{1+St^2}$	$\frac{c_v}{c_d}\left[c\frac{D_p}{D_p+d_c^{\,s}}+(1-c)\frac{D_p}{D_p+d_c^{\,l}}\right]$
Zhang et al. (2001)	Sc^{-a}, $0.5 \leqslant a \leqslant 0.58$	$\left(\frac{St}{0.8+St}\right)^2$	$\frac{1}{2}\left(\frac{D_p}{d_c}\right)^2$
Petroff et al. (2008b)	$C_B Sc^{-2/3} Re^{n_B-1}$	$\left(\frac{St}{0.6+St}\right)^2$	$\frac{2D_p}{d_c}$
ZS14 scheme	$C_B Sc^{-2/3} Re^{n_B-1}$	$\left(\frac{St}{0.6+St}\right)^2$	$\mathrm{A_{in}} \cdot u_* \cdot 10^{-St} \cdot \frac{2D_p}{d_c}$

Table 2-3: Diffusive transfer to vertical obstacles described by Petroff et al. (2008b).

Re	C_B	n_B
1-4×10^3	0.467	0.5
4×10^3-4×10^4	0.203	0.6
4×10^4-4×10^5	0.025	0.8

b. Interception

Interception and impaction exhibit their most effective collection efficiency when dust particles fall within the intermediate size range of 0.1 μm to 5 μm (Fowler et al., 2009). Interception is primarily considered the dominant collection mechanism for dust particles sized below 2 μm (Droppo, 2006). This phenomenon occurs when the distance between the dust particles moving with the airflow and the obstacle is smaller than the particle's radius.

Existing research generally concurs that the significance of interception hinges on the ratio of particle size to roughness size, as depicted in Table 2-2. The ZS14 scheme suggests that the interception efficiency of obstacles is also influenced by wind speed. In Table 2-2, the parameter A_{in} accounts for the micro-roughness characteristics, such as the ratio of hair size to obstacle size. $St = T_p u_* / d_c$ represents the Stokes number. 10^{-St} corrects for deviations in particle behavior following the airflow and is nearly equal to 1 for particles with low inertia. T_p is the particle relaxation time. d_c signifies the diameter of the filter material.

c. Impaction

Dust particles within the range of 2 μm to 5 μm are excessively sizable to seamlessly track the alterations in airflow direction due to their considerable inertia. Consequently, these particles might encounter the obstacle or the ground during the response time after the airflow's interaction with them or its descent to the ground. The collision efficiency E_{im} for particle-ground collisions differs from that of particle-obstacle collisions. In circumstances involving surfaces featuring obstacles, particle-ground collisions are commonly neglected. The ZS14 scheme differentiates the ground surface into two categories: bare ground and obstacle-covered ground. The scheme provides the impaction efficiency for both scenarios, and further elaboration on this can be found in the ZS14 scheme review below.

Table 2-2 compiles various mechanisms governing particle-obstacle collision efficiency, wherein $\hat{T}_p$ signifies the dimensionless particle relaxation time (Liu and Agarwal, 1974) expressed as:

$$\hat{T}_p = \frac{T_p u_*^2}{\nu} \tag{2.12}$$

d. Rebound

The rebound fraction, denoted as R, characterizes the decrease in particle collection due to instances of particle bounce-off (Chamberlain, 1967). This phenomenon is contingent upon the initial kinetic energy of the particle and the adhesive properties of the underlying surface. An illustrative example is the rebound fraction of water surfaces, which stands at a value of zero due to its inherent properties. In the case of natural grass, Slinn (1982) suggests the rebound fraction can be calculated as follows:

$$R = \exp\left(-b\sqrt{St}\right) \tag{2.13}$$

with b being an empirical constant. And b is set to 2 based on Chamberlain (1967)'s wind tunnel data, while Giorgi (1986) and Zhang et al. (2001) set it to 1. In the ZS14 scheme, b varies according to the land use category.

However, obtaining the dust deposition flux in the roughness layer is challenging due to the unknown nature of the dust concentration at the surface. Consequently, researchers often rely on assuming a constant vertical flux above the surface in dust deposition studies. This assumption entails that the mass transport per unit time and unit area remains consistent in the vertical direction from the top of the roughness layer to the top of the roughness layer, as shown in Figure 2-6. While this constant flux assumption in the surface layer might not hold for instantaneous fluxes, it holds reasonably accurate for average vertical fluxes observed over a sufficiently large sample. With this assumption in place, it becomes possible to establish a relationship between the movement of dust and its deposition.

Operating within the framework of a constant flux assumption, the dust deposition flux at the surface equals the dust flux at a reference height z_r above the surface. Assuming uniform wind velocity and dust concentration within a specific volume of space. Analogous to wind flow, the dust concentration at height z_r can be divided into its mean and fluctuating components, denoted as $\overline{c}$ and c', respectively. Thus, the Reynolds-averaged transported aerosol flux $F_d\left(x, y, z\right)$ can be estimated as

$$F_{d,x} = \overline{\left(\overline{u} + u'\right)\left(\overline{c} + c'\right)} = \overline{u}\ \overline{c} + \overline{u'c'} \tag{2.14a}$$

$$F_{d,y} = \overline{\left(\overline{v} + v'\right)\left(\overline{c} + c'\right)} = \overline{v}\ \overline{c} + \overline{v'c'} \tag{2.14b}$$

$$F_{d,z} = \overline{\left(\overline{w}_p + w_p{}'\right)\left(\overline{c} + c'\right)} = \overline{w}_p\overline{c} + \overline{w_p{}'c'} \tag{2.14c}$$

where $w_p = w - w_t$ is the vertical velocity of the particle. Since the terminal velocity w_t is related solely to dust properties, the averaged vertical wind velocity $\overline{w} = 0$ results in $\overline{w}_p \overline{c} = \overline{w}_t \overline{c}$. As a consequence, Equation (2.14c) can be reformulated as

$$F_{d,z} = -w_t \overline{c} + \overline{w'c'} \tag{2.15}$$

On the right-hand side of the equation, the first term, $-w_t \overline{c}$, represents the gravitational settling, represented by $F_{d,g}$. This term describes the process of a particle moving through the air under the influence of gravity. Gravitational settling begins to dominate the overall deposition process when the size of the dust particle is greater than 5 μm (Fowler et al., 2009). while the final term, $\overline{w'c'}$, indicates the diffusion flux. The diffusion flux includes contributions from both Brownian diffusion, denoted as $F_{d,B}$, and turbulent diffusion, denoted as $F_{d,T}$. Thus $F_{d,z} = F_{d,g} + F_{d,B} + F_{d,T}$.

Following Fick's law (Fick, 1855), the Brownian diffusion flux can be obtained using

$$F_{d,B} = -k_p \frac{\partial \overline{c}}{\partial z} \tag{2.16}$$

where $k_p = K_B T C_u / 3\pi \mu_a D_p$ is the molecular diffusivity pertaining to dust particles. Within the constant flux layer, the vertical gradients of the mean wind speed, scalar concentration, and temperature dominate the turbulent fluxes of momentum, mass, and heat. Analogous to molecular diffusion, the turbulent flux of dust particles is parameterized through K-theory as follows:

$$F_{d,T} = -K_p \frac{\partial \overline{c}}{\partial z} \tag{2.17}$$

where K_p is the eddy diffusivity and can be determined by

$$K_p = Sc_T \cdot K_m \tag{2.18}$$

where K_m stands for the eddy viscosity, which is discussed in the next chapter and Sc_T is the turbulent Schmidt number determined by the turbulence strength and particle inertia magnitude (Csanady, 1963), given as

$$Sc_T = \left(1 + \frac{\mathrm{b}_1^2 w_t^2}{\sigma^2}\right)^{-1/2} \tag{2.19}$$

with b_1 being the empirical coefficient and σ being the standard deviation of the turbulent wind.

By substituting Equations (2.16) and (2.17) into Equation (2.15), the resulting expression is a comprehensive representation of the particle deposition flux, presented as:

$$F_d = -w_t \overline{c} - \left(k_p + K_p\right) \frac{\partial \overline{c}}{\partial z} \tag{2.20}$$

The deposition velocity at a reference height is defined as the deposition flux normalized by the concentration at the same height, expressed as follows:

$$V_d = -\frac{F_d(z_r)}{\overline{c}(z_r)} \tag{2.21}$$

where the positive sign indicates that the downward deposition velocity is treated as positive. The essence of the dust deposition scheme is to address the computation of the deposition velocity.

2.2.3 Review of particle-deposition schemes

The exploration of particle deposition onto complex surfaces typically initiates with an examination of fundamental filtration principles, such as interception and impaction. From there, supplementary processes that contribute to the overall system are integrated into the analysis (Hicks et al., 2016). Figure 2-8 illustrates the schematic diagram involving many physical processes involved in dust deposition between the airborne source (i.e., the dusty atmosphere at a reference height z_r) and receptor surfaces. In the figure, thermophoresis is responsible for pushing particles away from heated surfaces due to the increased energy of gas molecules colliding with the side of a particle that is oriented towards the surface. Diffusiophoresis occurs when particles are present in a mixture of multiple gases exhibiting a concentration gradient of one of the gases. Both thermophoresis and diffusiophoresis are contingent on the interplay between atmospheric molecules and the particles. Thes processes are adequately intricate, and in many field situations, their impact on dry deposition can be disregarded because of the small phoretic effects. The figure also shows that it is possible to order, quantify, and logically combine the processes that control the exchange of particles and gases between the atmosphere and the surface.

A popular approach to the case of gas exchange is accomplished by introducing a resistance component to account for the physical processes. The now-familiar multiple-resistance model for dust particles is an extension of gaseous deposition (Chamberlain, 1967). Analogous to an electric circuit, the principle of this model is to treat the difference in dust concentration as a voltage, the deposition flux as a current, and the inverse of the deposition velocity as the resistance. Thus, the deposition process of airborne dust has two layers to consider: the upper layer is from a height z_r to the top of the roughness layer, and the lower layer is from the top of the roughness layer to the surface of roughness elements or ground. Normally, the contribution associated with near-surface phoretic effects is overlooked, and surface properties are simplified. Therefore, in the upper layer, the aerodynamic factors, consisting of turbulence and gravity settling, dominate dust movement. In the lower layer, particles are trapped by impaction, interception, or Brownian diffusion.

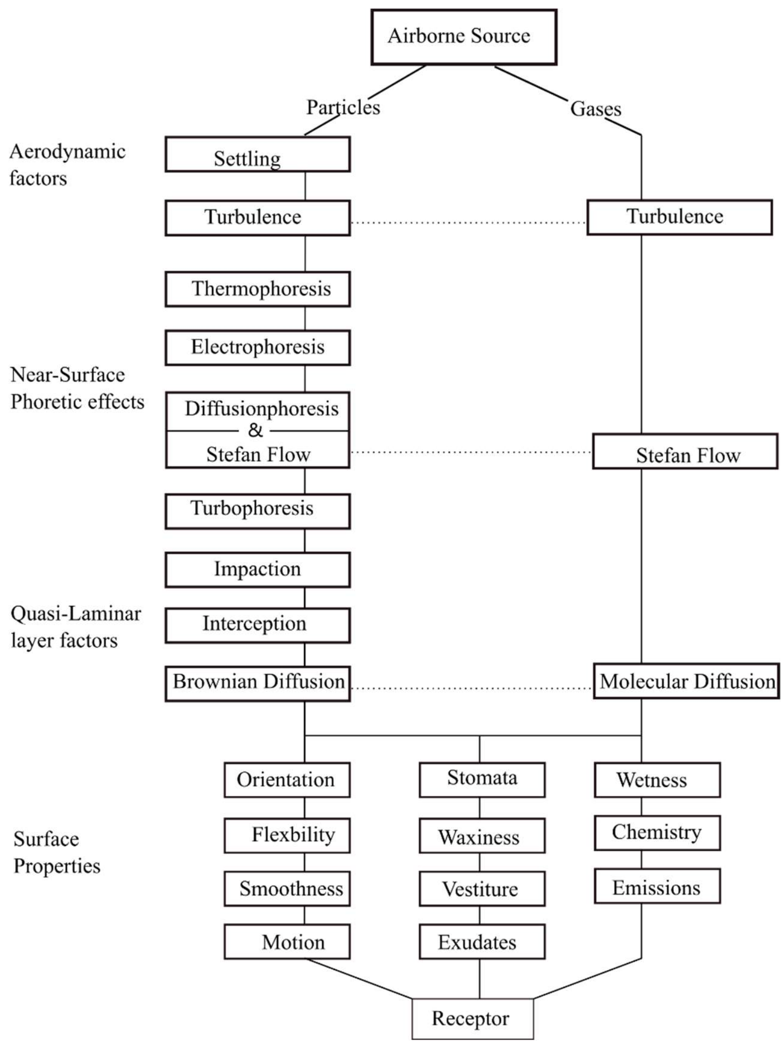

Figure 2-8: A depiction of the processes contributing to the deposition of airborne particles and trace gases (redrawn from Hicks et al. (2016)).

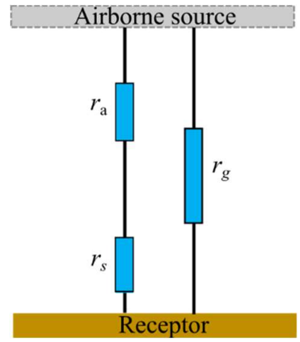

Figure 2-9: A simple resistance analogy for a particle aerosol from source to sink. r_a is the aerodynamic resistance considering the turbulence phenomenon in the transfer layer, r_s is the quasi-laminar sublayer resistance related to the Brownian motion, interception, and impaction. r_g is the gravitational resistance. In the upper layer, the deposition flux by Brownian diffusion (redrawn from Hicks et al. (1987)).

Figure 2-9 illustrates a resistance diagram depicting the resistances between the source and receptor. The aerodynamic resistance r_a signifies the downward transfer capacity of dust through turbulence diffusion from the open air to the layer adjacent to the receptor layer. The collection resistance r_s is related to the capacity of the collection layer to capture and retain particles. Slinn (1982) proposed an expression for deposition velocity as follows:

$$v_d = w_t + \frac{1}{r_a + r_s} \tag{2.22}$$

Furthermore, Slinn (1982) assumed that the eddy diffusivity for mass is equal to that for momentum. Additionally, within the transfer layer, molecular diffusion is negligible compared to eddy diffusion. Consequently, integrating $F_{d,T}$ in Equation (2.17) from the top of the roughness layer z_h to the height z_r in the open air yields:

$$r_a = -\frac{\overline{c}(z) - \overline{c}(z_h)}{\overline{F}_{d,T}} = \int_{z_h}^{z_r} \frac{1}{K_p} dz = \int_{z_h}^{z_r} \frac{1}{ku_* z} dz = \frac{1}{ku_*} \ln\left(\frac{z_r}{z_h}\right) \tag{2.23}$$

where κ is the von Kármán constant.

The transfer resistance across the quasi-laminar layer, r_s, is the inverse of the deposition velocity in the roughness layer. Considering the vertical variation of wind velocity, dust concentration, and leaf area in the roughness layer, Slinn (1982) suggested that

$$r_s = \frac{U_{\mathrm{a}}(z_h)}{u_*^2}\frac{1}{\sqrt{\xi}}\left\{\frac{1+\sqrt{\xi}\tanh\gamma\sqrt{\xi}}{\sqrt{\xi}+\tanh\gamma\sqrt{\xi}}\right\} \tag{2.24}$$

where $U_{\mathrm{a}}(z_h)$ is the magnitude of the mean horizontal wind speed at height z_h and $U_a = \left(\overline{u}^2 + \overline{v}^2\right)^{1/2}$, $\xi = \left(E_B + E_{im} + E_{in}\right)\cdot R$, γ is a parameter characterizing the wind profile in the canopy and is expected to be in the range $2 \leqslant \gamma \leqslant 5$.

Zhang et al. (2001) simplified the scheme of Slinn (1982) in both aerodynamic resistance and collection resistance. For aerodynamic resistance, they considered the MOST-based ABL stability correction and introduced the roughness length z_0 instead of using the canopy height z_h, which is consistent with gas transfer. In Zhang et al. (2001), r_a is expressed as

$$r_a = \frac{1}{ku_*}\left[\ln\left(z_r/z_0\right) - \psi_m\right] \tag{2.25}$$

where ψ_{m} is the integral of the stability function between z_0 to z_r.

For collection resistance, Zhang et al. (2001) assumed that the wind and the dust concentration in the quasi-laminar layer are spatially homogeneous. Assuming the dust concentration and wind speed throughout the roughness layer are the same as that at the top of the roughness layer, the collection resistance of the roughness layer r_s can be expressed as

$$r_s = -\frac{\overline{c}(z_h)}{F_s(z_h)} \tag{2.26}$$

where $F_s(z_h) = F_d(z_h) - F_{d,g}(z_h)$ is the dust deposition flux captured by the roughness layer and can be calculated with

$$F_s(z_h) = -U_a(z_h)\cdot\overline{c}(z_h)\cdot\left(E_B + E_{im} + E_{in}\right)\cdot R \tag{2.27}$$

By substituting Equation (2.27) into Equation (2.26), r_s can be expressed as follows:

$$r_s = \frac{1}{U_a(z_h)\cdot\left(E_B + E_{im} + E_{in}\right)\cdot R} \tag{2.28}$$

with the wind velocity U_{a} at z_h is assumed equal to 3 times the friction velocity u_*, i.e., $U_{\mathrm{a}} = 3\,u_*$.

Venkatram and Pleim (1999) pointed out that the multiple-resistance model for particles conflicts with mass conservation. They suggested integrating Equation (2.20) and combining it with Equation (2.21) directly to derive the deposition velocity as

$$V_d = \left[\frac{w_t}{1 - \exp(-r_a \cdot w_t)} \right]^{-1} \tag{2.29}$$

However, Venkatram and Pleim (1999) did not describe the surface collection process. Since Venkatram and Pleim (1999) did not account for the surface collection process, the ZS14 scheme has improved upon this method. Details about the ZS14 scheme are provided below.

The ZS14 scheme

By integrating Equation (2.20) from the top of the roughness layer to the reference height and combining it with Equation (2.21), the ZS14 scheme suggests the following expression for the deposition velocity:

$$V_d = \left[r_g + \frac{r_s - r_g}{\exp(r_a / r_g)} \right]^{-1} \tag{2.30}$$

with r_g being the gravitational resistance. The gravitational resistance r_g is defined as the reciprocal of the gravitational settling velocity w_t and depends mainly on particle size and density, which is calculated as:

$$r_g = w_t^{-1} = \left(\frac{C_u \rho_p D_p^2 g}{18 \mu_a} \right)^{-1} \tag{2.31}$$

Using the MOST, the aerodynamic resistance between the reference height z_r and the top of the roughness layer, z_h, is calculated as:

$$r_a = \frac{Sc_T}{ku_*} \left[\ln \left(\frac{z - z_d}{z_h - z_d} \right) - \psi_m \right] \tag{2.32}$$

where z_d is the displacement height.

In addition to the friction velocity, the ZS14 scheme takes into account surface heterogeneity and links drag partitioning with deposition flux partitioning in the collection process. Dust deposition within the roughness layer encompasses the deposition on the roofs of roughness elements, the portion on bare ground, the part captured by the frontal area of the roughness elements, and the gravitational settling. Table 2-2 presents the collection efficiency by the frontal area of the roughness elements used in the ZS14 scheme. The collection process on the roof surface of the roughness elements and the bare ground only includes the Brownian diffusion and impaction. Assuming the laminar layer for wind and scalar is the same, the total dust deposition on the roof of the roughness elements and bare ground caused by Brownian diffusion is expressed as

$$F_{d,r}^{B} + F_{d,s}^{B} = -\frac{\tau + \tau_c}{\rho_a U_a(z_h)} \cdot Sc^{-1} \cdot \overline{c}(z_h) \tag{2.33}$$

where τ is the total shear stress on the surface, τ_c symbolizes the pressure drag force exerted on the roughness elements, and it can be estimated as

$$\tau_c = C_d \cdot \rho_a \cdot U_a\left(z_h\right)^2 \cdot \lambda \tag{2.34}$$

with C_d being the drag coefficient for an isolated roughness element, and λ representing the frontal area index of the isolated roughness element.

Drawing from Slinn and Slinn (1980), dust deposition through turbulent impaction on the roofs of roughness elements and bare ground can be quantified using

$$F_{d,r}^{im} + F_{d,s}^{im} = -\frac{\tau}{\rho_a U_a(z_h)} \cdot 10^{-\frac{3}{\hat{T}_p}} \cdot \overline{c}(z_h) \tag{2.35}$$

where $10^{-3/\hat{T}_p}$ signifies the turbulent impaction efficiency of upward-facing faces.

In comparison to previous studies, the ZS14 scheme integrates the frontal area index of roughness elements into dust collection, as demonstrated below:

$$F_{d,c} = -U_a(z_h) \cdot \overline{c}(z_h) \cdot \left(E_B + E_{im} + E_{in}\right) \cdot \lambda \tag{2.36}$$

By connecting this equation with the pressure drag acting on roughness elements, it can be reformulated as

$$F_{d,c} = -\frac{\tau_c}{\tau} \cdot \frac{\tau}{\rho_a U_a(z_h)} \cdot \frac{E}{C_d} \cdot \overline{c}(z_h) \tag{2.37}$$

The ratio τ_c/τ can be calculated according to Yang and Shao (2006), as follows:

$$\frac{\tau_c}{\tau} = \frac{\beta_1 \lambda_e}{1 + \beta_1 \lambda_e} \tag{2.38}$$

where β_1 (= 200) represents the ratio of the drag coefficient for an isolated roughness element to that for a bare surface, λ_e is the effective frontal area index expressed as

$$\lambda_e = \frac{\lambda}{\left(1-\eta\right)^6} \exp\left(-\frac{\lambda}{10\left(1-\eta\right)^6}\right) \tag{2.39}$$

where η denotes the basal area index of the roughness elements.

Therefore, total dust deposition flux can be computed using

$$F_d\left(z_h\right) = F_{d,c} + F_{d,r}^{im} + F_{d,s}^{im} + F_{d,r}^{B} + F_{d,s}^{B} + F_{d,g} \tag{2.40}$$

Substituting the Equations (2.33)- (2.40) into $r_s = -\frac{\bar{c}(z_h)}{F_d(z_h)}$ yields

$$r_s = \left\{ R \cdot \frac{\tau}{\rho_a \cdot U_a(z_h)} \left[\frac{E}{C_d} \frac{\tau_c}{\tau} + \left(1 + \frac{\tau_c}{\tau}\right) Sc^{-1} + 10^{-\frac{3}{T_p}} \right] + w_t \right\}^{-1} \tag{2.41}$$

The deposition schemes clearly illustrate that the deposition velocity is influenced by wind-induced shear stress or friction velocity. Due to turbulence, the shear stress is intermittent. However, the application of the deposition schemes in large-scale simulations has so far used the Reynolds averaged shear stress. The effect of the turbulent shear stress on the dust deposition velocity will be discussed in the following sections.

2.3 Effect of the ABL stability on deposition velocity and shear stress

2.3.1 Eddy correlation method

The eddy correlation (EC) method was proposed by Montgomery (1948), Swinbank (1951), and Obukhov (1951) to measure exchanges of momentum, heat, and mass between a flat, horizontally homogeneous surface and the overlying atmosphere. The covariance between turbulent fluctuations of the vertical wind and the desired quantity is the vertical flux. Thus, the vertical flux of momentum (also known as shear stress) in the kinematic unit is expressed as

$$\tau_R = \sqrt{\overline{u'w'}^2 + \overline{v'w'}^2} \tag{2.42}$$

The vertical flux of dust particles by eddy diffusion is

$$F_{d,T} = \overline{w'c'} \tag{2.43}$$

EC requires a very high sampling frequency (Businger, 1986). In practice, the acquisition frequency should be a minimum of 1 Hz for measurements a few meters above the ground (Damay et al., 2009). Figure 2-10 shows a schematic diagram of transport flux obtained by the EC method. At time 1, eddy 1 moves parcel of air c_1 down at speed w_1. Then, at time 2, eddy 2 moves parcel c_2 up at speed w_2. Each parcel of air has a horizontal wind velocity, a mass, and a temperature unit.

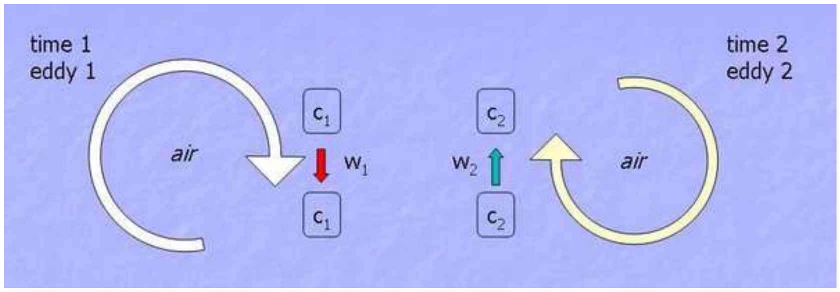

Figure 2-10: An illustration of air parcel transport by rotating eddies. Eddy 1 moves the air parcel c_1 down with the speed w_1, while eddy 2 moves parcel c_2 up with the speed w_2 (from Burba et al. (2013)).

2.3.2 Effects of the ABL stability on deposition velocity

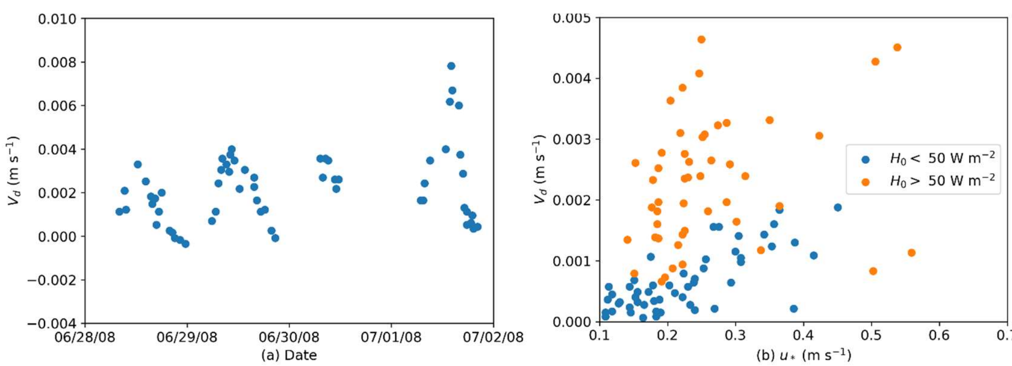

Figure 2-11: (a) Daily evolution of deposition velocity; (b) deposition velocity in terms of friction velocity u_* ($u_*=\sqrt{\tau_R}$ in kinematic unit), the dots correspond to H_0 > 50 Wm^{-2}. The diameter D_p = 33 nm (redrawn from Damay (2010)).

Many studies have described that dust deposition velocities are greater under unstable ABL conditions than under stable or neutral conditions. For example, Damay (2010) carried out a field experiment using the EC method to show the dependence of dust deposition velocity on vertical momentum flux and heat flux. Figure 2-11a shows that there is a clear diurnal trend in dust deposition velocity. At noon local time, when the heat flux released from the surface is higher than in the morning and evening local times, the dust deposition velocity is higher. To clarify the effects of friction velocity and heat flux on dust deposition velocity, Damay (2010) compared the deposition velocities with similar friction velocities but different heat fluxes, as shown in Figure 2-11b. As can be seen, Figure 2-11b indicates that dust deposition velocity increases with increasing friction velocity. In addition, for similar friction velocities, dust deposition velocities are higher for heat fluxes $H_0 > 50$ W m^{-2} than for heat fluxes $H_0 < 50$ W m^{-2}.

The overview of dust deposition in Section 2.2 shows that shear stress is a descriptor of the effect of ABL turbulence on dust deposition velocity. ABL stability strongly influences ABL flow characteristics, which, in turn, determine the shear stress. Therefore, to parameterize the effects of ABL stability, it is necessary to demonstrate the variation of turbulent shear stress with ABL stability.

2.3.3 Effect of ABL stability on shear stress distribution

As the instantaneous shear stress is not given in the study of Damay (2010), an in-situ observation of the instantaneous wind speed vector was conducted here. The in-situ measurement was carried out on 19 May 2019, from 08:00 to 20:00 local time at Cuiying Mountain in Yuzhong county (35.95°N, 104.18°E, altitude: 1965.8 m), which is a county in Lanzhou City, China. The land use type is a flat grassland with no big obstacles around it. Figure 2-12 illustrates the configuration of the field experiment. As shown, the instantaneous wind was measured using a suit of five ultrasonic anemometers (UA) mounted on the meteorological mast along the vertical direction. The sampling frequency is 50 Hz and the measured heights of the UA are 1, 2.06, 2.89, 4.05, and 5.29 m respectively. The instantaneous shear stress in the kinematic unit is calculated by

Figure 2-12: Configuration of the field experiment.

$$\tau_f = \sqrt{(uw)^2 + (vw)^2} \tag{2.44}$$

Figure 2-13 shows the probability density distributions of the instantaneous stresses and the corresponding instantaneous friction velocities. As shown, the variations in the magnitude of the instantaneous shear stress and friction velocity are greater under unstable conditions than under stable or neutral conditions. In the atmosphere, the deviation is determined by the atmospheric stability for the same surface properties.

Section 2.3.2 and Section 2.3.3 indicate that with higher heat flux, the dust deposition velocity, as shown in Figure 2-11, is greater and shear stress, as shown in Figure 2-13, has a wider range of deviations. Therefore, my hypothesis for this issue is that the difference in dust deposition velocity caused by the heat flux is because more large vertical eddies can be generated in convective ABL. As these large eddies intermittently increase the local shear stress, the deposition velocity is intermittently increased. As the turbulent variation of wind speed can be described by its distribution, in the next section there will be an ideal theoretical analysis of the effect of the friction velocity distribution on the bulk deposition velocity.

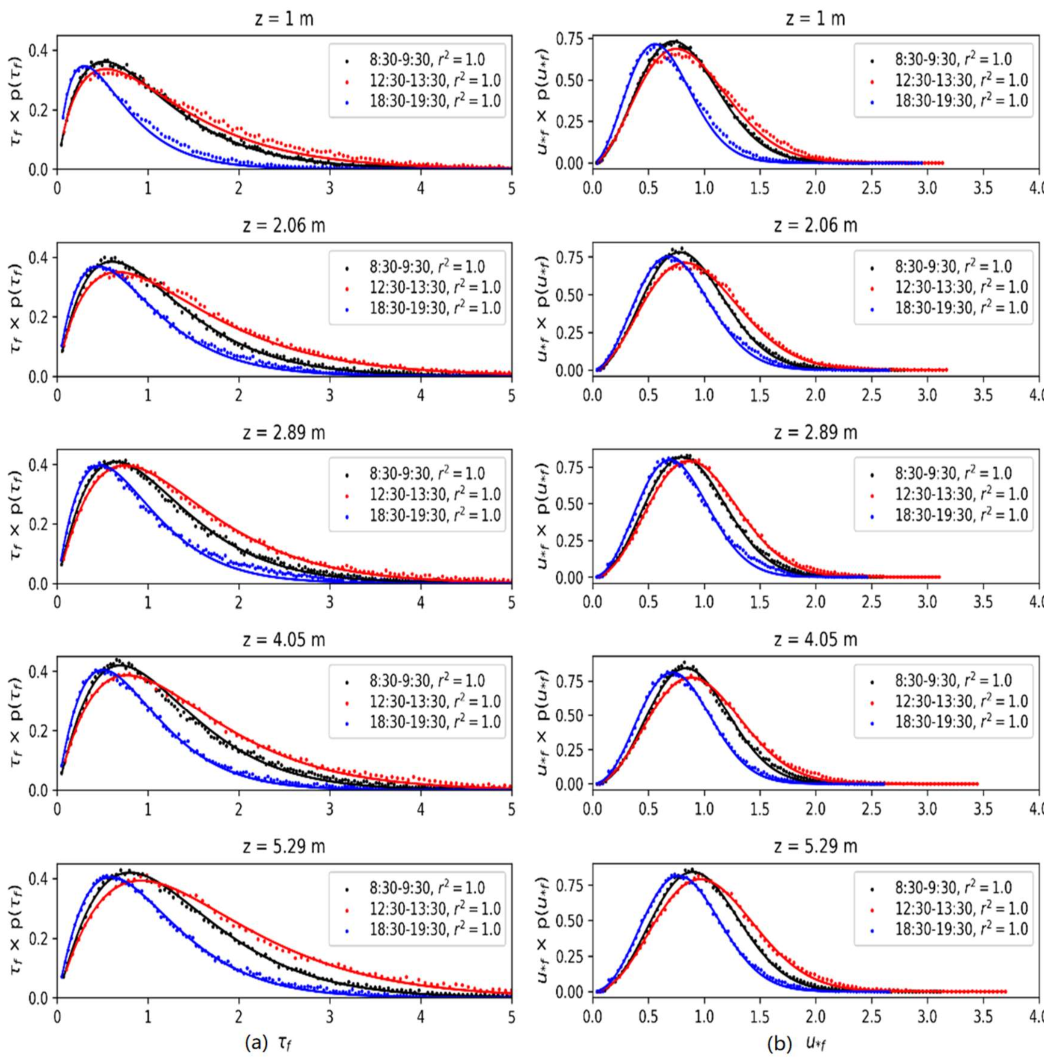

Figure 2-13: The time-varying of shear stress (a) and corresponding friction velocity density (b) distribution at different heights.

2.4 Effect of shear stress distribution on deposition velocity

Previous studies of dust deposition velocity have almost exclusively used Reynolds-averaged shear stresses, i.e., the averaged shear stresses of the transient large eddies with different directions. This does not fully account for the effects of the transient large eddies on dust deposition velocity. This section aims to show that, in addition to the average value, the standard deviation of the shear stress or the friction velocity distribution is also responsible for the increase in deposition velocity.

Following Shao et al. (2020), u_{*_n} with n = 1, 2, 3, 4, 5, 6, are considered here individually with the following assumptions:

- u_{*_n} follow a Gaussian distribution.
- u_{*_n} have the same mean value, e.g., $\bar{u}_{*_n}$ = 0.22 m s^{-1} in this study.
- u_{*_n} have the standard deviations σ_n = 0.02, 0.03, 0.04, 0.05, 0.06,0.08, respectively.
- Deposition velocity, V_d, is calculated by the deposition scheme of ZS14.

With these assumptions, the distributions of the friction velocities, u_{*n}, are shown in Figure 2-14. Note that the instantaneous stress or instantaneous friction velocity along a given axis can be positive or negative, with a negative sign indicating a negative direction to the given axis.

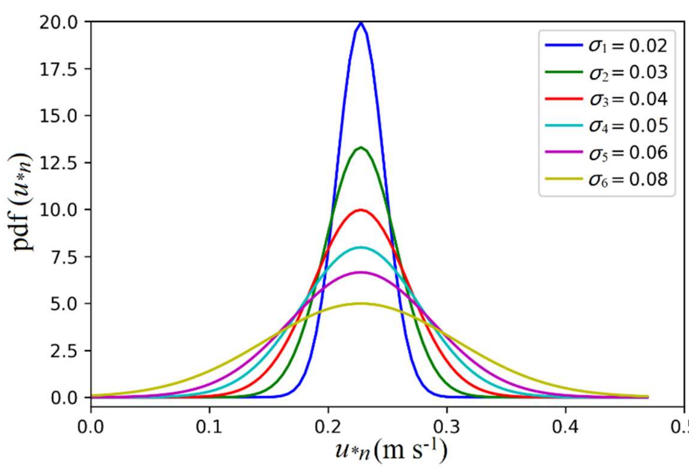

Figure 2-14: The Gaussian distribution of the stochastic variable u_{*_n} with mean value $\bar{u}_{*_n}$ = 0.22 m s^{-1}. The standard deviations σ_n = 0.02, 0.03, 0.04, 0.05, 0.06, 0.08 for n = 1, 2, 3, 4, 5, 6, respectively.

Taking each value in u_{*n} into the ZS14 model, i.e., Equations (2.30)-(2.41), the mean values of each $V_d\left(u_{*n}\right)$ can be obtained as

$$\overline{V_d\left(u_{*n}\right)} = \int_0^{\infty} V_d\left(u_{*n}\right) p\left(u_{*n}\right) du_{*n} \qquad \text{with } n = 1, 2, 3, 4, 5, 6 \tag{2.39}$$

with $p(u_{*n})$ being the probability density distribution of u_{*n}.

Taking $\overline{V_d\left(u_{*1}\right)}$ as a reference, the ratio of the other $\overline{V_d\left(u_{*n}\right)}$ to $\overline{V_d\left(u_{*1}\right)}$ represents the difference caused by the various standard deviations of the distribution of u_{*n}, as follows:

$$\eta_{V_d} = \overline{V_d\left(u_{*n}\right)} \Big/ \overline{V_d\left(u_{*1}\right)} \tag{2.40}$$

Figure 2-15 shows that the ratio η_{V_d} increases as the standard deviation of the distribution of u_{*n} increases, especially for particles with sizes between approximately 0.01 µm and 5 µm. The result indicates that the effect of the distribution of friction velocity on deposition velocity cannot be ignored when the standard deviation of friction velocity is large.

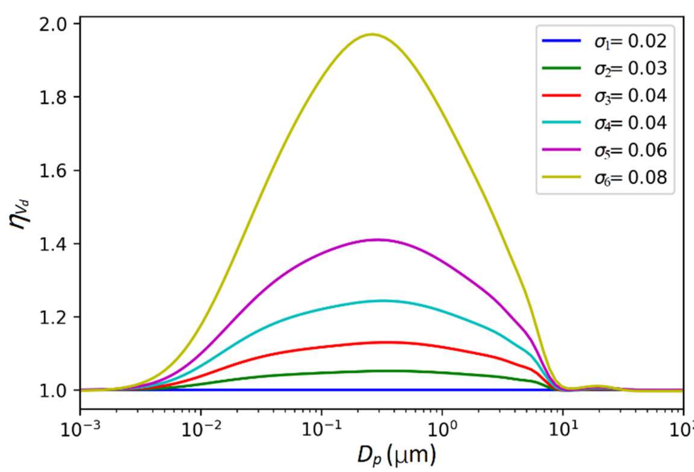

Figure 2-15: The ratio of the mean deposition velocity $\overline{V_d\left(u_{*n}\right)}$ with n = 1, 2, 3, 4, 5, 6 and the $\overline{V_d\left(u_{*1}\right)}$, where $\overline{V_d\left(u_{*n}\right)}$ is calculated by the statistical variable u_{*n} assumed to follow a Gaussian distribution with different standard deviations σ$_n$ and $\overline{V_d\left(u_{*n}\right)}$ is the $\overline{V_d\left(u_{*n}\right)}$ with n = 1.

In summary, the dust deposition velocity calculated by the deposition scheme, such as the ZS14 scheme used here, does not only depend on the average value of the shear stress in time or space but is also influenced by the distribution of the stress fluctuations. For a fixed mean value, a larger turbulent variation range of friction velocity corresponds to a larger bulk deposition velocity. Thus, the above tests clearly demonstrate that a more accurate assessment of deposition velocity requires accounting for precise information on the distribution of instantaneous shear forces, rather than simply relying on the Reynolds-averaged shear stress over the studied period. Therefore, the effect of transient shear stress should be considered in the context of the impact of ABL stability on deposition rates.

3. Methodology

In this thesis, both the WRF model and the WRF-LES model are used and coupled with a dust module. WRF is a regional model and WRF-LES is the large-eddy mode of WRF, which allows for partial resolution of the turbulence spectrum. WRF-LES has the same framework as the WRF model but with different grid resolution and subgrid closure mechanisms. The WRF-LES/D was originally developed by Shao et al. (2013), Klose and Shao (2013), and Liu et al. (2015). It is a well-established system used to simulate turbulence and particle motion under various ABL stability conditions. WRF-LES allows easily simulating different atmospheric conditions regarding the ABL stability by specifying the heat flux released from the surface in the input file and facilitates the coupling with dust modules.

To solve the governing equations for ABL flows, the LES and the Reynolds-Averaged Simulation (RAS) methods are used in WRF-LES and WRF, respectively. In this chapter, the governing equations are presented (Section 3.1), followed by an overview of the LES (Section 3.2) and the RAS (Section 3.3) methods. Then the surface layer scheme is described (Section 3.4). In the last section (Section 3.5), a comparison of the turbulent momentum flux from these two modelling approaches as well as the shear stress derivation are given.

3.1 Governing equations for ABL flows

The governing equations for ABL flows consist of an equation of state, the continuity equation, and the conservation equations for momentum (in three directions), temperature, moisture and scalar quantity (Stull, 1988). Below is the common system of governing equations in Cartesian coordinates.

The continuity equation and conservation equations for momentum in tensor form are

$$\frac{\partial \rho_a}{\partial t} + \frac{\partial \rho_a u_j}{\partial x_j} = 0 \tag{3.1}$$

$$\frac{\partial u_i}{\partial t} + \frac{\partial u_j u_i}{\partial x_j} = -\delta_{i3} g + \varepsilon_{ijk} f\, u_k - \frac{1}{\rho_a}\frac{\partial p}{\partial x_i} + \nu \frac{\partial^2 u_i}{\partial x_j^2} \tag{3.2}$$

where u_i with i = 1, 2, 3 are the wind speeds u, v and w along the x, y and z axes, respectively, δ_{i3} is the Kronecker delta, ε_{ij3} is the Levi-Civita-Pseudo-Tensor, f is the

Coriolis parameter and is defined as $f = 2\omega \sin \Phi$, with ω being the angular velocity of the Earth and Φ being the latitude, p is the pressure, ν is the kinematic viscosity. In Equation (3.2), $\varepsilon_{ijk} \cdot f \cdot u_k$ describes the Coriolis effect, which represents the influence of the Earth's rotation. $\partial p / \partial x_j$ describes the pressure-gradient force. For velocities much smaller than the speed of sound, the air is assumed to be an incompressible fluid. The last term on the right-hand side of Equation (3.2), $\nu \cdot \partial^2 u_i / \partial x_j^2$, presents the influence of viscous stress.

The state of the air is determined by its pressure, volume, and temperature. It is described adequately by the ideal gas law as

$$p = \rho_a \Re T_\mathrm{v} \tag{3.3}$$

where $\Re$ is the specific constant of air, $T_V = (1+0.61 \cdot \mathrm{r}) \cdot T$ is the virtual absolute temperature with the mixing ratio r for unsaturated air. The potential temperature θ is the temperature at which an air parcel of temperature T moves adiabatically from the given pressure to the reference pressure.

The conservation of water vapor in the air, written in tensor form, is as follows:

$$\frac{\partial q}{\partial t} + \frac{\partial u_j q}{\partial x_j} = k_q \frac{\partial^2 q}{\partial x_j{}^2} + \frac{S_q}{\rho_a} \tag{3.4}$$

where $q = \mathrm{r} / (1 + \mathrm{r})$ is the specific humidity of the air, k_q is the molecular diffusivity for water vapor and S_q describes a net moisture source.

The energy conservation of airflows in the ABL can be expressed by the conservation of the potential temperature equation:

$$\frac{\partial \theta}{\partial t} + \frac{\partial u_j \theta}{\partial x_j} = k_\theta \frac{\partial^2 \theta}{\partial x_j{}^2} + \frac{S_\theta}{\rho_a c_p} \tag{3.5}$$

where θ is the potential temperature, k_θ is the thermal diffusivity, c_p is the specific heat for moist air at constant pressure and $S_\theta = S_{\theta,rad} + S_{\theta,LH}$ is the net source term with $S_{\theta,rad}$ associated with the radiation divergence and $S_{\theta,LH}$ the latent heat released or consumed during the phase change.

The coupled dust module describes the temporal evolution of the dust concentration. Let c be the concentration of the dust aerosol in the atmosphere, representing the mass of dust per unit volume of air (kg m^{-3}). It is accepted that dust follows the airflow well in the horizontal direction, while in the vertical direction, it experiences a relative velocity to the vertical airflow due to gravity. The dust concentration equation is expressed as follows:

$$\frac{\partial c}{\partial t}+\frac{\partial (u_j - w_t)c}{\partial x}=k_p\frac{\partial^2 c}{\partial {x_j}^2}+\frac{S_p}{\rho_a} \tag{3.6}$$

where k_p is the molecular diffusivity of dust and S_p is the net source term in air. The terminal velocity w_t describes the relative velocity between the particle and the wind when the gravitational acceleration force acting on the particle is balanced by the aerodynamic drag.

The non-linear and coupled governing Equations (3.1)-(3.6) need to be solved numerically. Theoretically, three modelling approaches are available, namely DNS, LES, and RAS. However, DNS requires a grid fine enough to resolve the eddies down to the Kolmogorov length scale, η, which is of the order of 1 mm (Kaimal and Finnigan, 1994), where dissipation takes place. Assuming that the grid resolution needed to resolve the smallest eddies is equal to its maximum value η, $O(10^{18})$ grid points are required for a domain of size $10^3\times10^3\times10^3$ m^3 in the x, y and z directions. If the maximum vertical velocity and horizontal wind are 10 m s^{-1}, a time step of $O(10^{-4})$ is necessary. Even with the latest high-performance computing (HPC) systems, running such a model is prohibitively expensive. The solution to this problem is explicitly resolving the transport on larger scales and only approximating the effect of smaller scales. In the case of LES, large eddies are resolved, while the smaller eddies in the turbulence cascade are parametrized. This means that the model directly simulates the dynamics of larger turbulent structures, while the effect of smaller scales is represented through subgrid scale models. On the other hand, in the case of RAS, only the mean fields of the turbulent eddies are addressed, and all the turbulent eddies are parameterized. This approach relies on averaging the governing equations over time, leading to a set of equations that describe the mean behavior of the turbulence. The effect of turbulent fluctuation is captured through closure models. The following Sections 3.2 and 3.3 will delve into more detail on LES and RAS, respectively, explaining their formulations and applications in simulating ABL flows.

3.2 LES filtering and closure

The ABL turbulent flow encompasses eddies of different sizes. The main difficulty in modelling the atmosphere is the non-linear effect among eddies on various spatial and temporal scales (Rauterkus, 2021). LES is a mathematical model for turbulence that has been widely used to compute comprehensive simulations of boundary-layer flows since it was proposed by Smagorinsky (1963) and explored by Deardorff (1970). Unlike DNS, the main idea behind LES is to reduce the computational cost by not explicitly resolving the smallest length scales, which are the most computationally expensive to resolve. This is achieved by low-pass filtering of the Navier-Stokes equations. By filtering, the LES method decomposes a turbulent variable (X) into a grid-resolved component or filtered component, denoted by X_{g}, and a subgrid or unresolved component, denoted by X_{sg}.

The LES cannot explicitly account for eddies smaller than twice the grid spacing, the corresponding wavenumber is referred to as the cut-off wavenumber. The unresolved eddies are parameterized by a subgrid-scale (SGS) model. The SGS model requires the cut-off wavenumber to be within the so-called inertial subrange (see Figure 2-1), where theories exist on how turbulence cascades towards smaller scales and eventually dissipates (Kolmogorov, 1991).

According to Leonard (1975), the convolution of a quantity with the filter function $G(\vec{x}-\vec{\varsigma})$ yields its grid-resolved part. For example, the resolved wind speed along the x-axis $\vec{u}_g$ (or $u_g(\vec{x})$) is obtained from:

$$u_g(\vec{x}) = \int_D G(\vec{x}-\vec{\varsigma})u(\vec{\varsigma})d\vec{\varsigma} \tag{3.7}$$

with the Box filter

$$G(\vec{x}-\vec{\varsigma}) = \begin{cases} \dfrac{1}{\Delta} & \vec{x} - \vec{\varsigma} < \dfrac{\Delta}{2} \\ 0 & \text{else} \end{cases} \tag{3.8}$$

used in WRF-LES. Δ is the filter width, twice the x and y grid spacing Δx and Δy. $\vec{\varsigma}$ represents an auxiliary cartesian vector for integration, corresponding to $\vec{x}$. The residual part or SGS part can be obtained from:

$$u_{sg} = u - u_g \tag{3.9}$$

By filtering Equation (3.2), the prognostic equation for the grid-resolved $u_{i,\mathrm{g}}$ is

$$\frac{\partial u_{i,g}}{\partial t} + \frac{\partial \left(u_j u_i\right)_g}{\partial x_j} = -\delta_{i3} g + \varepsilon_{ijk} f\, u_{k,g} - \frac{1}{\rho_a}\frac{\partial p_g}{\partial x_i} + \nu \frac{\partial^2 u_{i,g}}{\partial x_j^2} \tag{3.10}$$

Other basic governing equations at the large eddy scale, which are not repeated here, can be derived using the same approach. According to Leonard (1975), the filtered flux term $(u_j\, u_i)_g$ is rewritten as

$$
\begin{aligned}
\left(u_i u_j\right)_g &= \left(\left(u_{i,g}+u_{i,sg}\right)\left(u_{j,g}+u_{j,sg}\right)\right)_g \\
&= \left(u_{i,g}u_{j,g}+u_{i,g}u_{j,sg}+u_{i,sg}u_{j,g}+u_{i,sg}u_{j,sg}\right)_g \\
&= \left(u_{i,g}u_{j,g}\right)_g+\left(u_{i,g}u_{j,sg}\right)_g+\left(u_{i,sg}u_{j,g}\right)_g+\left(u_{i,sg}u_{j,sg}\right)_g \\
&= u_{i,g}u_{j,g}+\underbrace{\left(u_{i,g}u_{j,g}\right)_g-u_{i,g}u_{j,g}}_{L_{ij}}+\underbrace{\left(u_{i,g}u_{j,sg}\right)_g+\left(u_{i,sg}u_{j,g}\right)_g}_{C_{ij}}+\underbrace{\left(u_{i,sg}u_{j,sg}\right)_g}_{R_{ij}}
\end{aligned}
\tag{3.11}
$$

where L_{ij} is the Leonard stress due to interactions of resolved eddies, C_{ij} is the cross stress due to interactions between resolved and unresolved eddies, and R_{ij} is the SGS Reynolds stress representing interactions of unresolved eddies. Following Pope (2000), the SGS stress in kinematic units is defined as τ_{sg} and $\tau_{sg} = L_{ij} + C_{ij} + R_{ij}$. Applying Equation (3.11) gives

$$\tau_{sg} = \left(u_i u_j\right)_g - u_{i,g}u_{j,g} \tag{3.12}$$

$u_{i,g}u_{j,g}$ is the advection of momentum by the resolved wind, defined as the resolved stress in kinematic units, τ_g, that is

$$\tau_g = u_{i,g}u_{j,g} \tag{3.13}$$

Substituting Equations (3.12) and (3.13) into Equation (3.10) gives

$$\frac{\partial u_{i,g}}{\partial t}+\frac{\partial u_{i,g}u_{j,g}}{\partial x_j} = -\delta_{i3}g+\varepsilon_{ij3}f\,u_{j,g}-\frac{1}{\rho_a}\frac{\partial p_g}{\partial x_i}+\nu\frac{\partial^2 u_{i,g}}{\partial x_j{}^2}-\frac{\partial \tau_{sg}}{\partial x_j} \tag{3.14}$$

However, this procedure leads to the problem of turbulence closure. To close the governing equations, τ_{sg} is usually parameterized by linking to the terms of the resolved variables. The eddy-viscosity model (Cottet et al., 2003; Pope, 2000; Schmitt, 2007) is commonly used to achieve this. This model relates τ_{sg} to the filtered strain rate, S_{ij}, via the Boussinesq hypothesis:

$$\tau_{sg} = -2K_{m,sg}S_{ij}+\frac{1}{3}\tau_{kk,sg}\delta_{ij} \tag{3.15}$$

where

$$S_{ij} = \frac{1}{2}\left(\frac{\partial u_{i,g}}{\partial x_j}+\frac{\partial u_{j,g}}{\partial x_i}\right) \tag{3.16}$$

$K_{m,sg}$ is the SGS eddy viscosity. Substituting Equation (3.15) and Equation (3.16) into Equation (3.14) gives:

$$\frac{\partial u_{i,g}}{\partial t}+\frac{\partial u_{i,g}u_{j,g}}{\partial x_j}=-\delta_{i3}g+\varepsilon_{ij3}f\,u_{j,g}-\frac{1}{\rho_a}\frac{\partial \tilde{p}_g}{\partial x_i}+\nu\frac{\partial^2 u_{i,g}}{\partial x_j^{\;2}}+\frac{\partial}{\partial x_j}\left[K_{m,sg}\left(\frac{\partial u_{i,g}}{\partial x_j}+\frac{\partial u_{j,g}}{\partial x_i}\right)\right] \tag{3.17}$$

with $\tilde{p}_g = p_g/\rho_a + \frac{1}{3}\tau_{kk,sg}$ being the modified pressure constrained by the continuity equation. $K_{m,sg}$ in Equation (3.15) becomes the key to be addressed. In this study, the *k-l* closure scheme (Deardorff, 1980) is applied, which uses kinetic energy to calculate the subgrid eddy viscosity $K_{\mathrm{m,sg}}$, as follows:

$$K_{m,sg} = ku_{*\mathrm{sg}}l \tag{3.18}$$

where l is the mixing length, which is different for the horizontal and vertical directions. Assuming that Δx, Δy and Δz are grid resolutions for the x, y, and z directions, respectively, then:

$$l_x = l_y = \left(\Delta x\,\Delta y\right)^{1/2} \tag{3.19}$$

and

$$l_z = \begin{cases} \min\left[\Delta z,\ 0.76\sqrt{e}/B_f\right] & \text{for } B_f^{\;2} > 0 \\ \Delta z & \text{for } B_f^{\;2} \le 0 \end{cases} \tag{3.20}$$

with $e = 0.5\cdot\left(u_{sg}^{\;2}+v_{sg}^{\;2}+w_{sg}^{\;2}\right)$ being the non-resolved turbulence kinetic energy (TKE) and B_f the Brunt-Väisälä frequency calculated by the gradient of potential temperature and humidity in either a moist saturated or unsaturated environment., u_{*sg} is the subgrid scaling velocity, calculated from

$$u_{*\mathrm{sg}} = C_k\sqrt{e}/k \tag{3.21}$$

where $C_k = 0.15$ is an empirical parameter (Shao et al., 2013). The filtered prognostic equation for the evolution of TKE (hereafter TKE equation; Skamarock et al., 2008) is:

$$\frac{\partial e}{\partial t}+\frac{\partial u_{j,g}e}{\partial x_j} = \text{shear production term} + \text{buoyancy term} + \text{dissipation term} \tag{3.22}$$

where the shear production term (or mechanical production term) represents the production of TKE by wind shear. The buoyancy term describes non-resolved TKE consumed or generated by buoyancy. Buoyancy generates turbulence if the sensible-heat flux is upward and suppresses turbulence if the sensible-heat flux is downward. Buoyancy influences only the wind velocity directed in the vertical direction. The dissipation term describes the viscous dissipation rate for TKE. Dissipation reduces TKE by converting it irreversibly into heat. These source and sink terms are calculated as follows:

$$\text{shear production term} = K_{m,sg} S_{ij}{}^{2} \tag{3.23}$$

$$\text{buoyancy term} = -K_{h,sg} B_{f}{}^{2} \tag{3.24}$$

$$\text{dissipation term} = \frac{c_{\varepsilon} e^{3/2}}{l} \tag{3.25}$$

where $K_{h,sg}$ is a subgrid eddy coefficient for scalar quantities, and the value of the empirical coefficient c_{ε} depends on C_k, and either the grid volume or SGS TKE and B_f. Analogous to wind velocity, temperature, moisture, and the equation for dust concentration can also be split into a resolved part and a subgrid part. After filtering, Equations (3.1)-(3.6) become:

$$\frac{\partial \rho_a}{\partial t} + \frac{\partial \rho_a u_{j,g}}{\partial x_j} = 0 \tag{3.26}$$

$$\frac{\partial u_{i,g}}{\partial t} + \frac{\partial u_{i,g} u_{j,g}}{\partial x_j} = -\delta_{i3} g + \varepsilon_{ij3} f \ u_{j,g} - \frac{1}{\rho_a} \frac{\partial p_g}{\partial x_i} + \nu \frac{\partial^2 u_{i,g}}{\partial x_j{}^2} - \frac{\partial \tau_{sg}}{\partial x_j} \tag{3.14}$$

$$\frac{\partial \theta_g}{\partial t} + \frac{\partial u_{j,g} \theta_g}{\partial x_j} = k_\theta \frac{\partial^2 \theta_g}{\partial x_j{}^2} + \frac{1}{c_p} \cdot \frac{\partial H_{j,sg}}{\partial x_j} + \frac{S_{\theta,g}}{c_p \rho_a} \tag{3.27}$$

$$p_g = \rho_a \Re_a T_g \tag{3.28}$$

$$\frac{\partial q_g}{\partial t} + \frac{\partial u_{j,g} q_g}{\partial x_j} = k_q \frac{\partial^2 q_g}{\partial x_j{}^2} + \frac{\partial^2 Q_{j,sg}}{\partial x_j} + \frac{S_{q,g}}{\rho_a} \tag{3.29}$$

$$\frac{\partial c_g}{\partial t} + \frac{\partial u_g c_g}{\partial x} + \frac{\partial v_g c_g}{\partial y} + \frac{\partial \left(w_g - w_t \right) c_g}{\partial z} = -k_p \frac{\partial^2 c_g}{\partial x_j{}^2} + \frac{\partial F_{j,sg}}{\partial x_j} + \frac{S_{p,g}}{\rho_a} \tag{3.30}$$

where H_j, Q_j, and F_j are the subgrid fluxes of heat, moisture, and dust, respectively. The subgrid eddy diffusivity for heat $K_{h,sg}$ and scalar $K_{p,sg}$ can be expressed as:

$$K_{h,sg} = K_{p,sg} = K_{m,sg} P_r^{-1} \tag{3.31}$$

According to Deardorff (1972), the Prandtl number $P_r = 1/3$ for the horizontal eddy viscosity, and $P_r^{-1} = 1 + 2l_z / \Delta z$ for vertical eddy viscosity. Thus, by combining the prognostic equations at a large-eddy scale with the TKE equation and the SGS model, the temporal and spatial variations of the substance in the ABL are obtained.

3.3 RAS filtering and closure

RAS filtering is an averaging procedure applied to atmospheric substances in a turbulent flow. This average is usually taken over a period of time, but it may also be taken over space or an ensemble. By applying Reynolds averaging, a physical variable X in the ABL can be decomposed into a mean and a turbulent perturbation, i.e., $X = \bar{X} + X'$ (Equation (2.1)). The average value $\bar{X}$ is given by

$$\overline{X} = \frac{1}{T}\int_0^T X(t)dt \tag{3.32}$$

where T is a time period and is typically 15-30 minutes. So that the fluctuating part X' has

$$\overline{X'} = 0 \tag{3.33}$$

Thus, the following derivation is valid for the general variables X and Y.

$$\overline{XY} = \overline{\left(\overline{X} + X'\right)\left(\overline{Y} + Y'\right)} = \overline{\overline{X}\overline{Y} + \overline{X}Y' + X'\overline{Y} + X'Y'} = \overline{X}\,\overline{Y} + \overline{X'Y'} \tag{3.34}$$

$\overline{X'Y'}$ is the flux due to turbulent motion and is in general non-zero. Applying the Reynolds averaging to the basic governing Equations (3.1)-(3.6) for momentum, temperature and scalar gives

$$\frac{\partial \overline{u}_i}{\partial t} + \frac{\partial \overline{u}_i\overline{u}_j}{\partial x_j} = -\delta_{i3}g + \varepsilon_{ij3} f\,\overline{u}_j - \frac{1}{\rho_a}\frac{\partial \overline{p}}{\partial x_i} + \nu\frac{\partial^2 \overline{u}_i}{\partial {x_j}^2} - \frac{\partial \tau_R}{\partial x_j} \tag{3.35}$$

$$\frac{\partial \overline{\theta}}{\partial t} + \frac{\partial\left(\overline{u}_j\overline{\theta}\right)}{\partial x_j} = k_\theta\frac{\partial^2 \overline{\theta}}{\partial {x_j}^2} + \frac{1}{c_p}\frac{\partial \overline{{u_j}'\theta'}}{\partial x_j} + \frac{\overline{S}_\theta}{c_p\rho_a} \tag{3.36}$$

$$\frac{\partial \overline{c}}{\partial t} + \overline{u}_j\frac{\partial \overline{c}}{\partial x_j} - w_t\frac{\partial \overline{c}}{\partial z} = -k_p\frac{\partial^2 c_g}{\partial {x_j}^2} + \frac{\partial \overline{{u_j}'c'}}{\partial x_j} + \frac{\overline{S}_p}{\rho_a} \tag{3.37}$$

where $\tau_R = \overline{{u_j}'{u_i}'}$ is the Reynolds stress tensor in kinematic units. The system of the Reynolds averaged governing equations is then not closed as the turbulent fluxes, such as τ_R, $\overline{{u_j}'\theta'}$, $\overline{{u_j}'c'}$ are unknown. Therefore, this procedure needs closure schemes for turbulence fluxes.

The K-theory is a simple first-order closure, which is commonly used in numerical weather prediction models and relates the turbulent flux to the gradient of the variable X. For example, the vertical turbulent flux of u is

$$\overline{w'u'} = -K_m\frac{\partial \overline{u}}{\partial z} \tag{3.38}$$

Four parameterizations can be chosen in WRF, for instance, the specification of a constant K_m, 3D Smagorinsky, and prognostic TKE closure. The prognostic TKE closure applied to the RAS-filtered equations shares the same program framework but with different empirical coefficients.

In addition to the closure problem, the transport flux to the surface (or surface flux) is another important issue required to solve the governing equations for high-Reynolds-number turbulence. The next section will present the parameterization for this problem.

3.4 Atmosphere-Land-surface Model

The surface properties and surface fluxes are parameterized by combining two different physical modules: a land-surface parameterization calculates the evolution of surface properties, and a surface-layer parameterization calculates the surface fluxes. For the sake of simplicity, this thesis assumes that the surface properties are constant in time during the simulation. The interface between the atmosphere and the land is the surface layer, where turbulence varies by less than 10%. The surface layer is further divided into an inertial layer and a roughness sublayer. The flux of the inertial layer is calculated using the bulk transfer method as described below. The bulk transfer method is based on the MOST which assumes that the surface layer is stationary and horizontally homogeneous. The MOST hypothesis applied to wind yields

$$\frac{\partial U_a}{\partial z} = \frac{u_*}{kz}\phi_m\left(\zeta\right) \tag{3.39}$$

with the magnitude of the horizontal wind speed $U_a = \sqrt{u^2 + v^2}$, the dimensionless independent variable $\xi = z / L_O$, and ϕ_m the similarity function. Linking Equation (3.39) with the K-theory, the eddy viscosity is derived as

$$K_m = \frac{ku_* z}{\phi_m} \tag{3.40}$$

and the friction velocity in the lowest layer is

$$u_* = \frac{kU_a}{\ln\left(z / z_0\right) - \psi_m\left(z / L_O\right)} \tag{3.41}$$

where $\psi_m = \int_{z_0}^{z} \left(1 - \phi_m\right) \mathrm{d}\ln z$, and z_0 is the aerodynamic roughness length. The stress components along the x and y axis are $u / U_a \cdot \tau$ and $v / U_a \cdot \tau$, respectively.

Similarly, applying MOST, the eddy diffusivity for temperature, moisture is obtained as

$$K_h = K_q = \frac{ku_* z}{\phi_h} \tag{3.42}$$

where ϕ_h is the similarity function for heat and moisture. Upon substituting Equation (3.40) into Equation (2.18), the eddy diffusivity of dust particles is derived as

$$K_p = Sc_T \cdot \frac{ku_* z}{\phi_m} \tag{3.43}$$

However, the application of MOST in LES is questioned by Shao et al. (2013). They argue, for example, that ignoring the effects of advection does not hold at the atmospheric large eddy scale since the MOST similarity functions are empirically derived using average (e.g., over 15–30 min or over several kilometers) measurements. They also indicate that the MOST-based diffusivity and viscosity estimated in the surface layer are inconsistent with values from the closure model.

The surface flux for dust, i.e., the lower boundary condition for Equation (3.30) and Equation (3.37), is difficult to parameterize because the dust concentration very close to the surface is poorly obtained. Instead, the dust deposition velocity at a reference height is usually parameterized, as discussed in Section 2.2. Under the assumption of constant flux in the surface layer, the dust deposition flux can be calculated by a multiplication of the dust deposition velocity and the dust concentration at a reference height above the surface. Section 2.2 also shows that the dust deposition velocity is dependent on the friction velocity, which is a surrogate for the surface shear stress. Currently, the dust deposition schemes applying to weather scale simulation have only considered Reynolds stresses rather than instantaneous stresses. However, both updrafts and downdrafts of eddies produce instantaneous shear stress at the surface. The new deposition scheme that will be presented in this thesis considers the stochastic nature of dust deposition. This is achieved by taking into account the statistical distributions of the turbulent shear stress. Therefore, a distinction needs to be made between turbulent shear stress and Reynolds shear stress, which will be described in the next section (Section 3.5).

3.5 Shear stress derivation

The Reynolds shear stress is commonly used as the dominant driver of the dust deposition process in weather-scale simulations. Because dust particles respond to shear stress on much shorter time scales, Reynolds shear stress is not suitable for driving turbulent dust deposition. Instead, the instantaneous shear stress vector is applied, which in the kinematic unit is defined as

$$\vec{\tau}_f = uw\vec{i} + vw\vec{j} \tag{3.44}$$

By filtering in LES, the instantaneous wind component is decomposed into a grid-resolved component and a subgrid-scale component. Then Equation (3.44) is rewritten as

$$\begin{aligned}\vec{\tau}_f &= \left(u_g + u_{sg}\right)\left(w_g + w_{sg}\right)\vec{i} + \left(v_g + v_{sg}\right)\left(w_g + w_{sg}\right)\vec{j} \\ &= (\underbrace{u_g w_g}_{\tau_{g,x}} + \underbrace{u_g w_{sg} + u_{sg} w_g + u_{sg} w_{sg}}_{\tau_{sg,x}})\vec{i} + (\underbrace{v_g w_g}_{\tau_{g,y}} + \underbrace{v_g w_{sg} + v_{sg} w_g + v_{sg} w_{sg}}_{\tau_{sg,y}})\vec{j}\end{aligned} \tag{3.45}$$

where $\tau_{g,x}$ and $\tau_{g,y}$ are the grid-resolved shear stresses along the x- and y- axes, respectively, $\tau_{sg,x}$ and $\tau_{sg,y}$ are the SGS shear stress. Therefore, the grid-resolved shear stress is expressed as

$$\vec{\tau}_g = u_g w_g \vec{i} + v_g w_g \vec{j} \tag{3.46}$$

and the unsolved SGS shear stress is

$$\vec{\tau}_{sg} = \left(u_g w_{sg} + u_{sg} w_g + u_{sg} w_{sg}\right)\vec{i} + \left(v_g w_{sg} + v_{sg} w_g + v_{sg} w_{sg}\right)\vec{j} \tag{3.47}$$

which is parameterized.

Substituting Equation (3.46)-(3.47) into Equation (3.45) and comparing it with Equation (3.46) gives

$$\vec{\tau}_f = \left(\tau_{g,x} + \tau_{sg,x}\right)\vec{i} + \left(\tau_{g,y} + \tau_{sg,y}\right)\vec{j} \tag{3.48}$$

The magnitude of the instantaneous shear stress is calculated as follows

$$\tau_f = \left[\left(\tau_{g,x} + \tau_{sg,x}\right)^2 + \left(\tau_{g,y} + \tau_{sg,y}\right)^2\right]^{1/2} \tag{3.49}$$

As shown by Equation (2.2) and Equation (3.9), $u_{i,g}$ can be further decomposed into a Reynolds averaged term $\bar{u}_i$ and a turbulent fraction $\tilde{u}_i$ on scales larger than the filter grid size, as follows

$$u_{i,g} = \bar{u}_i + \tilde{u}_i \tag{3.50}$$

Substituting Equation (3.50) into Equation (3.46) gives

$$\vec{\tau}_g = \left(\overline{uw} + \overline{u}\tilde{w} + \tilde{u}\overline{w} + \tilde{u}\tilde{w}\right)\vec{i} + \left(\overline{vw} + \overline{v}\tilde{w} + \tilde{v}\overline{w} + \tilde{v}\tilde{w}\right)\vec{j} \tag{3.51}$$

As seen, the grid-resolved shear stresses include those due to interactions of advective winds ($\bar{u}_i\bar{w}$), interactions between advective winds and large eddies ($\tilde{u}_i\bar{w}$ and $\bar{u}_i\tilde{w}$), and interactions of large eddies ($\tilde{u}_i\tilde{w}$). The large-eddy scale shear stress is

$$\vec{\tilde{\tau}} = \left(\tilde{u}\tilde{w}\right)\vec{i} + \left(\tilde{v}\tilde{w}\right)\vec{j} \tag{3.52}$$

Substituting $u = \bar{u} + u'$, $v = \bar{v} + v'$ and $w = \bar{w} + w'$ into Equation (3.44) gives

$$\vec{\tau}_f = \left(\overline{u} + u'\right)\left(\overline{w} + w'\right)\vec{i} + \left(\overline{v} + v'\right)\left(\overline{w} + w'\right)\vec{j} \tag{3.53}$$

The Reynolds averaging of the instantaneous shear stress vector in the kinematic unit is denoted as $\overline{\vec{\tau}_f}$ and is derived as

$$\begin{aligned}
\overline{\vec{\tau}_f} &= \overline{\left(\overline{u} + u'\right)\left(\overline{w} + w'\right)}\vec{i} + \overline{\left(\overline{v} + v'\right)\left(\overline{w} + w'\right)}\vec{j} \\
&= \left(\overline{\overline{u}\,\overline{w}} + \overline{\overline{u}\,w'} + \overline{u'\,\overline{w}} + \overline{u'w'}\right)\vec{i} + \left(\overline{\overline{v}\,\overline{w}} + \overline{\overline{v}w'} + \overline{v'\overline{w}} + \overline{v'w'}\right)\vec{j} \\
&= \left(\overline{u}\,\overline{w} + \cancel{\overline{u}\,\overline{w'}} + \cancel{\overline{u'}\,\overline{w}} + \overline{u'w'}\right)\vec{i} + \left(\overline{v}\,\overline{w} + \cancel{\overline{v}\,\overline{w'}} + \cancel{\overline{v'}\,\overline{w}} + \overline{v'w'}\right)\vec{j} \\
&= \left(\overline{u}\,\overline{w} + \overline{u'w'}\right)\vec{i} + \left(\overline{v}\,\overline{w} + \overline{v'w'}\right)\vec{j}
\end{aligned} \tag{3.54}$$

where $\overline{u}\,\overline{w}$ and $\overline{v}\,\overline{w}$ are advective momentum fluxes, $\overline{u'w'}$ and $\overline{v'w'}$ are Reynolds stress components. If turbulence is completely random, then the positive $u'w'$ and $v'w'$ are instantly canceled by a negative $u'w'$ and $v'w'$, resulting in $\overline{u'w'} = \overline{v'w'} = 0$. However, there are situations where the average turbulent flux might be significantly different from zero. Comparing the advective fluxes to the eddy fluxes, it is important to recognize that $\overline{w} \cong 0$ throughout most of the boundary layer. Then the vertical advective fluxes are usually negligible compared to the vertical turbulent fluxes. Thus, $\overline{\vec{\tau}_f}$ becomes the vector of the Reynolds shear stress, and Equation (3.54) can be rewritten as

$$\vec{\tau}_R = \overline{\vec{\tau}_f} = \overline{u'w'}\,\vec{i} + \overline{v'w'}\,\vec{j} \tag{3.55}$$

The magnitude of $\vec{\tau}_R$ is determined by

$$\begin{aligned}
\tau_R &= \sqrt{\overline{u'w'}^2 + \overline{v'w'}^2} \\
&= \sqrt{\left(\overline{\vec{\tau}}_{f,x} - \overline{u}\,\overline{w}\right)^2 + \left(\overline{\vec{\tau}}_{f,x} - \overline{v}\,\overline{w}\right)^2} \\
&= \sqrt{\left(\overline{\vec{\tau}_{g,x}} + \overline{\vec{\tau}_{sg,x}} - \overline{u}\,\overline{w}\right)^2 + \left(\overline{\vec{\tau}_{g,y}} + \overline{\vec{\tau}_{sg,y}} - \overline{v}\,\overline{w}\right)^2}
\end{aligned} \tag{3.56}$$

Substituting Equation (3.51) for τ_g into Equation (3.56) gives

$$\tau_R = \left[\left(\overline{\tilde{\tau}}_x + \overline{\tau_{sg,x}}\right)^2 + \left(\overline{\tilde{\tau}}_y + \overline{\tau_{sg,y}}\right)^2\right]^{1/2} \tag{3.57}$$

This suggests that Reynolds shear stresses include the Reynolds average of shear stresses by large eddies $\overline{\tilde{\tau}}_x$ and the Reynolds average of SGS shear stresses $\overline{\tau_{sg,x}}$.

The expressions for both the vector and magnitude of the shear stress are summarized in Table 3-1. The instantaneous friction velocity and Reynolds averaged friction velocity are given as $u_{*f} = \sqrt{\tau_f}$ and $u_* = \sqrt{\tau_R}$, respectively.

Table 3-1: A list of definitions and expressions of the instantaneous, grid-resolved, subgrid, and Reynolds averaged shear stress in kinematic units.

Symbol	Mathematical expression	Physical meaning
$\vec{\tau}_f$	$\vec{\tau}_f = uw\vec{i} + vw\vec{j}$	Instantaneous momentum flux
	$\tau_f = \sqrt{\left(u_g w_g + \tau_{sg,x}\right)^2 + \left(v_g w_g + \tau_{sg,y}\right)^2}$	Magnitude of $\vec{\tau}_f$
$\vec{\tau}_g$	$\vec{\tau}_g = \rho_a \left(u_g w_g \vec{i} + v_g w_g \vec{j}\right)$	Grid-resolved instantaneous momentum flux
	$\tau_g = \rho_a \sqrt{\left(u_g w_g\right)^2 + \left(v_g w_g\right)^2}$	Magnitude of $\vec{\tau}_g$
$\vec{\tau}_{sg}$	$\vec{\tau}_{sg} = \rho_a \left(u_g w_{sg} + u_{sg} w_g + u_{sg} w_{sg}\right)\vec{i} + \left(v_g w_{sg} + v_{sg} w_g + v_{sg} w_{sg}\right)\vec{j}$	Subgrid instantaneous momentum flux; parameterized
	$\tau_{sg} = \sqrt{\tau_{sg,x}^2 + \tau_{sg,y}^2}$	Magnitude of $\vec{\tau}_{sg}$
$\vec{\tilde{\tau}}$	$\vec{\tilde{\tau}} = \left(\tilde{u}\tilde{w}\right)\vec{i} + \left(\tilde{v}\tilde{w}\right)\vec{j}$	Instantaneous large eddy scale shear stress
	$\tilde{\tau} = \sqrt{\left(\tilde{u}\tilde{w}\right)^2 + \left(\tilde{v}\tilde{w}\right)^2}$	Magnitude of $\vec{\tilde{\tau}}$
$\vec{\tau}_R$	$\vec{\tau}_R = \overline{u'w'}\,\vec{i} + \overline{v'w'}\vec{j}$	Reynolds shear stress
	$\tau_R = \sqrt{\left(\overline{\tau_{g,x}} + \overline{\tau_{sg,x}} - \overline{u}\,\overline{w}\right)^2 + \left(\overline{\tau_{g,y}} + \overline{\tau_{sg,y}} - \overline{v}\,\overline{w}\right)^2}$	Magnitude of $\vec{\tau}_R$

In the next chapter, a series of numerical experiments will be carried out to investigate the form of the shear stress distribution and to parameterize the effects of ABL stability on the shear stress distribution and the bulk deposition velocity at the kilometer scale.

4. Large-eddy-simulation of turbulent particle deposition and its dependency on atmospheric boundary-layer stability

Dust deposition velocities are enhanced in unstable ABLs (Damay, 2010; Gallagher et al., 1997; Nemitz and Sutton, 2004; Wesely et al., 1985a), and this enhancement is difficult to reproduce in current dust deposition models. The deposition velocity is dependent on the surface shear stress which is a stochastic quantity with statistical moments depending on the ABL stability. This thesis argues that it is the intermittency of turbulent shear stress that causes this enhancement. By considering the probability density distribution of shear stress, the dust deposition scheme can be improved. This is demonstrated by using WRF-LES/D, in which the instantaneous dust deposition flux and wind shear on the surface are simulated. In WRF-LES/D, the physics-based ZS14 scheme (as shown in Section 2.2.2) is applied and the deposition flux in each grid of the bottom layer at each time step can be computed using the ZS14 scheme with the transient shear stress in the same grid. This approach is chosen since it can explicitly resolve the large-eddy-scale motions of the turbulent flow while modelling the sub-filter motions. The ensemble mean of the dust deposition fluxes over all simulation grid cells and time steps divided by the ensemble mean of the dust concentration gives the so-called LES deposition velocity in this chapter. The Reynolds shear stress for the entire computational domain can also be calculated (see Section 3.5 for the derivation procedure). Thus, the Reynolds deposition velocity, which is the dust deposition velocity calculated by the ZS14 scheme using the Reynolds shear stress, referred to as the bulk deposition velocity, is obtained. A comparison of these two deposition velocities at different ABL stability shows the effect of ABL stability on the bulk deposition velocity.

Around this objective, this chapter is subdivided into three main sections. The first section (Section 4.1) describes the model setup and introduces a series of ABLs with different conditions of atmospheric stability and background wind. The results of the analysis in the second section (Section 4.2) cover five aspects, including the analysis of the instantaneous shear stress (Section 4.2.1) and deposition velocity at the surface (Section 4.2.2), a refinement of the ZS14 scheme by considering the effect of atmospheric stability (Section 4.2.3), the variation of the probability density distribution of the shear stress with distance from the surface (Section 4.2.4), a description of the shear stress probability density distribution over grassland (Section 4.2.5). The final section (Section 4.3) summarizes and compares the results of the previous sections.

4.1 LES experimental setup

In this section, a total of 52 cases of numerical experiments are performed with WRF-LES/D, as given in Table 4-1. These experiments include variations of the ABL stabilities and Reynolds friction velocities (defined as the square of the Reynolds shear, representative of background wind), as well as the roughness length. As shown, the surface heat flux varies case by case from -50 to 600 W m^{-2} for Exp (1-35), from 0 to 400 W m^{-2} for Exp (A1-A5), and from 0 to 600 W m^{-2} for Exp (36-47). The Reynolds friction velocity u_* increases from 0.1 to 0.4 m s^{-1} in Exp (1-20), from 0.15 to 0.5 m s^{-1} in Exp (21-35), from 0.15 to 0.3 m s^{-1} in Exp (A1-A5) and from 0.15 to 0.5 m s^{-1} in Exp (36-47). The roughness length z_0 for the sand surface used in Exp (1-20) is 0.153 mm according to the wind tunnel experiment (Zhang et al., 2014), but 0.76 mm for the desert in Exp (21-35) and Exp (A1-A5) according to the field observation in Niger in the Sahara desert (Bergametti et al., 2018). The wind speed at the upper boundary corresponding to each friction velocity is also given in Table 4-1. The vertical scaling velocity, w_*, of convective turbulence is determined by

$$w_* = \left(\frac{g}{\overline{\theta}} \frac{H_0}{\rho_a c_p} z_l \right)^{1/3} \tag{4.1}$$

where $\overline{\theta}$ is the Reynolds averaged potential temperature and z_l = 1000 m is the inversion height of the convective ABL. The scaling velocity w_* is roughly the updraft velocity of convective thermals and is often used in similarity theories for the convective boundary layers. Usually, w_* is not used for stable ABLs, but it is used here as an indicator of turbulence suppression by negative buoyancy. Furthermore, the density of dust particles is defined as ρ_p = 2650 kg m^{-3}. Exp (1-20) simulates the default dust sizes set in the WRF model, including 1.46, 2.8, 4.8, 9, and 16 μm, while Exp (21-35) extends the dust particle size range by additing four diameters of 0.04, 0.1, 0.2 and 0.5 μm.

Table 4-1: List of numerical experiments: wind speed at the top boundary (U) and vertical scaling velocity (w_*) are in m s^{-1}, and the unit of surface heat flux (H_0) is W m^{-2}.

H_0	w_*	z_0 = 0.153 mm			z_0 = 0.76 mm			z_0 = 10 cm		
		Name	u_*	U	Name	u_*	U	Name	u_*	U
-50	-1.12	Exp1	0.1	4	Exp21	0.15	5.44			
-50	-1.12	Exp2	0.2	8	Exp22	0.3	10.87			
-50	-1.12	Exp3	0.3	12	Exp23	0.5	18.12			
-50	-1.12	Exp4	0.4	16	–		–			
0	0	Exp5	0.1	4	EXP24, ExpA1	0.15	5.44	Exp36	0.15	3.6
0	0	Exp6	0.2	8	EXP25, ExpA4	0.3	10.87	Exp37	0.3	7.2
0	0	Exp7	0.3	12	EXP26	0.5	18.12	Exp38	0.5	11.9
0	0	Exp8	0.4	16	–					
200	1.77	Exp9	0.1	4	EXP27, ExpA2	0.15	5.44	Exp39	0.15	3.6
200	1.77	Exp10	0.2	8	EXP28, ExpA5	0.3	10.87	Exp40	0.3	7.2
200	1.77	Exp11	0.3	12	EXP29	0.5	18.12	Exp41	0.5	11.9
200	1.77	Exp12	0.4	16	–		–			
400	2.23	Exp13	0.1	4	EXP30, ExpA3	0.15	5.44	Exp42	0.15	3.6
400	2.23	Exp14	0.2	8	EXP31	0.3	10.87	Exp43	0.3	7.2
400	2.23	Exp15	0.3	12	EXP32	0.5	18.12	Exp44	0.5	11.9
400	2.23	Exp16	0.4	16	–		–			
600	2.55	Exp17	0.1	4	EXP33	0.15	5.44	Exp45	0.15	3.6
600	2.55	Exp18	0.2	8	EXP34	0.3	10.87	Exp46	0.3	7.2
600	2.55	Exp19	0.3	12	EXP35	0.5	18.12	Exp47	0.5	11.9
600	2.55	Exp20	0.4	16	–		–			

Idealized vertical profiles of the wind speed, potential temperature, and dust concentration are used to initialize the WRF-LES/D model, with examples shown in Figure 4-1(a-c). The wind speed follows a logarithmic profile determined by the roughness length and Reynolds friction velocity, as provided in Table 4-1. Additionally, the initial vertical profile of dust concentration for each dust size bin is assumed to be logarithmic, following the methodology outlined by Chamberlain (1967) and Kind (1992), as follows

$$c(z) = \frac{35.88}{\kappa} \ln \frac{z}{z_0} \tag{4.2}$$

where z_0 is the roughness length, and the coefficient of 35.88 is defined based on field observations over a desert surface by Bergametti et al. (2018).

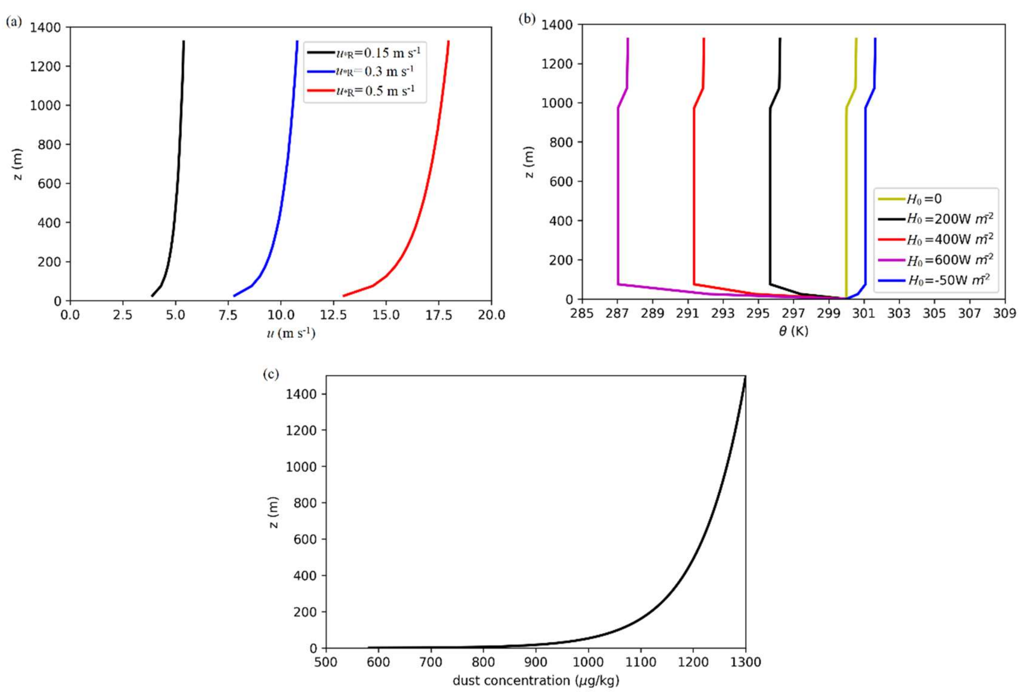

Figure 4-1: (a) The initial profiles of wind speed are characterized by Reynolds friction velocities of 0.15, 0.3, and 0.5 m s^{-1}, respectively (i.e., Exp24, 25, 26). (b) The initial potential temperature profiles vary as H_0 changes from -50 Wm^{-2} to 600 W m^{-2}. (c) The initial dust concentration profile is determined by Equation (4.2) with z_0 = 0.153 mm.

The computation setup in WRF-LES/D is summarized in Table 4-2. The model domain covers a flat area of 2 × 2 km^2. As discretization and subgrid-scale-model errors tend to increase with decreasing resolution (Chow and Moin, 2003; Meyers and Sagaut, 2007), it is crucial to choose a resolution fine enough to minimize these errors. The size of the simulated domain should also be large enough to contain the relevant boundary-layer structures.

The upper boundary of the domain is set at 1.5 km above the ground surface, assumed to be sufficient for fully developing the ABL structures. To balance computational costs, this study aims for a resolution that is as coarse as possible yet sufficiently fine. Following Klose and Shao (2013), the model domain ($2 \times 2 \times 1.5$ km^2) in this study is covered by $200 \times 200 \times 90$ grids, corresponding to a horizontal resolution of $\Delta x = \Delta y = 10$ m. In the vertical direction, the grid spacing varies from the surface to the top of the boundary layer. The lowest model layer has a depth of 1 m, with layers above it stretched logarithmically with respect to height (z). Lateral boundary conditions are periodic, enabling the creation of a fully developed ABL. For upper boundary conditions, constant pressure and zero vertical velocity are set. Rayleigh damping with a factor of 0.01 is applied to the layer between 1.2 km and 1.5 km.

Surface roughness elements are assumed to be uniformly distributed. Each simulation defines a fixed heat flux from the surface, and no radiation model is activated. The ZS14 dust deposition scheme is used, with no active dust emission scheme. The computation of momentum flux within the lowest grid layer employs the MOST. The Arakawa-C staggered grid is utilized. The simulation time for each experiment (EXP) is 90 minutes, with a time step of 0.05 s and an output interval of 10 s. The first 30 minutes of the simulation serve as model spin-up time, and data from the remaining 60 minutes is used for the analysis.

On this basis, eddies in ABL with varying stabilities can be generated. Each grid provides transient surface shear stress and dust deposition flux due to eddies. The next section will offer an in-depth exploration of the ABL eddies and the analysis of the simulations.

Table 4-2: Settings of model simulation.

Characteristic	Options
Surface layer scheme	MOST
Domain size	$2 \times 2 \times 1.5$ km^3
Horizontal resolution	$\Delta x = \Delta y = 10$ m
Vertical resolution	Exp(1-47): logarithmically stretched with Δz varying from 1 m in the bottom layer; Exp(A1-A5): logarithmically stretched above 51 m, $\Delta z = 1$ m in the bottom layer, $\Delta z = 2$ m from 1 m to 51 m
Grid	$200 \times 200 \times 90$
Time step	0.05 s
Simulation period	90 min
Boundary conditions	Lateral: Periodic Upper: Constant pressure with zero vertical velocity

4.2 Results

Figure 4-2 (a-c) shows examples of the instantaneous shear stress and dust deposition flux from Exp 1 (stable condition), Exp5 (neutral condition), and Exp9 (unstable condition), respectively, all initiated with an initial background wind of 4 m s^{-1}. In Figure 4-2a, the instantaneous shear stresses exhibit high homogeneity, indicating the suppression of large vertical vortices in the vertical direction due to inverted buoyancy. Comparatively, Figure 4-2b shows a greater variation in instantaneous shear stress than that seen in Exp1, yet retains essential horizontal homogeneity. Moving to Figure 4-2c, the transient shear stress is more dispersed, marked by localized stronger shear stresses. This behavior arises from buoyancy-induced large eddies that intermittently elevate local stresses. Moreover, this intermittently occurring strong shear stress contributes to significant dust deposition flux, as demonstrated in Figure 4-2c.

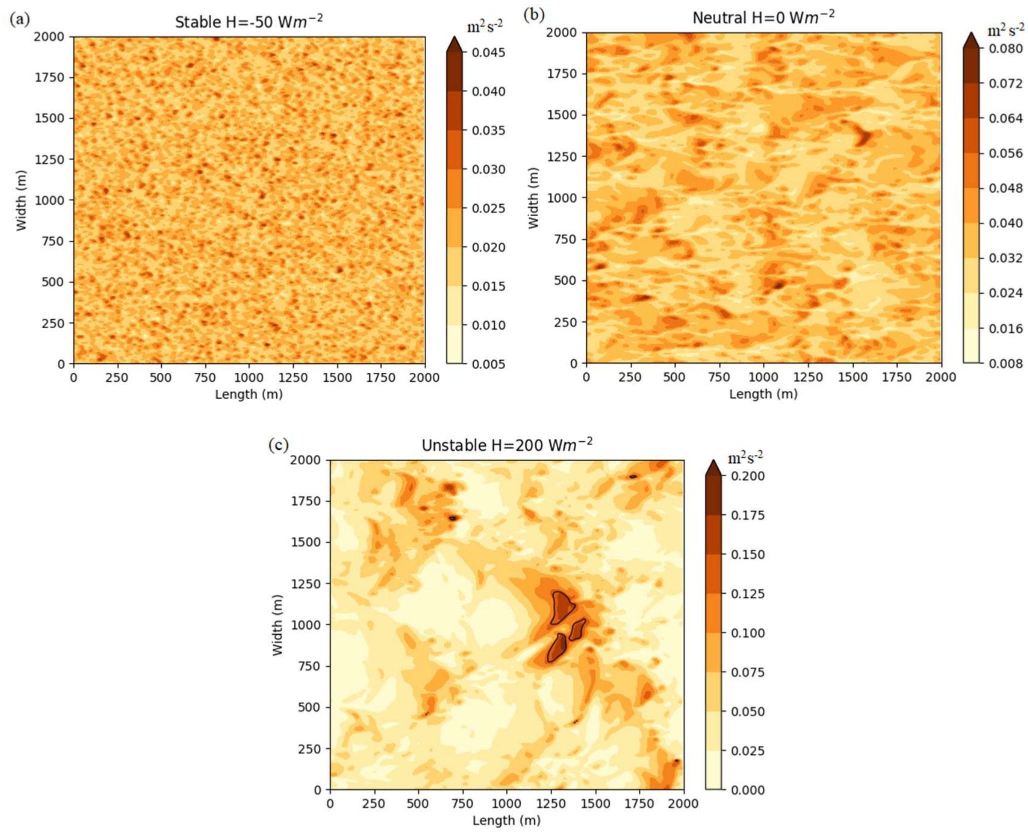

Figure 4-2: The instantaneous shear stress (color shaded) and dust deposition flux (contour, $F_d > 1$ μg $m^{-2}s^{-1}$) within the computational bottom layer for conditions of (a) H_0 = -50 Wm^{-2}; (b) for $H_0 = 0$; (c) for $H_0 = 200$ Wm^{-2}.

The effects of large eddies on dust deposition become more apparent in Figure 4-3. This figure presents a vertical cross-section showcasing velocity vectors (u', w') and dust concentration (depicted in Figure 4-3a), along with the corresponding dust deposition velocity (shown in Figure 4-3b). Figure 4-3a reveals the presence of vertically rotating vortices, accompanied by relatively robust updrafts and downdrafts. Both updrafts and downdrafts contribute to higher dust deposition velocities for dust particles with a size of 1.46 μm. Furthermore, due to the coherent structure of these large eddies, downward airflow carries elevated concentrations of dust from the upper to lower levels, resulting in enhanced dust deposition. Hence, to achieve a comprehensive grasp of turbulent deposition, it becomes imperative to delve into the characterization of turbulent shear stresses.

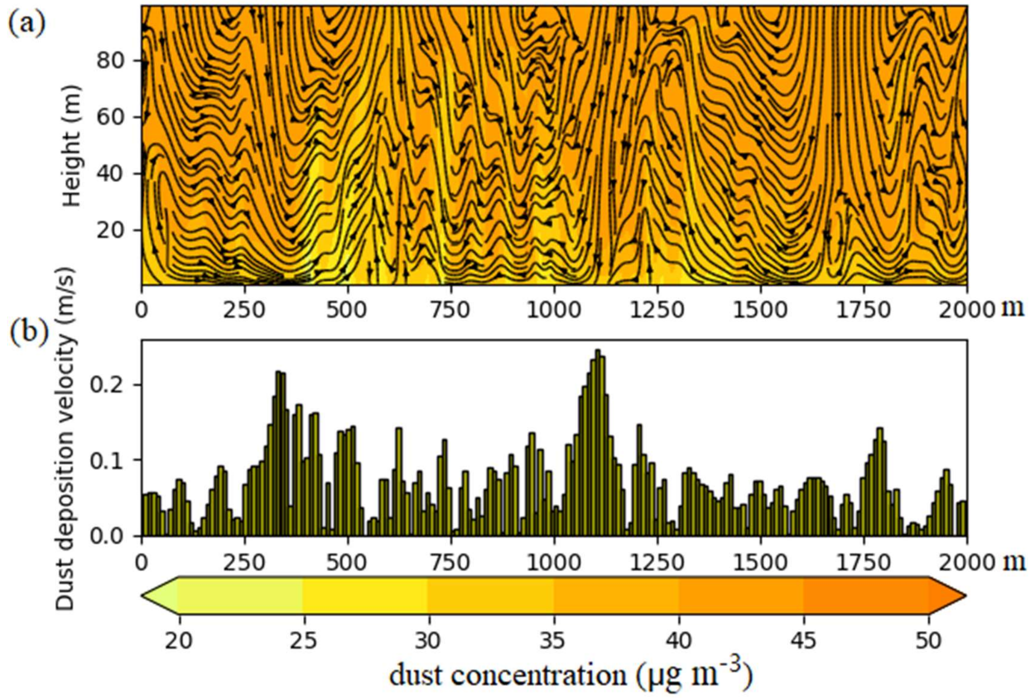

Figure 4-3: (a) Cross-section of the airflow components (u', w', in m s^{-1}). (b) The dust deposition velocity (in m s^{-1}).

4.2.1 Turbulent shear stress

In this first set of analyses, we examine the influence of atmospheric stability on surface shear stress, including both the fluctuation and mean value. The instantaneous shear stress is calculated for each grid in the bottom layer using Equation (3.49). Subsequently, the space-and-time averaged total momentum flux $\overline{\tau}_f$, grid-resolved momentum flux $\overline{\tau}_g$, and subgrid momentum flux $\overline{\tau}_{sg}$ are calculated as follows

$$\overline{\tau}_f = \frac{1}{N_x N_y N_t} \sum_{n_x n_y n_t} \tau_f \left(n_x, n_y, n_t\right) \tag{4.3}$$

etc., where N_x (=200) and N_y (=200) are the numbers of grid points in the x- and y-direction, respectively, and N_t (=360) are the time steps of the model output. Figure 4.4 illustrates an example of the vertical profiles of $\overline{\tau}_f$, $\overline{\tau}_g$, $\overline{\tau}_{sg}$ and τ_R obtained from Exp28. The value of τ_R is calculated using Equation (3.56). As can be seen, $\overline{\tau}_f$ substantially differs from τ_R. As the distance from the surface increases, τ_R remains almost constant while $\overline{\tau}_f$ increases. Near to surface, $\overline{\tau}_f$ is dominated by SGS shear stresses compared to grid-resolved shear stress. As height increases, $\overline{\tau}_{sg}$ decreases slightly, while $\overline{\tau}_g$

increasing rapidly, and then $\overline{\tau}_f$ is determined by $\overline{\tau}_g$. This is because as height increases, turbulence is increasingly resolved by the grid.

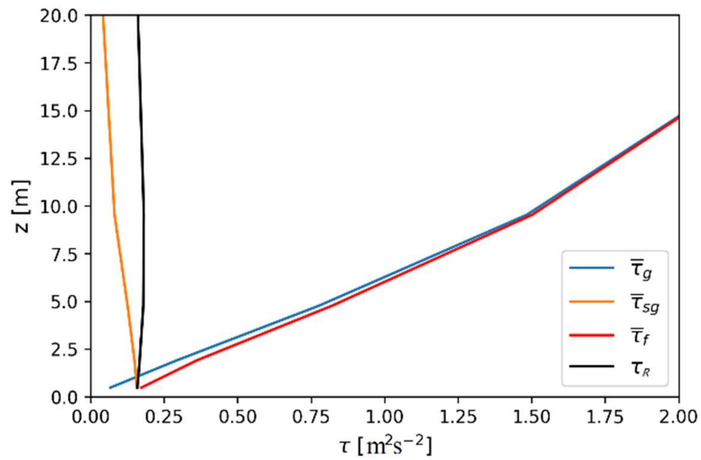

Figure 4-4: Vertical profiles of τ_R, $\overline{\tau}_f$, $\overline{\tau}_g$ and $\overline{\tau}_{sg}$ from the WRF-LES/D simulation Exp28.

Since the wind speed at the surface is zero in WRF-LES/D, the contribution of grid-resolved shear stress to the surface shear stress can be disregarded in comparison to the subgrid shear stress. As a result, the magnitude of the instantaneous shear stress at the surface can be expressed in kinematic units as

$$\tau_f = \left[\left(\tau_{sg,x} \right)^2 + \left(\tau_{sg,y} \right)^2 \right]^{1/2} \tag{4.4}$$

And the Reynolds averaged shear stress from Equation (3.56), i.e., $\tau_R = \left[\left(\overline{\tilde{\tau}_x} + \overline{\tau_{sg,x}} \right)^2 + \left(\overline{\tilde{\tau}_y} + \overline{\tau_{sg,y}} \right)^2 \right]^{1/2}$, can be rewritten as

$$\tau_R = \left[\left(\overline{\tau_{sg,x}} \right)^2 + \left(\overline{\tau_{sg,y}} \right)^2 \right]^{1/2} \tag{4.5}$$

Figures 4-5(a-c) give the instantaneous surface shear stress, τ_f, of a sample grid (n_x = 198, n_y = 41) over one hour for the runs with z_0 = 0.153 mm, U = 4 m·s^{-1} and the surface heat flux H_0 being 0, 200, 600 W·m^{-2}, respectively. Figures 4.5(d-f) are the same as Figures 4-5(a-c) but for a higher initial wind speed U = 16 m·s^{-1}. The panel indicates that τ_f is not constant with time, and the Reynolds averaged shear stress, as well as the shear stress fluctuations, increase with increasing atmospheric instability. In addition, the insert plots in Figure 4-5 show that the autocorrelation functions, ACF, oscillate as they decay with correlation time. As can be seen, the oscillation periodicity is longer under weak wind conditions (Figure 4-5(a-c)) than under strong wind (Figure 4-5(d-f)). In addition, the ACF in neutral conditions decreases more rapidly than in convective conditions. Retrieve Robinson (1991)'s definition of coherent motion: Correlations between variables observed over an extended temporal span, surpassing the minutest flow scales, serve as indicative manifestations of coherent oscillatory motion. Thus, the regular oscillation and long-time correlation of τ_f are closely related to the evolution of the coherent structure. This indicates that in a convective ABL, stronger large-scale coherent structures exist under weak wind conditions.

To gain insight into the behavior of the unsteady shear stress field, the turbulent intensity of surface shear stress (TI-S) is introduced here. TI-S is defined as the ratio of the standard deviation of fluctuating surface shear stress, σ_τ, to the Reynolds shear stress τ_R,

$$\text{TI-S} = \frac{\sigma_\tau}{\tau_R} \tag{4.6}$$

with σ_τ is obtained from

$$\sigma_\tau = \sqrt{\overline{\left(\tau_f - \tau_R\right)^2}} \tag{4.7}$$

As shown in Figure 4-5, TI-S increases as atmospheric conditions become more unstable when the background wind is similar. However, with the same ABL stability, TI-S decreases as the background wind increases. A summarization of TI-S for Exp (1-20) is given in Table 4-3. High wind speeds tend to force the value of TI-S closer to that of neutral ABLs, as the mean-wind-induced shear stress becomes dominant over the large-eddy-induced shear-stress fluctuations. For a weak TI-S, $\overline{\tau}_f$ is dominated by τ_R and the mean of shear stress fluctuations is small compared to τ_R. As TI-S increases, the contribution of momentum transport by large eddies becomes significant. This is because in unstable ABLs, buoyancy-generated large eddies penetrate to high levels and intermittently enhance the momentum transfer to the surface, see Figure 4-3.

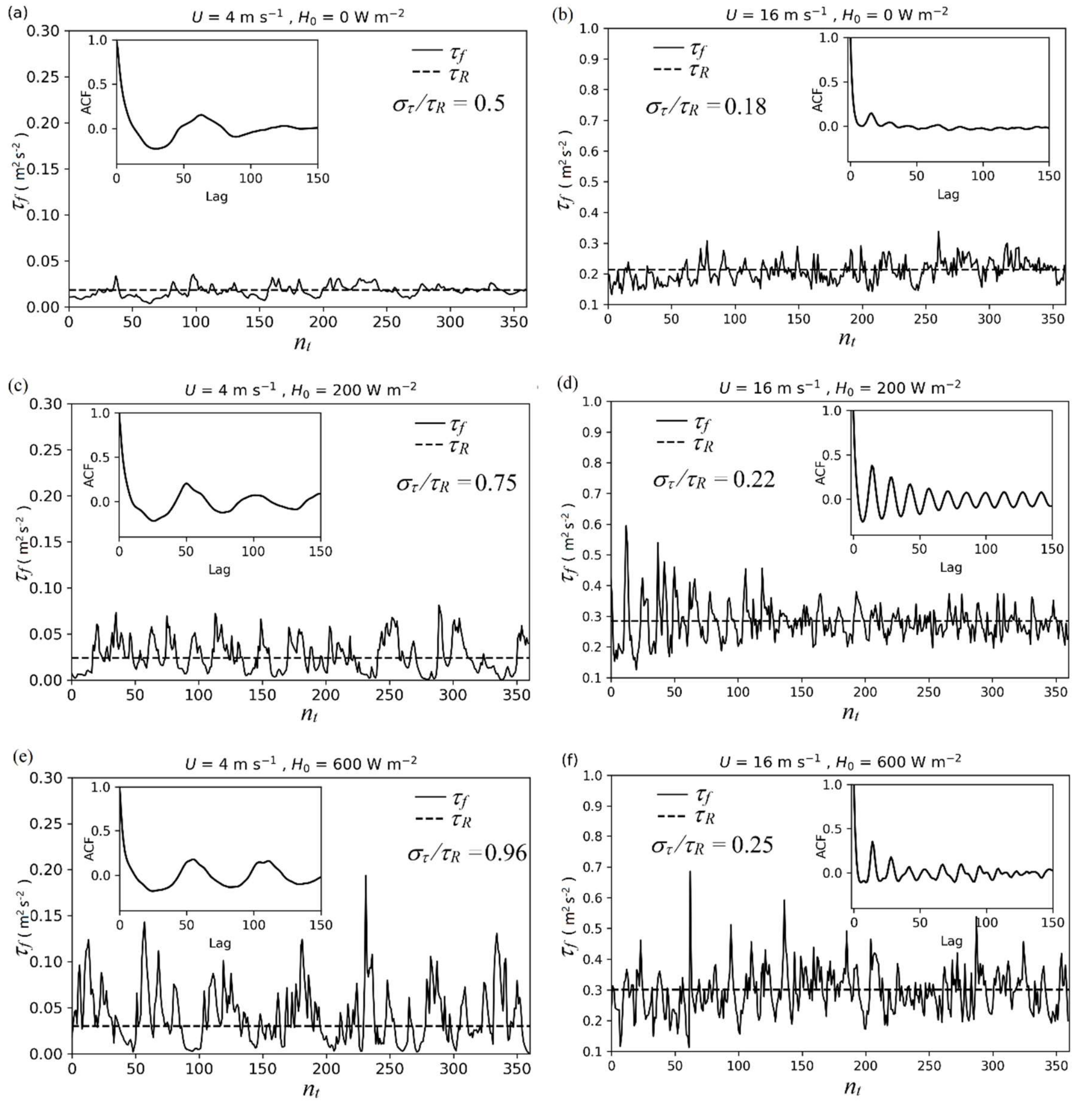

Figure 4-5: Time evolutions of surface shear stress τ_f with different H_0 values and z_0 = 0.153 mm at the grid point n_x = 198 and n_y = 41 (a-c) for U = 4 m s^{-1}; (d-f) for U = 16 m s^{-1}; the insert plots are the autocorrelation functions of τ_f.

4.2.2 Turbulent particle deposition

The intermittently enhanced surface shear stress can directly lead to stronger localized particle deposition. Therefore, similar to surface shear stress, dust deposition is also intermittent in space and time. In addition, the deviation $\tau_R - \overline{\tau}_f$ in Figure 4-4 shows Reynolds shear stress significantly differs from the instantaneous turbulence. However, to our knowledge, in existing dust deposition schemes, the dust deposition velocity is calculated using only the Reynolds shear stress τ_R instead of the instantaneous shear stress.

Let V_{d,τ_R} be the Reynolds-averaged deposition velocity, which is calculated by the ZS14 scheme using τ_R. And let $V_{d,\,LES}$ be the bulk deposition velocity from WRF-LES/D simulation. According to the method commonly used in field and wind experiments, $V_{d,\,LES}$ is expressed as the ratio of the ensemble average of particle deposition flux and the ensemble average of particle concentration, as follows

$$V_{d,LES} = -\frac{\bar{F}_d}{\bar{c}} \tag{4.8}$$

Analogous to the turbulent intensity of surface shear stress TI-S, a turbulence intensity of deposition velocity TI-V:

$$\text{TI-V} = \frac{\sigma_{V_d}}{V_{d,LES}} \tag{4.9}$$

To quantify the difference between V_{d,τ_R} and $V_{d,\,LES}$, a relative difference between these two deposition velocities, $RE\left(V_{d,LES}, V_{d,\tau_R}\right)$, is introduced, defined as

$$RE\left(V_{d,LES}, V_{d,\tau_R}\right) = \left|\frac{V_{d,LES} - V_{d,\tau_R}}{V_{d,LES}}\right| \times 100\% \tag{4.10}$$

The relative differences can be further linked to the ABL stability specified for each of the numerical experiments.

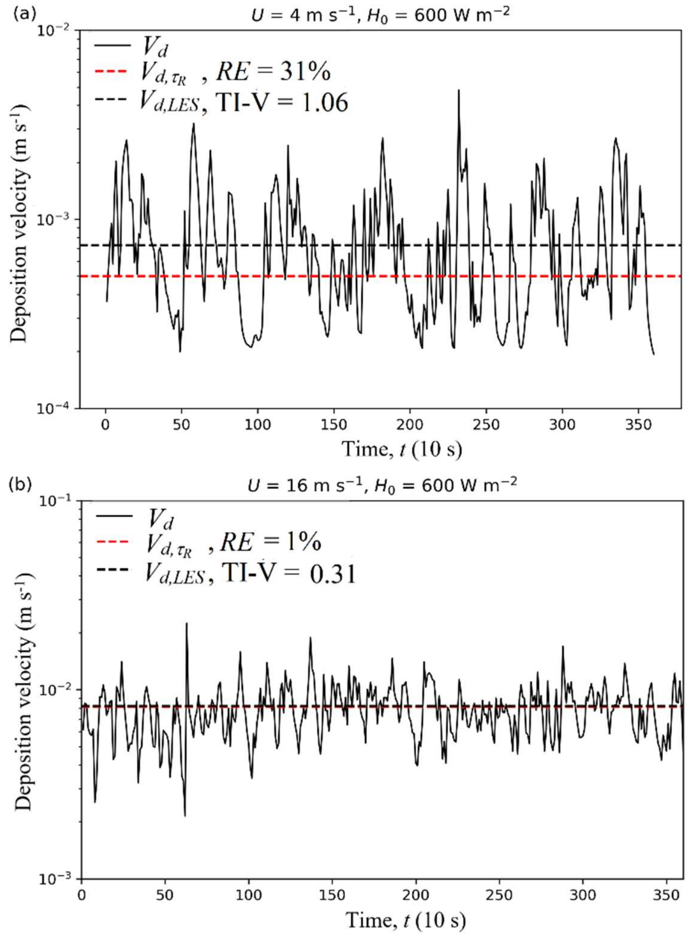

Figure 4-6: Time evolutions of deposition velocity V_d at grid point $n_x = 198$, $n_y = 41$ when H_0 = 600 W m^{-2}, z_0 = 0.153 mm and (a) U = 4 m s^{-1} and (b) U = 16 m s^{-1}. $RE\left(V_{d,LES}, V_{d,\tau_R}\right) = \left|\frac{V_{d,LES} - V_{d,\tau_R}}{V_{d,LES}}\right| \times 100\%$ is the relative difference between V_{d,τ_R} and $V_{d,LES}$, $\sigma_{V_d} / V_{d,LES}$ is the ratio of the standard deviation of simulated instantaneous deposition velocity V_d and mean deposition velocity, $V_{d,LES}$.

Figures 4-6(a-b), with the same wind conditions and surface heat fluxes as in Figures 4-5c and 4-5f, show the time evolution of the instantaneous deposition velocity V_{d,τ_f} for particles with a diameter of 1.46 μm. This particle size was chosen because it is the most sensitive to turbulent diffusion compared to the other default four sizes (2.8, 4.8, 9, 16 μm) in WRF-LES/D in Exp (1-20). The fluctuating behavior of V_{d,τ_f} is consistent with that of τ_f qualitatively. The comparisons of the TI-S in Figures 4-5e and 4-5f with the TI-V in Figures 4-6a and 4-6b show that TI-S and TI-V are positively correlated, i.e., an increase in TI-S leads to an increase in TI-V. In addition, Figure 4-6a shows that there is a substantial difference between $V_{d,LES}$ and V_{d,τ_R} and the $RE\left(V_{d,LES},V_{d,\tau_R}\right)$ reaches 31%. While in Figure 4-6b, V_{d,τ_R} is similar to $V_{d,LES}$ with the $RE\left(V_{d,LES},V_{d,\tau_R}\right)$ of only 1%. The value of the relative difference, $RE\left(V_{d,LES},V_{d,\tau_R}\right)$, depends on wind conditions, atmospheric stabilities, and particle sizes. It increases obviously with increased atmospheric instability under weak wind conditions, while it becomes less sensitive to stability when the wind is strong. Relating $RE\left(V_{d,LES},V_{d,\tau_R}\right)$ to the TI-S and the TI-V, it is easy to see that the ZS14 scheme with Reynolds shear stress, V_{d,τ_R}, can more accurately estimate the deposition velocity for low TI-S but underestimates the deposition velocity for high TI-S. The deviation of dust deposition velocity for high TI-S is due to the important role of gusty wind in particle deposition, which is not accurately reflected by V_{d,τ_R}. Therefore, in order to accurately estimate particle deposition, the shear stress variations in the dust deposition mechanism should be considered. The following first describes and parameterizes the turbulent surface shear stress.

As one of the main predisposing factors for aeolian processes, turbulent shear stress has attracted increasing attention in recent years (e.g., Klose et al., 2014; Li et al., 2020; Liu et al., 2018; Rana et al., 2020; Zheng et al., 2020). Similar to previous studies, we use the probability density distribution function $p(\tau_f)$ to characterize the stochastic variable τ_f. Figure 4-7(a-d) show the distributions of τ_f from Exp (1-20). As seen, the variability of τ_f increases with increasing atmospheric instability when the background winds are similar. The statistic moments of τ_f, including its Reynolds averaged value τ_R, standard deviation σ_τ, and skewness γ_1 of Exp (1-20) are summarized in Table 4-3. As shown, both σ_τ and τ_R increase with the increased ABL instability. $\gamma_1 > 0$ means the distribution of τ_f is positively skewed. Positive skewness is characterized by the distribution having a longer positive tail as compared with the negative tail and the distribution appears as a left-leaning (i.e., tends toward low values) curve. This indicates that large negative fluctuations are not as frequent as large positive fluctuations. The data also shows γ_1 generally shows a downward trend as TI-S decreases, which is consistent with Monahan (2006), i.e., as TI-S decreases, $p(\tau)$ becomes increasingly Gaussian. In addition, Figures

4-7 show that τ_R slightly increases with the ABL instability. The analysis of EXP (21-35) is carried out in the same way as EXP (1-20) and is not described in detail here.

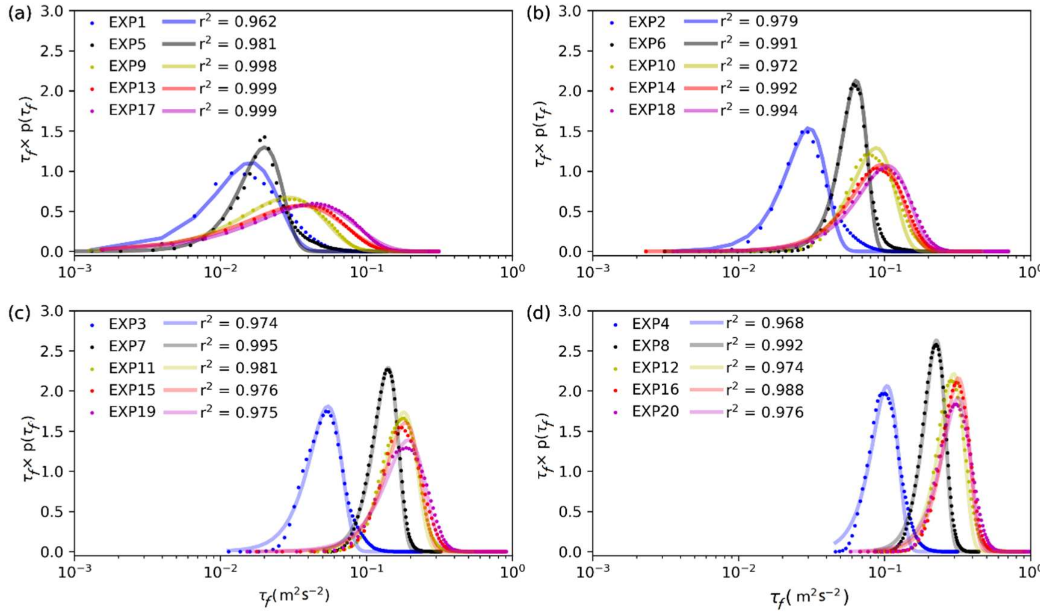

Figure 4-7: Probability density functions derived from WRF-LES/D simulated surface shear stress (dots) and the corresponding fitted Weibull density functions (solid lines, r^2 is the coefficient of determination) for different surface heat fluxes and different wind speeds: (a) U = 4 m s^{-1}, (b) U = 8 m s^{-1}, (c) U = 12 m s^{-1}, (d) U = 16 m s^{-1} with z_0 = 0.153 mm.

There are several shear stress distribution descriptions have been proposed in the literature. For instance, Klose et al. (2014) employed large-eddy simulations to establish that τ_f in unstable conditions adheres to a Weibull distribution. Shao et al. (2020), drawing insights from the Japan-Australian Dust Experiment data, demonstrated that $p(u_{*f})$ is reasonably Gaussian, albeit with a skew towards smaller values-signifying positive skewness-based on field observations. Li et al. (2020) suggested that τ_f in neutral conditions is Gauss distributed based on a wind-tunnel experiment. Colella and Keith (2003) hypothesized that turbulent shear flows deviate from Gaussian behavior due to nonlinear eddy interactions, thereby accounting for variations in shear stress distribution expressions.

Our findings indicate that the Gaussian approximation falls short in accurately capturing the skewed nature of $p(u_{*f})$, particularly in scenarios of heightened turbulence intensity (as exemplified by the unstable cases in Figure 4-7a). Consequently, we resort to approximating $p(\tau_f)$ through the utilization of a Weibull distribution as follows:

$$p(\tau_f) = \frac{\alpha}{\beta}\left(\frac{\tau_f}{\beta}\right)^{\alpha-1} \exp\left(-\left(\tau_f/\beta\right)^{\alpha}\right) \tag{4.11}$$

where α and β are the shape and scale parameters, respectively. The values of α and β for the numerical experiments Exp (1-20) are given in Table 4-3. It can be seen that both α and β depend not only on bulk wind conditions but also on the ABL stability. In addition, β is mainly determined by wind speed when the wind is strong, while it is affected by the ABL stability when the wind is weak. The behavior of α and β are shown in Figure 4-8. $|1/L_o|$ is the absolute value of the reciprocal of the Obukhov length L_o. Using the specified surface heat flux in the LES experiments, Equation (2.5) can be rewritten as

$$L_o = -\frac{\bar{\theta} u_*^{\,3}}{\kappa g \dfrac{H_0}{\rho_a c_p}} \tag{4.12}$$

Figure 4-8a shows that in both stable and unstable atmospheric conditions, analysis shows that the scale parameter α is related to the ABL stability as the power of $|1/L_o|$. As can be seen, α decreases as $|1/L_o|$ increases, satisfying Equation (4.13) approximately. For neutral conditions, L_o goes to infinity, Equation (4.13) no longer applies. Therefore, the shape parameter obtained by the fitting from Equation (4.13) was directly used for the pdf reproduction for the neutral cases instead of the approximated α obtained from Equation (4.13) which is applicable for stable and unstable conditions. The scaling parameter, β, depends on both the friction velocity of u_* ($=\sqrt{\tau_R/\rho_a}$) and the vertical scaling velocity w_*. Specifically, β increases linearly with $u_*^2 + 0.001 w_*^2$, as shown in Figure 4-8b. The relationship can be well approximated by Equation (4.14).

$$\alpha = 5.39 \cdot \exp\left(-5.43 \cdot |L_o|^{-2/3}\right) + 1.42 \tag{4.13}$$

$$\beta = 1.058 \cdot \left(u_*^2 + 0.001 w_*^{\,2}\right) \tag{4.14}$$

Table 4-3: Statistics of shear stress for numerical experiments Exp (1-20).

NAME	H_0	U	τ_R	σ_τ	σ_τ/τ_R	γ_1	α	β	$1/L_O$
Exp1	-50	4	0.0156	0.0086	0.554	1.902	2.026	0.011	0.475
Exp2	-50	8	0.0295	0.0096	0.327	1.573	3.154	0.023	0.153
Exp3	-50	12	0.0524	0.0115	0.22	1.029	3.923	0.044	0.06
Exp4	-50	16	0.1009	0.0158	0.157	0.835	4.819	0.09	0.02
Exp5	0	4	0.0185	0.0093	0.5	1.896	3.049	0.017	0
Exp6	0	8	0.0604	0.0151	0.25	1.142	5.004	0.055	0
Exp 7	0	12	0.1315	0.0266	0.202	0.166	5.383	0.122	0
Exp 8	0	16	0.2136	0.038	0.178	0.087	6.191	0.196	0
Exp 9	200	4	0.024	0.018	0.75	1.142	1.56	0.025	-0.696
Exp10	200	8	0.0812	0.0325	0.4	1.02	3.022	0.076	-0.11
Exp11	200	12	0.1676	0.0451	0.269	0.512	4.078	0.156	-0.037
Exp12	200	16	0.2848	0.0624	0.219	0.766	5.214	0.259	-0.017
Exp13	400	4	0.026	0.0248	0.955	1.127	1.302	0.03	-1.258
Exp14	400	8	0.0825	0.0372	0.451	0.646	2.513	0.081	-0.216
Exp15	400	12	0.1728	0.0522	0.302	0.677	3.776	0.160	-0.071
Exp16	400	16	0.2992	0.0646	0.216	0.289	5.214	0.278	-0.031
Exp17	600	4	0.0299	0.0287	0.96	1.083	1.303	0.035	-1.575
Exp18	600	8	0.0894	0.0424	0.474	0.715	2.472	0.089	-0.29
Exp19	600	12	0.1767	0.0604	0.342	0.614	3.252	0.167	-0.103
Exp20	600	16	0.3003	0.0739	0.246	0.511	4.493	0.277	-0.046

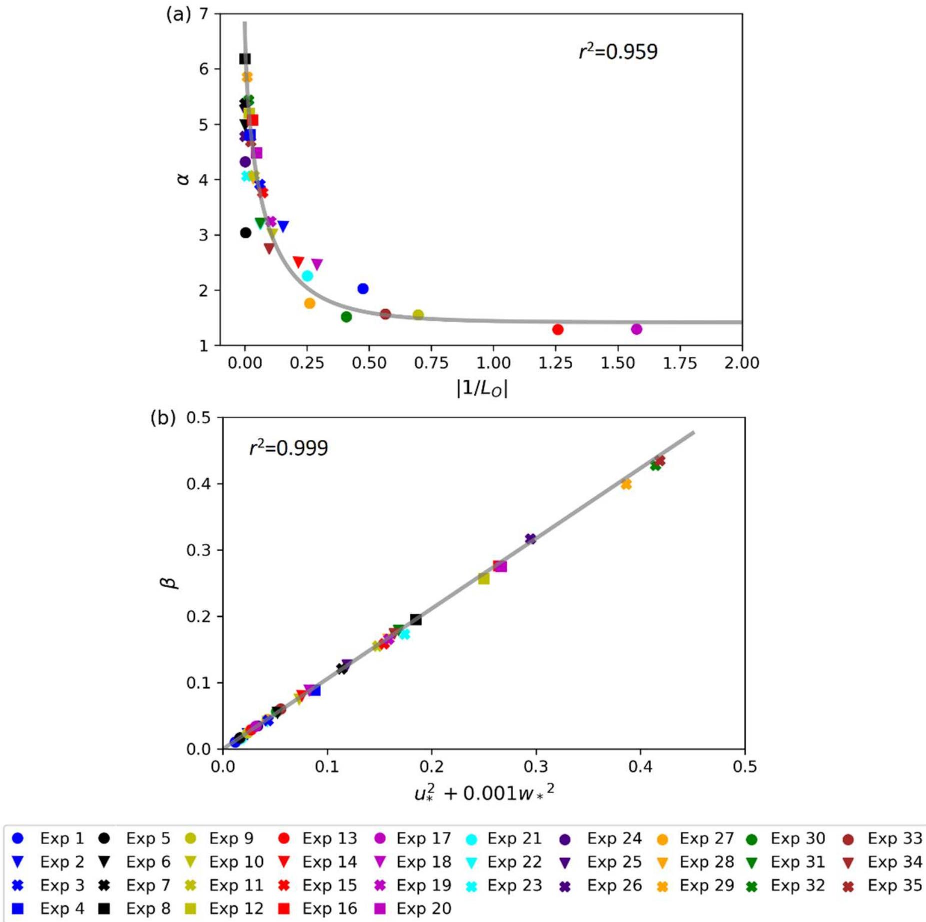

Figure 4-8: (a) Dependency of the shape parameter α on $1/L_O$ for all numerical experiments Exp (1-35); (b) Dependency of scaling parameter β on $\left(u_*^2 + 0.001w_*^2\right)$ for Exp (1-35).

Accordingly, if the macroscopic meteorological conditions, including Reynolds shear stress, heat flux, and vertical scaling velocity, are known, the corresponding turbulent surface shear stress distribution for non-neutral ABL can be obtained from Equations (4.11)-(4.14).

4.2.3 Improvement to particle deposition scheme

Figure 4-9 displays instances showcasing the performance of WRF-LES/D. Within the figure, the mean deposition velocities simulated from Exp (5, 7, 25) using WRF-LES/D, $V_{d,LES}$, are compared with the data from wind tunnel experiments (Zhang et al., 2014) and field observations (Bergametti et al., 2018). Notably, these experimental observations were conducted under neutral ABL conditions, featuring a Reynolds friction velocity u_*

akin to that of the numerical experiments. As depicted, the simulation results exhibit strong agreement with the observed data.

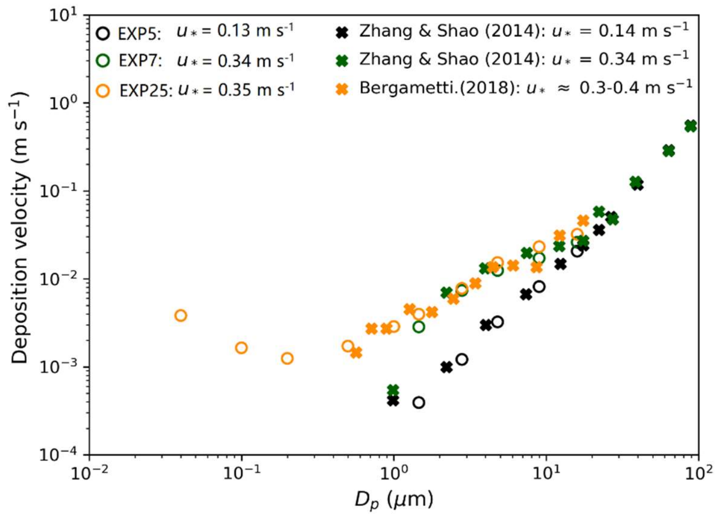

Figure 4-9: Validation of the simulated deposition velocity from WRF-LES/D (circles) by comparing with the observation data (crosses).

Through a comparison of the deposition velocity obtained using the ZS14 scheme V_{d,τ_R} with $V_{d,LES}$, we observed a diminishing accuracy of the ZS14 scheme as the ABL instability increases within weak background winds. To illustrate, consider the left sub-figure in Figure 4-10, which contrasts the $V_{d,LES}$ from Exp (5, 9, 17) with the V_{d,τ_R} from the same simulations. The background winds in Exp (5, 9, 17) are of a comparable magnitude. Similarly, the comparisons of $V_{d,LES}$ and V_{d,τ_R} for Exp (24, 27, 33) are provided in the right sub-figure of Figure 4-10.

Both sub-figures in Figure 4-10 clearly demonstrate that under weak wind conditions, V_{d,τ_R} agrees well with the deposition velocity from WRF-LES/D under neutral conditions. However, V_{d,τ_R} underestimates the deposition velocity under convective conditions, especially for particles that are not primarily influenced by molecular diffusion and gravity. In addition, this underestimation becomes more pronounced with increasing ABL instability.

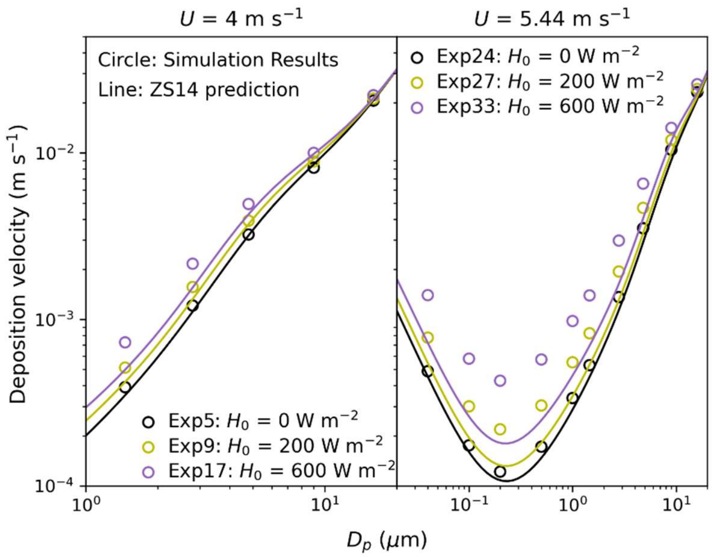

Figure 4-10: Comparison of the predicted result by the ZS14 scheme (lines) with the simulated value (circles) of Exp (5, 9, 17) (left) and Exp (24, 27, 33) (right).

To enhance the prediction of dust deposition velocity under convective conditions, this thesis takes into account the impact of shear stress fluctuations. Specifically, these fluctuations are integrated through the utilization of instantaneous shear stress distributions, thereby enabling an enhancement of the dry deposition scheme (hereafter referred to as the Y22 scheme) according to the following expression:

$$V_{d,\tau_f} = \int_0^\infty V_d(\tau_f)\, p(\tau_f)\, d\tau_f \tag{4.15}$$

where $p(\tau_f)$ is given by Equations (4.11)-(4.14), $V_d\left(\tau_f\right)$ is the instantaneous dust deposition velocity determined using the ZS14 scheme and τ_f.

Figure 4-11 graphically presents the outcomes of the improved scheme, demonstrating an impressive concurrence between the improved scheme's outcome V_{d,τ_f}, and simulated value $V_{d,LES}$. When compared to Figure 4-10, it becomes evident that with the inclusion of the shear stress distribution, the deposition scheme exhibits substantially enhanced alignment with the results of the numerical experiments.

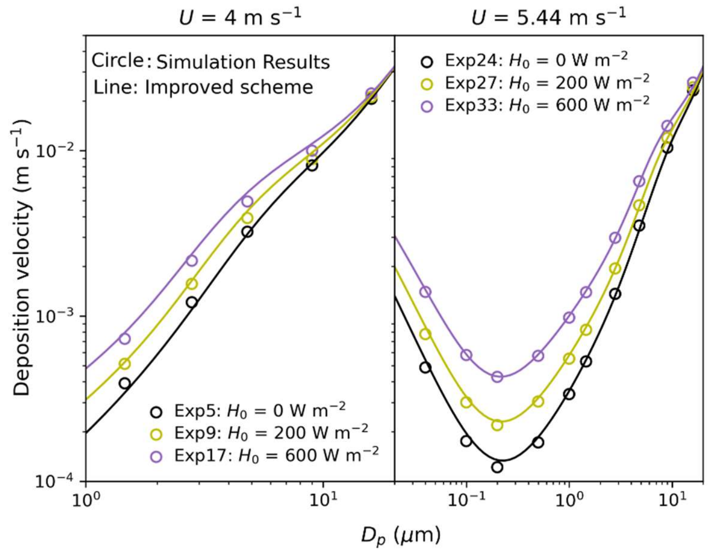

Figure 4-11: The comparison of the predicted result by the improved scheme (lines) with the simulated value (circles) of Exp (5, 9, 17) (left) and Exp (24, 27, 33) (right).

Up to now, three different mean deposition velocities have been described: V_{d,τ_R} , V_{d,τ_f} , and $V_{d,LES}$. $V_{d,LES}$ is serving as a reference for quantifying the other two velocities. To make the comparison more transparent, we also introduce the concept of the relative difference between V_{d,τ_f} and $V_{d,LES}$. Similar to Equation (4.10), the relative difference (*RE*) in the predicted deposition velocity by the improved scheme is expressed as

$$RE\left(V_{d,LES}, V_{d,\tau_f}\right) = \left|\frac{V_{d,LES} - V_{d,\tau_f}}{V_{d,LES}}\right| \times 100\% \tag{4.16}$$

Figure 4-12 shows that $RE\left(V_{d,LES}, V_{d,\tau_R}\right)$ generally increases with the shear stress turbulence intensity (TI-S). Meanwhile, the relative difference $RE\left(V_{d,LES}, V_{d,\tau_R}\right)$ obtained by using the Y22 scheme maintains a relatively stable range of values. Furthermore, when the shear stress intensity exceeds 0.4, the differences between $RE\left(V_{d,LES}, V_{d,\tau_R}\right)$ and $RE\left(V_{d,LES}, V_{d,\tau_f}\right)$ are evident for particles sized at 1.46 µm, 0.04 µm, and 0.5 µm. However, this contrast remains negligible for particles of 16 µm as their gravitational settling dominates the deposition.

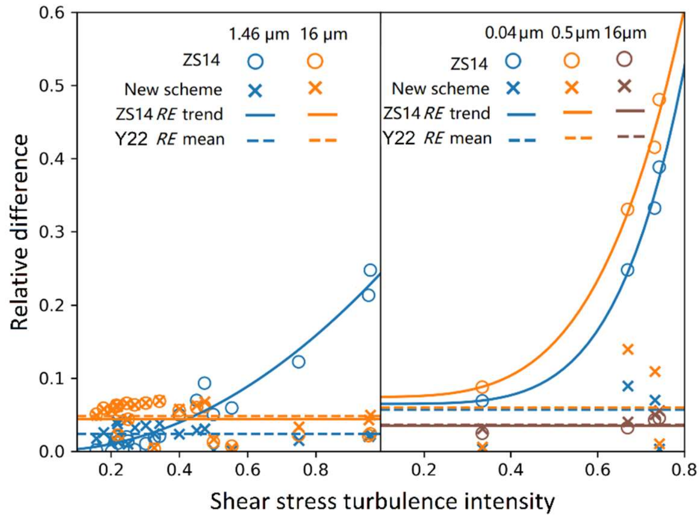

Figure 4-12: Comparison of relative difference as a function of shear stress turbulence intensity (TI-S), estimated by ZS14 scheme (circles) and the improved Y22 scheme (crosses) for Exp (1-20) (Left) and Exp (24, 27, 30, 33) (right).

Furthermore, to investigate which particle size range is strongly affected by the TI-S, the comparisons of the $RE\left(V_{d,LES}, V_{d,\tau_R}\right)$ and $RE\left(V_{d,LES}, V_{d,\tau_f}\right)$ are given here for all sizes of dust particles, as shown in Figure 4-13. The results show that $RE\left(V_{d,LES}, V_{d,\tau_R}\right)$ first increases and then decreases with increasing particle size. Notably, particles within the size range of 0.04 to 5 are strongly affected by turbulent shear stress. This size range covers the accumulation mode, approximately ranging from 0.1 to 2 µm. After incorporating the $p(\tau_f)$ consideration, errors are confined to around or less than 10%. As an illustration, the relative difference of Exp 17 (i.e., U = 4 m s^{-1} and $H_0 = 600$ W m^{-2}) for particles of 1.46 µm is reduced from approximately 25% to roughly 3%. Similarly, the relative difference of Exp 33 (i.e., U = 5.44 m s^{-1} and $H_0 = 600$ W m^{-2}) for particles of 0.5 µm is diminished from about 50% to around 12%.

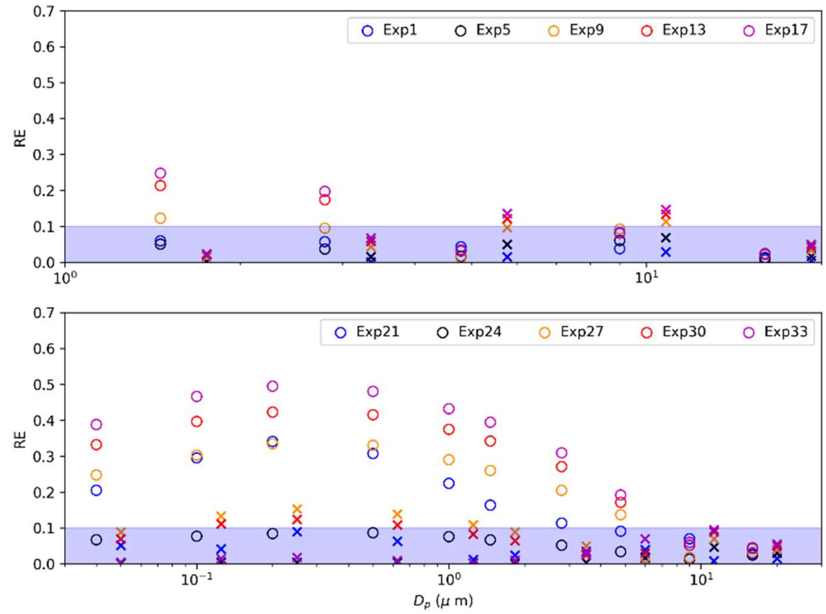

Figure 4-13: The variations of the RE including the $RE\left(V_{d,LES}, V_{d,\tau_R}\right)$ (circles) and the $RE\left(V_{d,LES}, V_{d,\tau_f}\right)$ (crosses) with the sizes of the dust particles.

To further analyze whether the $RE\left(V_{d,LES}, V_{d,\tau_R}\right)$ under the unstable condition is dominated by kinetic instability or dynamic instability, the gradient Richardson number in Equation (2.4) can be calculated as follows:

$$\mathrm{Ri} = -\frac{g}{\overline{\theta}} \kappa z \frac{\phi_h}{\phi_m^{\ 2}} \frac{H_0}{\rho_a c_p u_{*R}^{\ 3}} \tag{4.17}$$

Here, the center height of the lowest layer, $z = 0.5$ m, is applied.

Figure 4-14 shows the $RE\left(V_{d,LES}, V_{d,\tau_R}\right)$ increases as the Richardson number Ri decreases within the range $\mathrm{Ri} < -0.04$. According to the critical values for stability classification provided in Table 2-1, larger $RE\left(V_{d,LES}, V_{d,\tau_R}\right)$ coincides with convective predominance, weak winds, and strong vertical motion. This analysis reveals a positive correlation between TI-S and the gradient Richardson number Ri. While Ri and TI-S display an approximately linear relationship, the detailed nature of this connection requires further investigation.

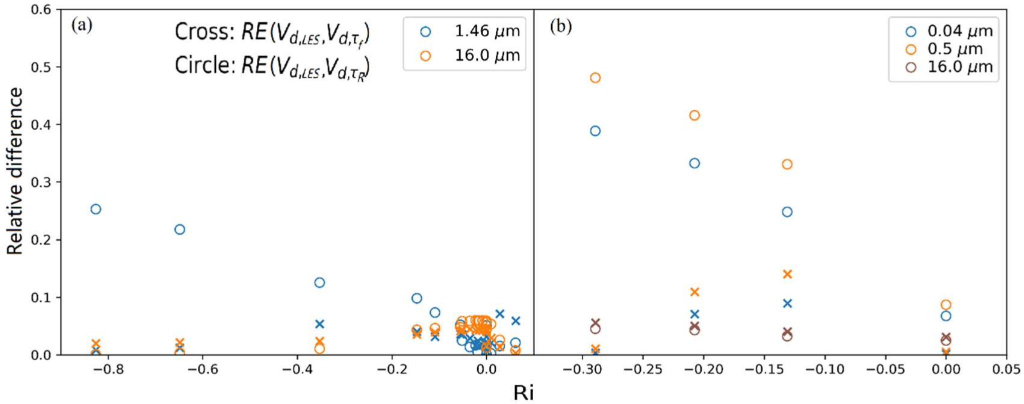

Figure 4-14: Comparison of the relative difference $RE\left(V_{d,LES},V_{d,\tau_R}\right)$ (circles) and $RE\left(V_{d,LES},V_{d,\tau_f}\right)$ (crosses) as functions of the Richardson number Ri from (a) Exp (1-20) and (b) Exp (24, 27, 30, 33).

Consequently, achieving precise dust deposition estimation demands a comprehensive depiction of the instantaneous shear stress field. In this regard, the Weibull distribution is employed to approximate the surface shear stresses. Through the incorporation of the shear stress distribution, we propose an enhanced version of the ZS14 scheme, designated as the Y22 scheme.

4.2.4 Shear stress at different heights

In Section 4.2.3, the scheme of ZS14 is improved by considering the shear stress at the surface. In WRF-LES/D, given the absence of wind velocity at the surface, the instantaneous shear stress aligns with the SGS shear stress due to the assumption that the contribution of grid-resolved shear stress is negligible. As described in Section 3.4, the SGS shear stress in the bottom layer is parameterized according to the MOST. However, the applicability of MOST in WRF-LES/D is still being questioned (Shao et al., 2013). In addition, the dust deposition velocity in field experiments is normally measured at an altitude above the surface. Therefore, this section examines how the shear stress distribution pattern varies with height. The grid-resolved shear stresses above the surface (in the air) are usually not zero and contribute to the instantaneous shear stress. Therefore, the magnitude of instantaneous shear stress is calculated from Equation (3.49), and the Reynolds shear stress is calculated from Equation (3.56).

To investigate the variation of shear stress distribution with height, an additional set of five numerical experiments, denoted as Exp (A1-A5), was conducted, as outlined in Table 4-1. These experiments involve a finer vertical grid division, with the horizontal grid size set at 10 m. In the vertical dimension, the height of the bottom layer is 1m, and the grid size ranges from 1 m to 51 m, increasing in 2 m increments. Notably, these experiments were carried out without the inclusion of the dust module coupling. This section presents simulation data from both Exp (21-35) and Exp (A1-A5) at various heights, specifically 0.5 m, 2 m, 5 m, 10 m, 20 m and 50m. These heights are conventionally chosen to measure the meteorological elements.

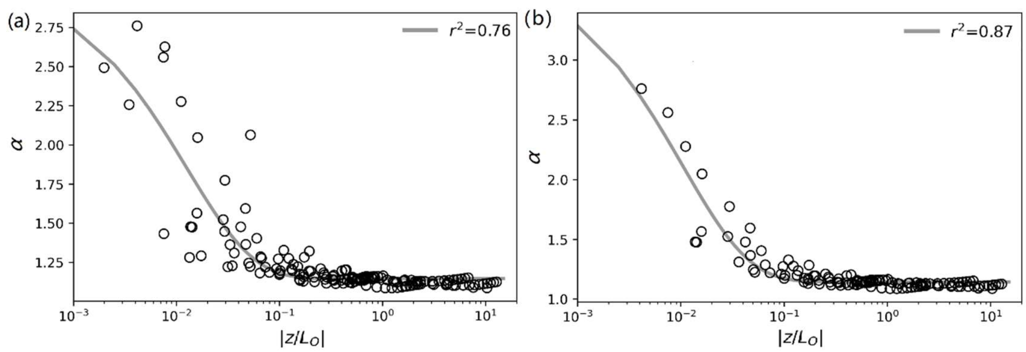

Figure 4-15: (a) Dependency of shape parameter α on z/Lo for friction velocity distribution from Exp (21-35) and Exp (A1-A5), (b) same as (a), but without the scenarios of neutral and stable conditions.

Figure 4-15a shows the shape parameters for all selected heights in Exp (21-35) and Exp (A1-A5). Meanwhile, Figure 4-15b mirrors Figure 4-15a but excludes simulations under neutral and stable conditions. These shape parameters exhibit an exponential decrease with $|z / L_O|$. The values of the shape parameters shown in Figure 4-15a are more widely spread in the region with small $|z / L_O|$. The expression for the shape parameters in Figure 4-15a can be represented as:

$$\alpha = 1.92 \cdot \exp\left(-18.45 \cdot |z / L_O|^{-2/3}\right) + 1.45 \tag{4.18}$$

In Figure 4-15b, the expression for the shape parameters is $\alpha = 1.93 \cdot \exp\left(-18.81 \cdot |z / L_O|^{2/3}\right) + 1.16$. Moving on, at each elevation, the scale parameter β demonstrates a linear dependence on a composite function that combines both the Reynolds shear stress and the bulk vertical scaling velocity, $u_*^2 + z / z_l w_*^2$, as graphically depicted in Figure 4-16. This linear relationship is mathematically characterized by Equation (4-19):

$$\beta = K_\beta \cdot \left(u_*^2 + z / z_l \cdot w_*^2 \right) \tag{4.19}$$

where K_β represents the slope. Moreover, Figure 4-16 also illustrates that these slopes exhibit an ascending trend with the simulated height of the grid level. Table 4-4 provides a summary of the specific values of K_β at each height, and the values are visually presented in Figure 4-17. Notably, the slope K_β experiences a logarithmic increase in correspondence with the simulated height. The logarithmic relationship between slopes and heights is expressed as follows:

$$K_\beta = 0.568 \cdot \ln\left(\frac{z}{0.131} \right) \tag{4.20}$$

Table 4-4: The relationship between β and height z.

z	0.5	2	5	10	20
K_β	1.122	1.492	1.999	2.492	2.853

However, a noticeable discrepancy arises between the shape and scale parameters presented here and the coefficients utilized in formulating surface shear stress expressions. A plausible explanation for this disparity lies in the intricate challenge of precisely pinpointing the z value within Equation (4.18) and Equation (4.19) at the surface level. In order to fully comprehend the underlying causes of this variation, a more comprehensive investigation is warranted.

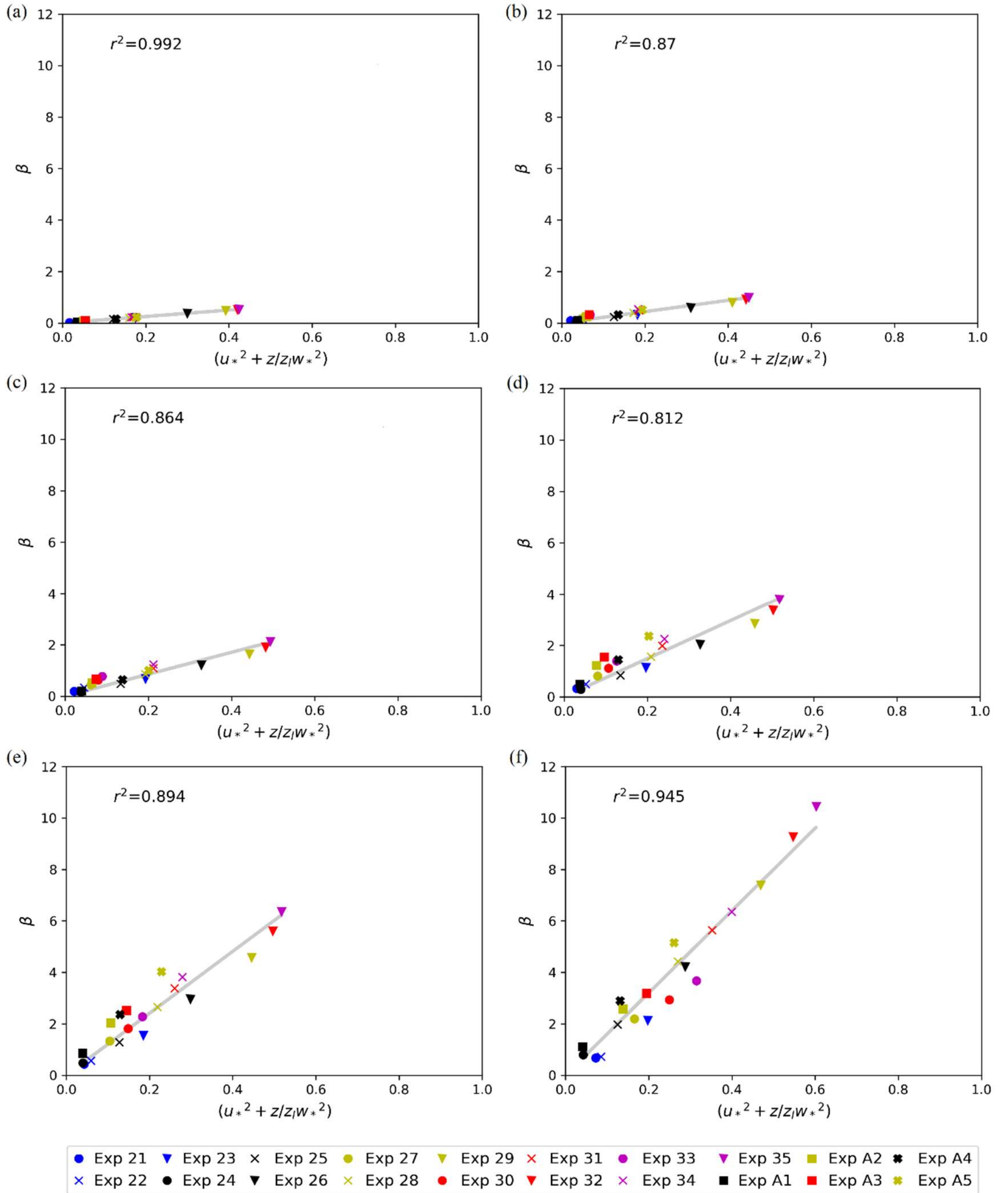

Figure 4-16: The dependence of the scale parameter β on u_* and w_* at different heights: (a) z = 0.5 m, (b) z = 2 m, (c) z = 5 m, (d) z = 10 m, (e) z = 20 m, and (f) z = 50 m for Exp (21-35) and Exp (A1-A5).

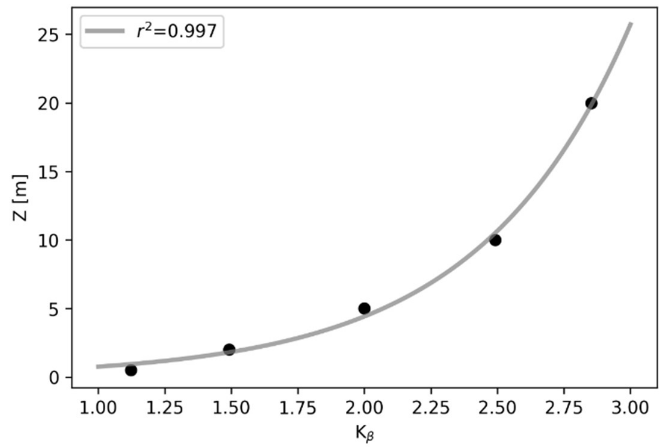

Figure 4-17: The variation of K_β with z.

4.2.5 Shear stress over a grass surface

The previous sections focus on analyzing the shear stress and the deposition velocity over the sand surface. This section introduces a series of conducted WRF-LES/D experiments over grass surfaces, where the roughness length z_0 is set at 10 cm. The aim is to investigate whether the distribution of shear stress above the grass field also conforms to the Weibull distribution and to assess how the shape and scaling parameters may vary.

The experimental setup mirrors that of Section 4.1, with the exception that parameters tailored to the grass surface in the ZS14 scheme are used. Similarly, the analysis procedure replicates that of Section 4.2, with the distinction that the calculation of shear stress takes into account the grid-resolve shear stress. As listed in Table 4-5, a total of 12 numerical experiments are conducted, with the atmospheric stability ranging from 0 to 600 W m^{-2} and background wind set at 3.6, 7.2, and 11.9 m s^{-1}.

Table 4-5: List of numerical experiments over grass surface with z_0 = 10 cm.

NAME	H_0	U	τ_R	σ_τ	σ_τ / τ_R	γ_1	α	β	$1/L_o$
Exp36	0	3.6	0.0426	0.0346	0.812	2.834	2.116	0.045	0.03
Exp37	0	7.2	0.1302	0.0558	0.428	0.764	2.593	0.146	0.006
Exp38	0	11.9	0.3406	0.153	0.449	0.682	2.398	0.38	0.001
Exp39	200	3.6	0.0778	0.0685	0.879	1.528	1.603	0.104	0.095
Exp40	200	7.2	0.2181	0.1236	0.567	1.259	2.188	0.247	0.02
Exp41	200	11.9	0.4416	0.1934	0.438	0.756	2.598	0.494	0.007
Exp42	400	3.6	0.0817	0.0853	1.044	1.452	1.458	0.122	0.177
Exp43	400	7.2	0.2322	0.1367	0.587	1.11	2.066	0.271	0.036
Exp44	400	11.9	0.5068	0.2249	0.443	0.725	2.586	0.574	0.011
Exp45	600	3.6	0.0981	0.1041	1.06	1.462	1.566	0.159	0.177
Exp46	600	7.2	0.2386	0.1661	0.695	1.186	1.735	0.286	0.053
Exp47	600	11.9	0.5178	0.2593	0.501	0.881	2.291	0.585	0.016

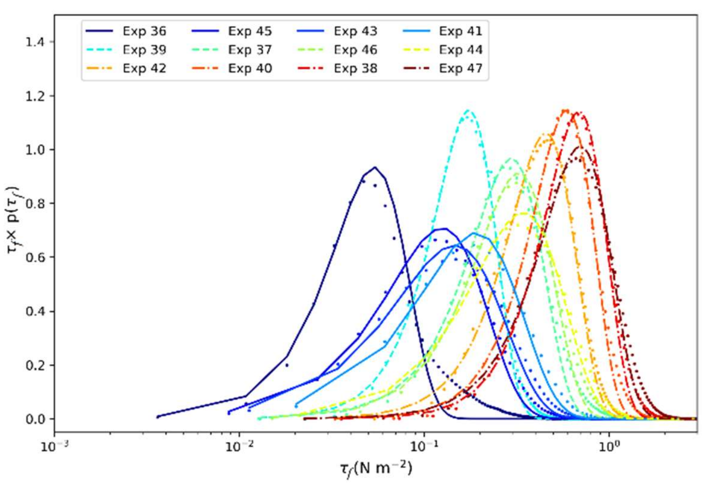

Figure 4-18: The probability density functions of shear stress from LES (dots) with the fitting lines (lines) for Exp (36-47).

Figure 4-18 shows the probability density distribution of instantaneous shear stress. Analogous to earlier described numerical experiments, the probability density distribution of obtained shear stress can be well-fitted to a Weibull distribution function. As observed with the shear stress pattern of the sand surface, the shape parameter exhibits a decrease with the inverse of Obukhov length L_o, as shown in Figure 4-19a. Additionally, the scale parameter is linearly related with $u_*^2 + 0.001w_*^2$, as shown in Figure 4-19b. Equation (4.21) and Equation (4.22) elucidate the detailed dependencies of α and β on the macro-meteorological parameters.

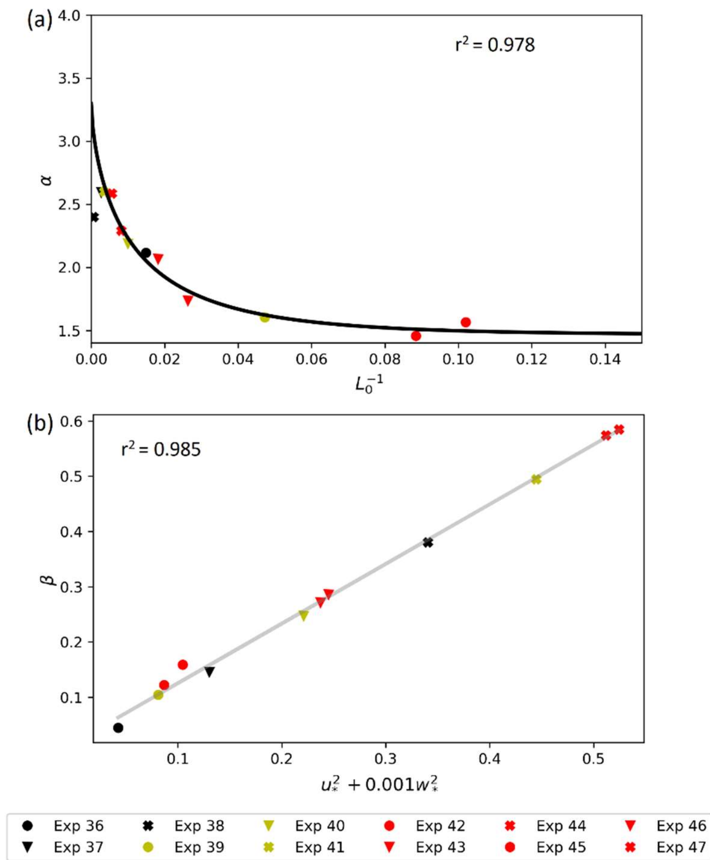

Figure 4-19: For numerical experiments of EXP (36-47): (a) Dependency of the shape parameter α on L_O^{-1}; (b) Dependency of scaling parameter β on $\left(u_{*R}^{\ 2} + 0.001w_*^{\ 2}\right)$.

$$\alpha = 1.83 \cdot \exp\left(-11.84 \cdot L_O^{-2/3}\right) + 1.46 \tag{4.21}$$

$$\beta = 1.278 \cdot \left(u_*^2 + 0.001w_*^{\ 2}\right) \tag{4.22}$$

The Reynolds shear stress τ_R, standard deviation σ_τ, turbulence intensity σ_τ / τ_R, and the skewness γ_1 of the instantaneous shear stress, along with the scaling parameter β and shape parameter α for the fitted Weibull distribution function, are also presented in Table 4-5. It is evident that both σ_τ and τ_R increase with increasing instability and background wind speed. This suggests that under unstable conditions, turbulence tends to be more intense and the Reynolds friction velocity is higher. However, the ratio between σ_τ and

τ_R , i.e., TI-S, displays a declining trend with rising background wind speed, while conversely, it demonstrates an upsurge in the presence of atmospheric instability.

4.3 Conclusions

This chapter aims to investigate dust deposition within a fully developed turbulent atmosphere. To achieve this, a series of numerical experiments were conducted utilizing WRF-LES/D, involving varying background wind speeds and the ABL stabilities. The analysis encompasses shear stress assessment at both the surface and different heights. The outcomes of this investigation reveal that estimating dust deposition velocity solely through Reynolds shear stress yields an underestimation of dust deposition within the ABL under conditions of weak winds and pronounced convection. Notably, the instantaneous shear stress can be effectively approximated by a Weibull distribution. The shape parameter of this distribution demonstrates an exponential decline in correlation with the reciprocal of the absolute value of the Obukhov length. Meanwhile, the scale parameter displays a linear increase correlated with a composite function involving Reynolds shear stress and bulk vertical scaling velocity. These patterns apply consistently to shear stress distributions at various altitudes.

By incorporating this Weibull distribution into the dust deposition scheme, an advanced and refined dust deposition scheme has been formulated.

5. Application of dust deposition schemes in WRF-Chem

In this chapter, we integrate both the ZS14 scheme and the improved scheme as introduced in Chapter 4 – the Y22 scheme (Yin et al., 2022), into the Weather Research and Forecasting model coupled with Chemistry (WRF-Chem) Version 4.0. Subsequently, these coupled models are employed to conduct regional-scale simulations of dust deposition.

5.1 Model description

WRF-Chem serves as the foundational model for integrating, applying, and validating the ZS14 scheme and Y22 scheme on a regional scale. WRF-Chem, known for its effectively simultaneous simulation of trace gas and aerosol emissions, transport, mixing, and chemical transformations alongside meteorological characteristics (Grell et al., 2005), is frequently employed for the investigation of mesoscale and synoptic air quantity issues.

WRF-Chem requires several physical processes. Specifically, the Yonsei University scheme (Hong et al., 2006) is selected as the closure scheme for the planetary boundary layer, while the Revised MM5 scheme for Monin-Obukhov similarity governs surface layer closure (as outlined in Section 3.3). In addition, the Noah land-surface model, utilizing the global soil categorization dataset from the United States Geological Survey (USGS) featuring 24 land categories. The Rapid Radiative Transfer Model for General Circulation (RRTMG) radiation scheme (Iacono et al., 2008) is applied to calculate the longwave and shortwave radiations. For convective and microphysics considerations, the Grell-Freitas convective scheme (Grell and Freitas, 2014) and the Morrison two-moment microphysics scheme (Morrison et al., 2009) are used. The aerosol module employed is the model for dust only (hereafter referred to as the DUST model). The DUST model classifies airborne dust particles into five bins: 0.92-2, 2-3.6, 3.6-6, 6-12, 12-20 μm, each with respective effective diameters of 1.46, 2.8, 4.8, 9, 16 μm. The dust emission scheme Shao2011 (Shao et al., 2011b) is used here to calculate surface dust emission and is elaborated upon further below. A compilation of the physical and chemical schemes configuring the model is presented in Table 5-1.

Table 5-1: WRF-Chem configuration in this study.

Atmospheric process	WRF-Chem option	Namelist variable	Option
Planetary boundary layer	Yonsei University scheme	bl_pbl_physics	1
Surface layer	Revised MM5 similarity	sf_sfclay_physics	1
Land surface	Noah land-surface model	sf_surface_physics	2
Microphysics	Morrison double moment	mp_physics	10
Cumulus clouds	Grell-Freitas	cu_physics	3
Longwave radiation	RRTMG	ra_lw_physics	4
Shortwave radiation	RRTMG	ra_sw_physics	4
Aerosol chemistry	Dust concentration only	chem_opt	401
Dust emission	Shao2011	Dust_schme	3

5.1.1 Shao2011 scheme

The Shao2011 scheme is a physics-based methodology employed to estimate size-resolved dust emissions. This scheme takes into account the saltation of grains with size d, and it calculates the emission rate of dust particles with size $D_{p,i}$ (from the i-th bin) using the following equation:

$$F(D_{p,i}) = c_y \eta_{mi} (1 + \sigma_m) \frac{gQ}{u_*^2} \tag{5.1}$$

where c_y is the dimensionless coefficient, η_{mi} is the fraction of dust that is capable of being emitted, σ_m is the bombardment efficiency, and Q stands for the saltation flux averaged over the range of sand particle sizes. The values of Q can be obtained using the equation:

$$Q = \int_{d_1}^{d_2} Q(d)\, p_m(d)\, \delta d \tag{5.2}$$

where d_1 and d_2 are the upper and lower limits of the saltation particle size, respectively, $p_m(d)$ is the minimally disturbed particle-size distribution. $Q(d)$ is the saltation flux for saltation particle size d and is calculated as

$$Q(d) = (1 - c_f) c_0 \frac{\rho_a}{g} u_*^3 \left(1 - \frac{u_{*t}}{u_*}\right)\left(1 + \frac{u_{*t}}{u_*}\right)^2 \tag{5.3}$$

where u_{*_t} is the threshold friction velocity, c_f is the fraction of vegetation cover, and c_0 is the Kawamura coefficient which falls between 1.8 and 3.1 (Kawamura, 1964).

Before conducting numerical experiments, it is important to determine the size bins for the dust particles under study. In the Shao2011 scheme, the emitted dust particles in the size range of 0.98 μm to 20 μm are divided into 40 size bins, which are further grouped into 5 size bins: 0.92-2, 2-3.6, 3.6-6, 6-12, 12-20 μm.

5.1.2 Numerical experiment setup

The simulation domain covers a geographic region spanning central northern China and southern Mongolia (93.69 – 117.82˚E, 33.76 – 47.46 ˚N). The utilized global categorization data from the United States Geological Survey (USGS) comprises 12 soil types and 24 land-use types, as shown in Figure 5-1. The simulation period ranges from March 28, 2001, to October 30, 2001, aligning with the availability of in-situ observations. Meteorological conditions are initialized and updated using the NCEP CFSR product (National Center for Environmental Prediction, Climate Forecast System Reanalysis) with a spatial resolution of 0.3˚.

In this study, a horizontal resolution of 10 km × 10 km is specified, with a vertical division into 38 layers with a model top pressure of 50 hPa. The longitudinal and latitudinal grid count amounts to 180 and 120, respectively. The simulation time step is 60 seconds, and the frequency of output results is once per hour. Simulations prior to April 1st serve the purpose of model spin-up and are excluded from the subsequent analysis.

The computation of dust deposition employs separate modules for the ZS14 scheme and the Y22 scheme, facilitating a comparative assessment between them. A consolidated overview of the simulation configurations is presented in Table 5-2.

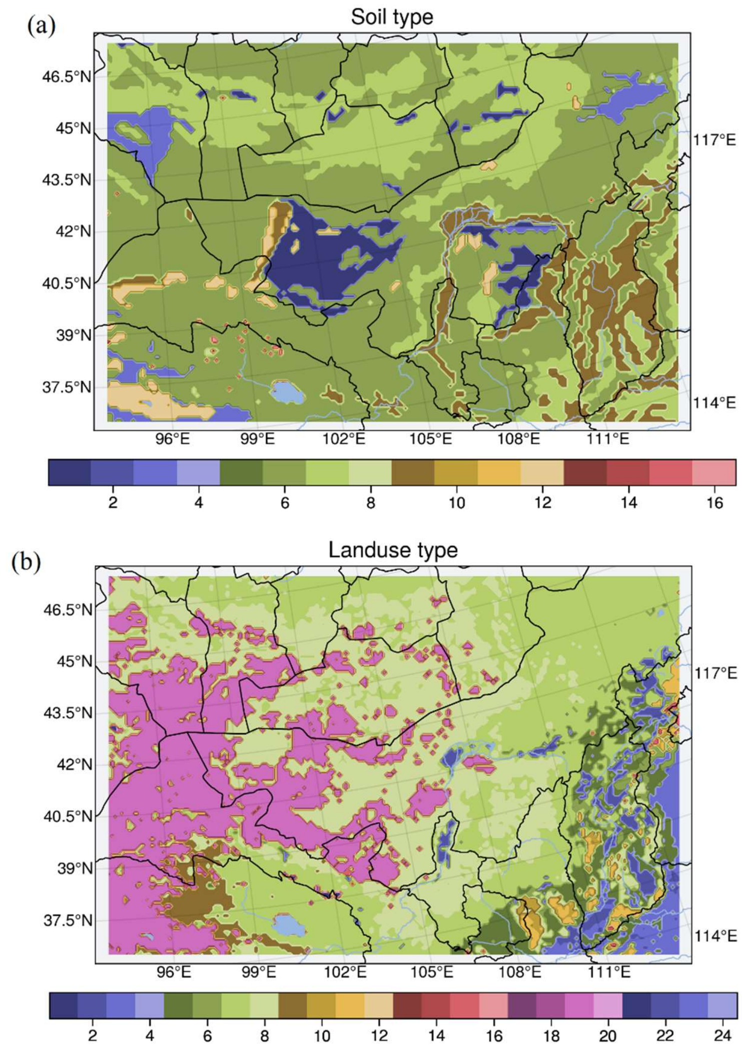

Figure 5-1: (a) WRF-Chem-generated soil categorization based on USGS. 1. Sand; 2. Loamy sand; 3. Sandy loam; 4. Silt loam; 5. Silt; 6. Loam; 7. Sandy clay loam; 8. Silty clay loam; 9. Clay loam; 10. Sandy clay; 11. Silty clay; 12. Clay; 13. Organic material; 14. Water; 15. Bedrock; 16. Land ice. (b) Land use categorization based on USGS. 1. Urban and Built-Up Land 2. Dryland Cropland and Pasture; 3. Irrigated Cropland and Pasture; 4. Mixed Dryland/Irrigated Cropland and Pasture; 5. Cropland/Grassland Mosaic; 6. Cropland/Woodland Mosaic; 7. Grassland; 8. Shrubland; 9. Mixed Shrubland/Grassland; 10. Savanna; 11. Deciduous Broadleaf Forest; 12. Deciduous Needleleaf Forest; 13. Evergreen Broadleaf Forest; 14. Evergreen Needleleaf Forest; 15. Mixed Forest; 16. Water Bodies; 17. Herbaceous Wetland; 18. Wooded Wetland; 19. Barren or Sparsely Vegetated; 20. Herbaceous Tundra; 21. Wooded Tundra; 22. Mixed Tundra; 23. Bare Ground Tundra; 24. Snow or Ice.

Table 5-2: Settings of model simulation.

Characteristic	Option
Domain	WE: 93.69 – 117.82˚E, NS: 33.76 – 47.46 ˚N
Atmospheric forcing data	CFSR with a resolution of 0.3 ˚
Topography data	Geographic Static Data default in WRF
Grid resolution	10 km
Number of cells	180 × 120
Timestep	1 minute
History interval	1 hour
Simulation period	01/04/2001-30/10/2001

The deposition schemes of ZS14 and Y22 require specific parameters to accurately simulate their effects. These parameters encompass the roughness length (z_0), the height of the roughness elements (z_h), the characteristic diameter of the roughness elements (d_c), the coverage fraction ratio of roughness elements in the grid (η), and the frontal area index of the roughness elements in the grid (λ). These parameters exhibit variability based on distinct land-use types.

For the parameters z_0, h_c, η, and λ, the default values established within the WRF framework are employed, with an exception being z_0 on the desert surface. For these areas, the value recommended by Zhang and Shao (2014) is adopted. Parameters not explicitly defined within the WRF scheme are meticulously specified by referencing reputable sources. For instance, the value of d_c is informed by Zhang et al. (2001), while the A_{in} parameter aligns with Zhang and Shao (2014). The assortment of parameter values corresponding to diverse land-use categories can be found in Table 5-3. Notably, values attributed to η and λ for urban regions, water bodies, and ice surfaces, as displayed in the table, are drawn from Zhang et al. (2001), diverging from the values proposed by WRF.

Table 5-3: USGS 24-category Land Use Categories with the corresponding parameters.

Category	Description	z_0 (m)	h_c (m)	d_c (m)	A_{in}	η	λ
1	Urban and Built-up Land	0.8	0.00	0.01	1.	0.5	0.4
2	Dryland Cropland and Pasture	0.15	0.5	0.002	150	--	--
3	Irrigated Cropland and Pasture	0.1	0.5	0.002	150	--	--
4	Mixed Dryland/Irrigated Cropland and Pasture	0.15	0.5	0.002	150	--	--
5	Cropland/Grassland Mosaic	0.14	0.5	0.002	150	--	--
6	Cropland/Woodland Mosaic	0.2	0.5	0.01	150	--	--
7	Grassland	0.12	0.5	0.002	150	--	--
8	Shrubland	0.05	0.5	0.002	150	--	--
9	Mixed Shrubland/Grassland	0.06	0.5	0.002	150	--	--
10	Savanna	0.15	0.5	0.002	150	--	---
11	Deciduous Broadleaf Forest	0.5	20.0	0.005	150	--	--
12	Deciduous Needleleaf Forest	0.5	14.0	0.002	150	--	--
13	Evergreen Broadleaf	0.5	35.0	0.005	150	--	--
14	Evergreen Needleleaf	0.5	17.0	0.002	150	--	--
15	Mixed Forest	0.5	18.0	0.005	150	--	--
16	Water Bodies	0.0001	0.003	0.0001	100	0.018	0.538
17	Herbaceous Wetland	0.2	0.5	0.01	100	--	--
18	Wooden Wetland	0.4	20.0	0.01	150	--	--
19	Barren or Sparsely Vegetated	0.01	0.0001	0.0002	1	0.25	0.125
20	Herbaceous Tundra	0.1	0.5	9.999	1	--	--
21	Wooded Tundra	0.3	10.0	0.01	150	--	--
22	Mixed Tundra	0.15	5.0	9.999	1	--	--
23	Bare Ground Tundra	0.1	0.02	0.0006	1	--	--
24	Snow or Ice	0.001	0.0	0.0	1	0	0

5.2 Simulation results

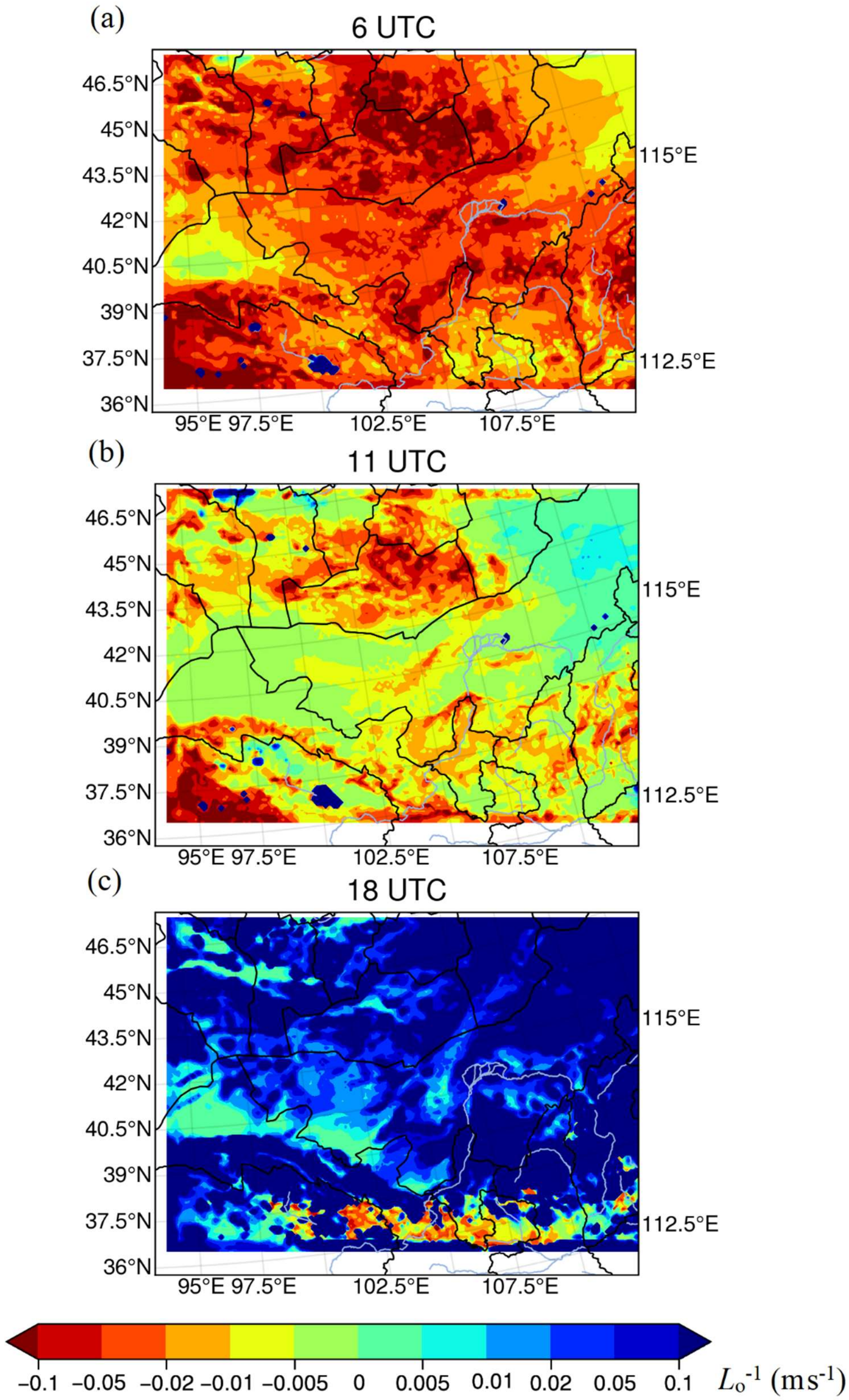

Figure 5-2: The spatial distribution values of L_o^{-1} at three different times: (a) 6 UTC (local time 12:00), (b) 11 UTC (local time 17:00), and (c) 18 UTC (local time 24:00) on April 21st, 2001.

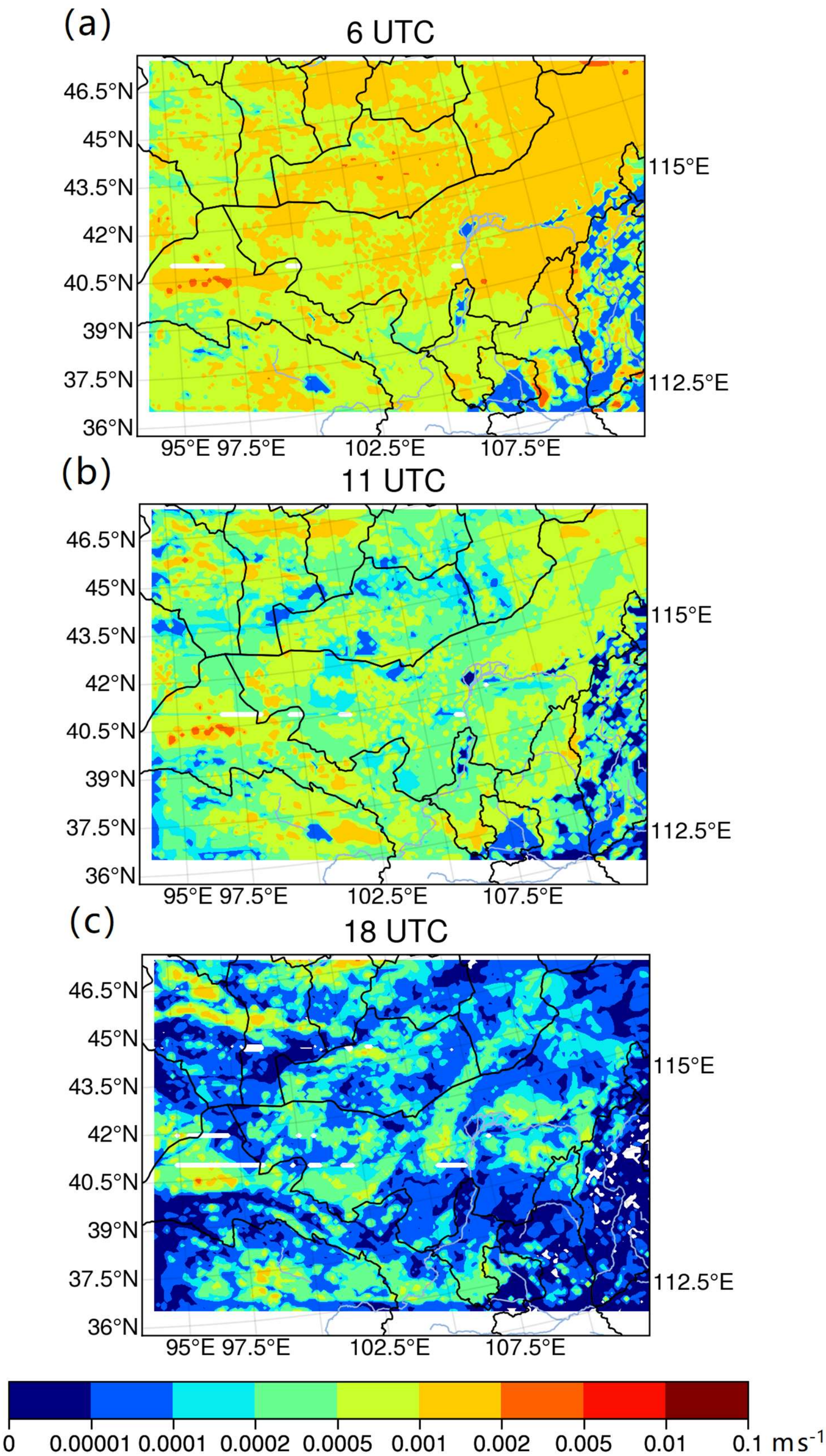

Figure 5-3: The spatial distribution of ΔV_d for particles of 1.46 μm at three times: (a) 6 UTC (local time 12:00), (b) 11 UTC (local time 17:00), and (c) 18 UTC (local time 24:00) on April 21st, 2001.

Let $V_{d,ZS14}$ represents the dust deposition velocity calculated by the ZS14 scheme utilizing Reynolds shear stress in the WRF simulation. Conversely, $V_{d,Y22}$ denotes the dust deposition velocity calculated by the Y22 scheme, which incorporates the distribution of surface shear stress. The difference between $V_{d,ZS14}$ and $V_{d,Y22}$ is computed according to the following equation:

$$\Delta V_d = V_{d,Y22} - V_{d,ZS14} \tag{5.4}$$

In Figure 5-2, the spatial distribution of L_O^{-1} within the surface layer is depicted at three Coordinated Universal Times (UTC): 6 UTC, 11 UTC, and 18 UTC. These correspond to local times of 12:00, 17:00, and 24:00 on May 21st. The figure shows that the ABL stability varies within the domain corresponding to these three times. In particular, almost the entire domain corresponds to a convective ABL at 6 UTC, while a stable ABL state prevails at 18 UTC. At 11 UTC, a substantial portion of the area experiences a neutral ABL state.

We then compared the differences in deposition velocities corresponding to these three times, as shown in Figure 5-3. It can be observed that ΔV_d at 6 UTC is generally larger compared to the other two moments. ΔV_d at 18 UTC is very small, while ΔV_d at 11 am UTC falls in between. When comparing Figure 5-2 to Figure 5-3, it becomes evident that the value of ΔV_d under unstable conditions is larger than the value under neutral conditions, and the ΔV_d under stable conditions is small. This comparison suggests that as the ABL changes from an unstable to a stable regime, the influence of the parameterization of surface shear stress on the correction of dust deposition velocity decreases. In addition, Figure 5-3 also shows that ΔV_d is not horizontally homogeneous. Discrepancies in dust deposition velocity are not only related to atmospheric stability conditions but also exhibit a stronger association with land use categories.

When using the land cover types – desert, shrub, and water body – as examples, Figure 5-4 illustrates the daily variation of the dust deposition velocities $V_{d,ZS14}$ and $V_{d,Y22}$, along with their difference ΔV_d. To provide a clearer demonstration of the impact of atmospheric stability on these variables, Figure 5-4 also presents the daily variation of the reciprocal Obukhov length, L_o^{-1}. The data depicted in Figure 5-4 represents the average values obtained from the nine adjacent grids, with the land-use type being consistent across these nine grids. Figure 5-4 reveals that on desert and shrub surfaces, $V_{d,Y22}$ is higher than $V_{d,ZS14}$ from 3 UTC to 9 UTC – corresponding to local times of 9:00 to 15:00, respectively. During this time period, the ABL is under convective conditions, indicated by the negative L_O^{-1}. After 9 UTC, L_O^{-1} experiences an increase, whereas the value of ΔV_d undergoes a decline. As L_O^{-1} rises to 0 or greater values, ΔV_d approaches zero. However, the ABL over water surface remains consistently stable, leading to a marginal difference between $V_{d,ZS14}$ and $V_{d,Y22}$.

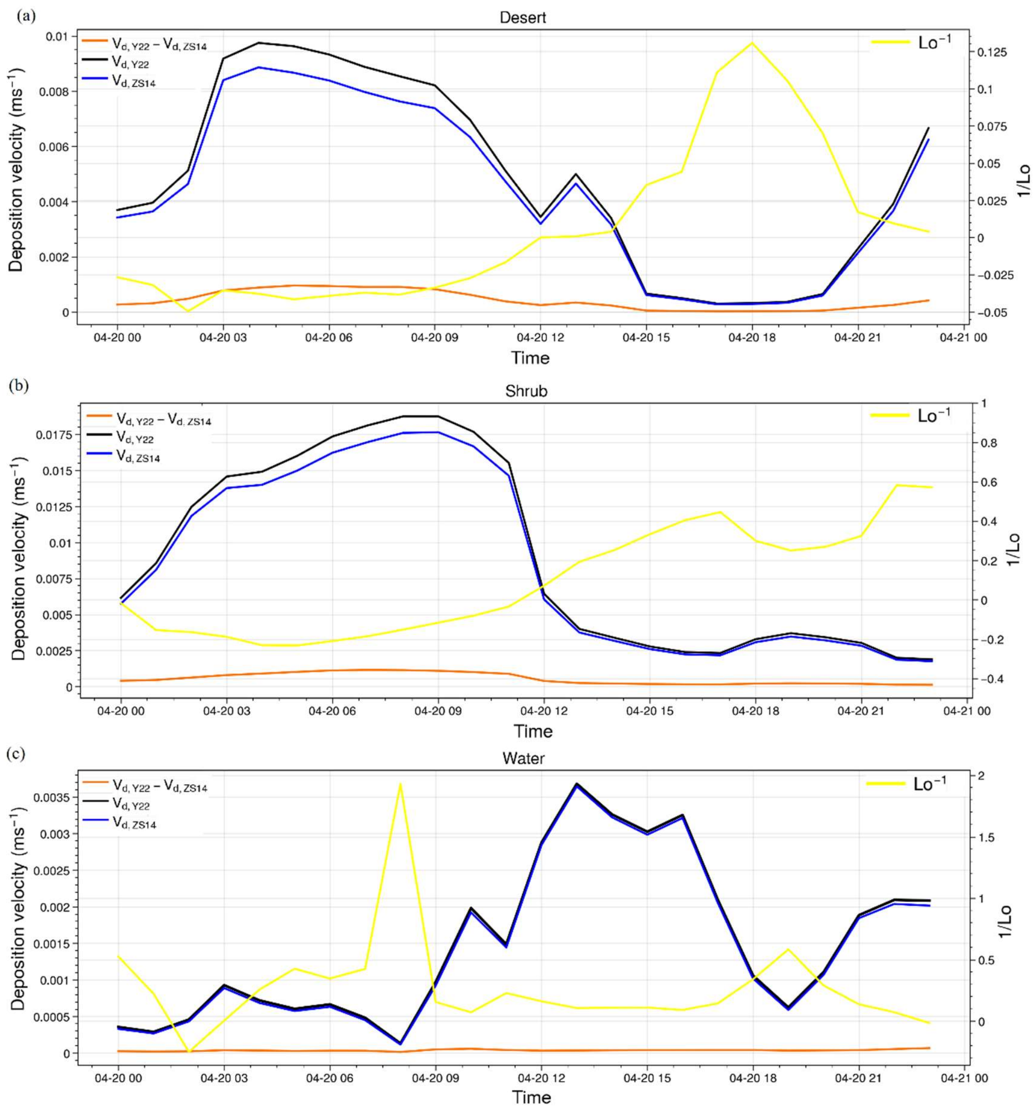

Figure 5-4: Daily variation of the dust deposition velocity (black line: $V_{d,Y22}$, blue line: $V_{d,ZS14}$, red line: ΔV_d) and the reciprocal of Obukhov length (L_O^{-1}, yellow line) obtained by averaging nine adjacent grids with the same land-use type.

In Figure 5-5, a comparison is made between monthly simulated dust deposition masses from the ZS14 and Y22 schemes and field observations conducted by the Chinese Academy of Sciences at the Shapotou Observatory (latitude: 37º16', longitude: 104º34') in China. In this experiment, dust particles falling within the size ranges of $D_p < 6\ \mu\text{m}$, $D_p < 12\ \mu\text{m}$ and $D_p < 20\ \mu\text{m}$ are measured. As shown in the figure, both ZS14 and Y22 schemes underestimate the dust particle deposition compared to the observed value.

Interestingly, the dust deposition masses simulated by the ZS14 scheme exhibit higher values than those yielded by the Y22 scheme – a counterintuitive outcome given our expectations. Ideally, we anticipated the Y22 scheme to predict greater dust deposition fluxes compared to the ZS14 scheme due to $V_{d,Y22} > V_{d,ZS14}$. As dust deposition flux hinges on both dust deposition velocity and dust concentration, we compared the monthly mean dust concentrations generated by using the ZS14 and Y22 schemes, as shown in Figure 5-6. As evident, the monthly mean dust concentrations simulated with the two schemes are different. The ZS14 scheme yields larger dust concentrations compared to the Y22 scheme.

Given the consistent meteorological variables such as wind speed and temperature across simulation scenarios, along with uniform dust emissions calculated via the Shao11 emission scheme, the Y22 scheme exhibits a larger deposition velocity. This greater deposition velocity results in the removal of a larger number of dust deposition particles, especially when dust concentrations are uniform for both schemes. Consequently, this removal leads to a reduction in airborne dust concentration as well as dust deposition particles. The reduction in dust concentration, in turn, leads to a further reduction in the dust flux. This explains why the simulated dust deposition flux using the Y22 scheme is lower than that obtained with the ZS14 scheme.

If c_{Y22} and c_{ZS14} represent the simulated dust concentrations using schemes of ZS14 and Y22 respectively, the disparity between them is computed as follows:

$$\Delta c = c_{ZS14} - c_{Y22} \tag{5.5}$$

Analogously, the dust deposition flux simulated by these two schemes is represented as $F_{d,ZS14}$ and $F_{d,Y22}$, with the difference being $\Delta F_d = F_{d,ZS14} - F_{d,Y22}$.

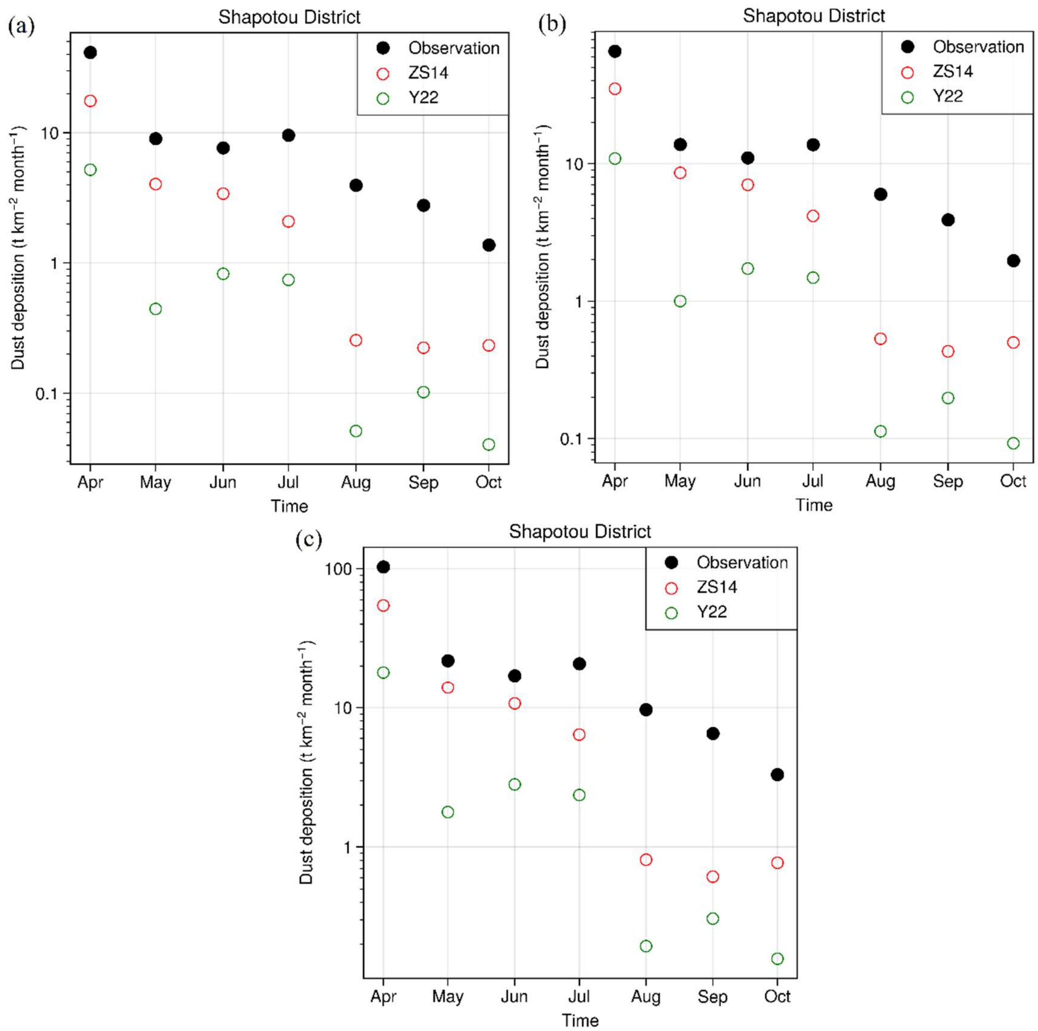

Figure 5-5: Comparisons of simulated monthly dust deposition by ZS14 and by Y22 at Shapotou district: (a) particles with $D_p < 6$ μm ; (b) particles with $D_p < 12$ μm ; (c) particles with $D_p < 20$ μm .

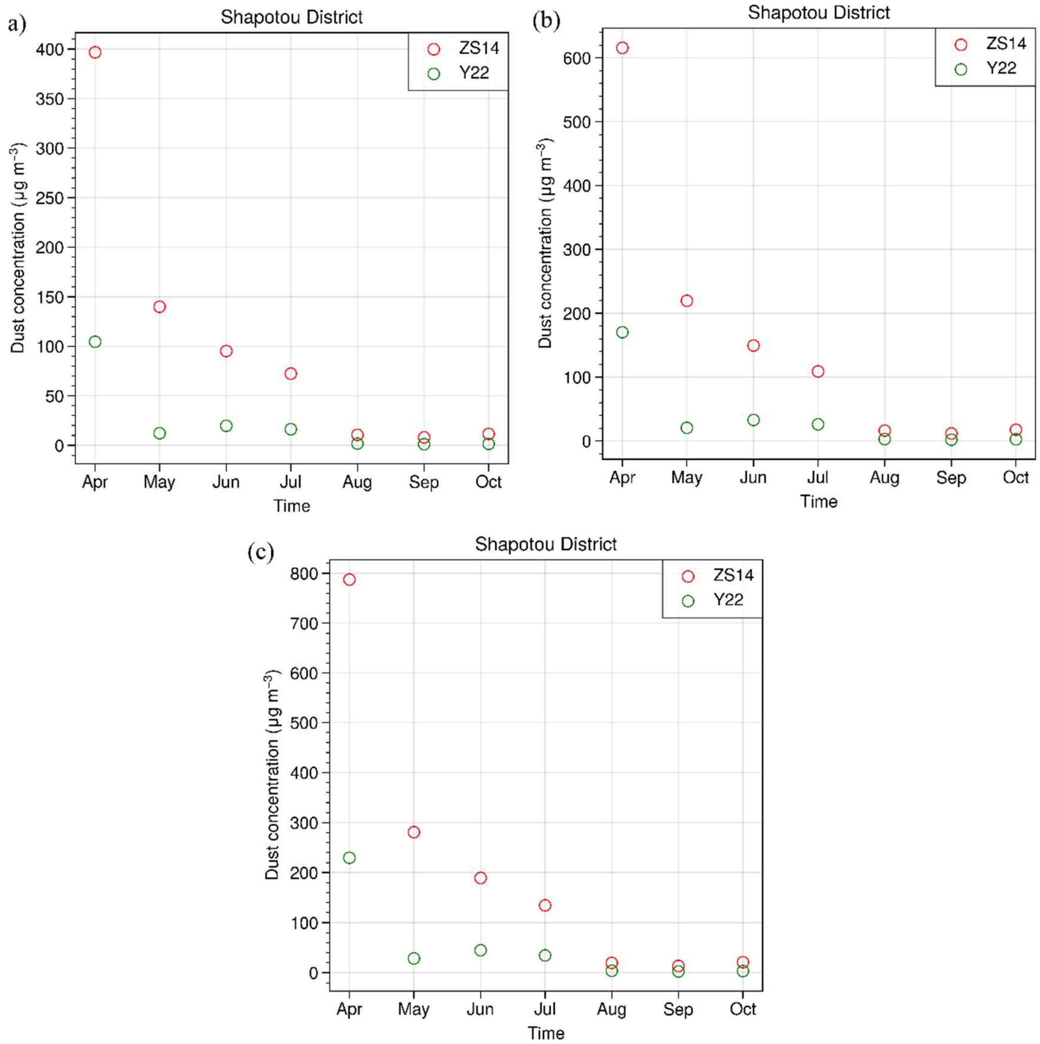

Figure 5-6: Comparisons of monthly dust concentration from the deposition scheme of ZS14 and Y22 for (a) particles with $D_p < 6$ μm ; (b) particles with $D_p < 12$ μm ; (c) particles with $D_p < 20$ μm .

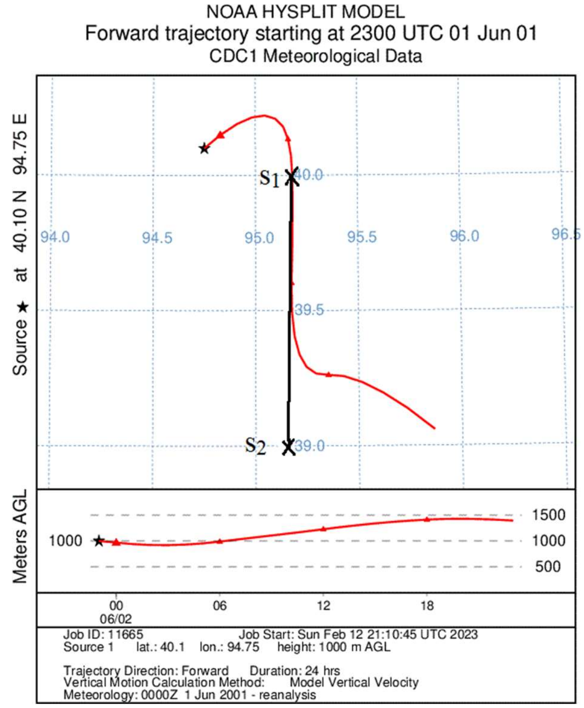

Figure 5-7: 24-hour forward trajectories of wind starting on 23 UTC June 01st, 2001, from an emission source area (black stars). The path (black line) between the start point S_1 and the endpoint S_2 is used for dust deposition analysis. NOAA = National Oceanic and Atmospheric Administration; HYSPLIT = Hybrid Single-Particle Lagrangian Integrated Trajectory; GDAS = Global Data Assimilation System; AGL = above ground level.

Figure 5-7 gives a 24-hour wind advance trajectory originating from an emission source (depicted as a star). Given the fine nature of dust particles that closely follow wind patterns, we assume that the trajectory showcased in Figure 5-7 also signifies the trajectory of dust particle transport. Along this wind trajectory, we designate two points – S_1 and S_2 – located within the desert region as the starting and ending points. On the trajectory from S_1 to S_2, we analyze the discrepancies between c_{Y22} and c_{ZS14}, as well as between $F_{d,ZS14}$ and $F_{d,Y22}$. At the starting point, the values of c_{Y22} and c_{ZS14} are nearly identical, but their difference becomes more pronounced as we move toward the endpoint. Since the effects of the ABL on dust deposition velocity are commonly observed under unstable conditions, we proceed to compare the dust deposition fluxes and simulated dust concentrations using two schemes under the convective ABLs. To obtain data in convective ABLs, we exclusively consider time points at 5 UTC, 6 UTC, 7 UTC, and 8 UTC for each day in June, July, and August. These UTC times correspond to the local times of 11:00, 12:00, 13:00, and 14:00, respectively. Subsequently, we calculate the average dust deposition flux and dust concentration under these unstable conditions. Figure 5-8a shows the variation of the averaged $F_{d,ZS14}$ and $F_{d,Y22}$ along the trajectory from the starting point to the ending point. Figure 5-8b displays the corresponding variation of the averaged c_{Y22} and c_{ZS14}. Upon analysis, we observe that at the starting point, the deposition flux simulated by the Y22 scheme is around 0.052 µg m^{-2} s^{-1}, and is larger than the deposition flux calculated by the scheme of ZS14, which is about 0.032 µg m^{-2} s^{-1}. The relative difference amounts to approximately 38.5%. As we progress in distance, c_{Y22} decreases at a quicker rate compared to c_{ZS14}, leading to an escalating difference between them. Consequently, this may lead to $F_{d,ZS14}$ becoming larger than $F_{d,Y22}$.

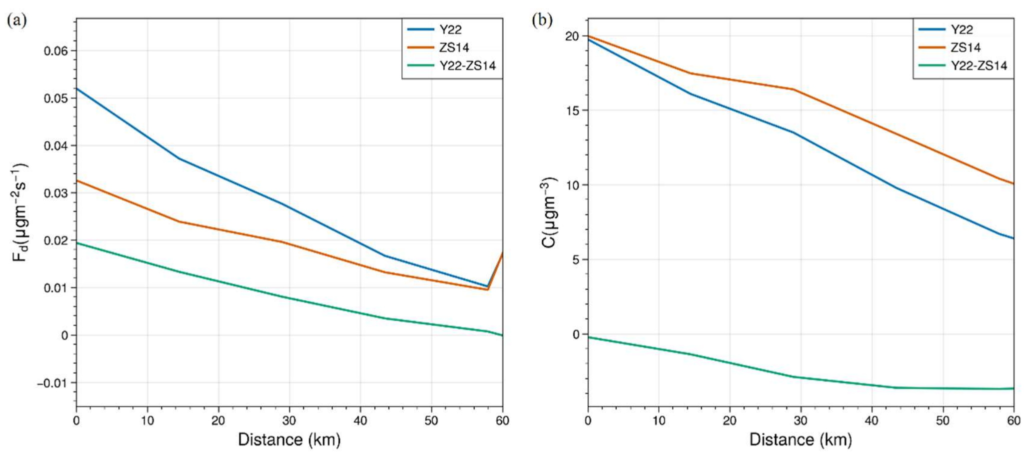

Figure 5-8: Comparison of the dust deposition flux predicted by the ZS14 scheme and the Y22 scheme at the location of the starting point (95.24 ºE, 40.081 ºN) and a downwind ending point (95.02º E, 37.405º N) along the trajectory.

Figure 5-9a illustrates the vertical dust concentration profiles at different distances: 0 km, 0.14 km, 0.29 km, 0.43 km and 0.58 km from the starting point S_1. It's evident that both c_{ZS14} and c_{Y22} almost remain constant in the vertical direction to about 1000 m. In addition, Figure 5-9a shows that both c_{ZS14} and c_{Y22} decrease with distance from the starting point. Simultaneously, the discrepancy between them, Δc, increases with distance, as depicted in Figure 5-9b. This phenomenon arises because the deposition velocity obtained using the Y22 scheme $V_{d,Y22}$ is larger than the ZS14 scheme $V_{d,ZS14}$, leading to greater dust deposition and subsequently lowering the airborne dust concentration. Furthermore, this leads to a decreased amount of dust suspended in the air, resulting in a diminished concentration of dust being transported forward by the wind.

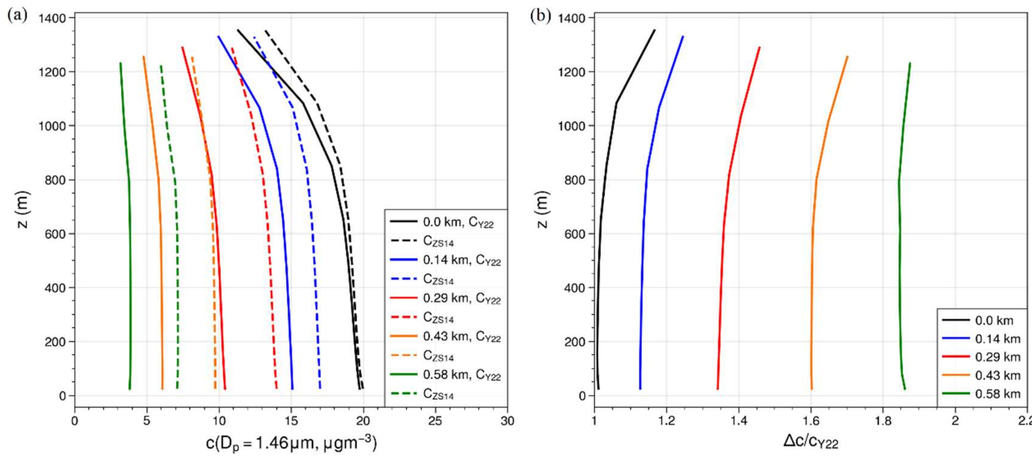

Figure 5-9: (a) The vertical profiles of dust ($D_p = 1.46$ μm) concentrations obtained by using the ZS14 scheme (dashed lines) and the Y22 scheme (solid lines) at different locations. (b) The vertical profiles of the relative difference between the two concentrations at different locations.

Using the same method, Figure 5-10 shows the one-hour accumulated dust deposition mass for dust particles with $D_p = 1.46$ μm . Here, the accumulated dust deposition mass is defined as the deposition output flux at each simulation time step multiplied by the time step (in seconds) and then superimposed to obtain the flux integral. In general, Figure 5-10 shows the same changing pattern as Figure 5-8a.

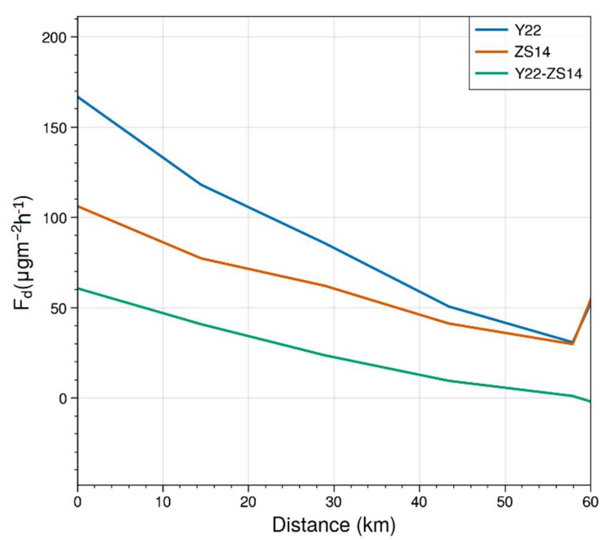

Figure 5-10: Same as Figure 5-9(a), but for accumulated dust deposition.

5.3 Conclusion

In this chapter, I incorporate the dust deposition schemes of Y22 and ZS14 into WRF-Chem to calculate both the dust deposition velocity and the dust deposition flux. While the Y22 scheme takes into account the distribution of surface shear stress, the ZS14 scheme solely considers the Reynolds shear stress. Based on the simulations, the differences in the dust deposition velocity between these two schemes are compared. Furthermore, I contrast the simulated monthly dust deposition results with in-situ observational data from the Shapotou district. Additionally, the dust deposition flux and dust concentration along a wind trajectory are also described. The main findings of this study can be summarized as follows:

1) $\Delta V_d \left(\text{i.e. } V_{d,\,Y22} - V_{d,\,ZS14}\right)$ is greater under convective conditions compared to neutral conditions, with the lowest value observed under steady conditions. This value is also influenced by the state of the underlying surface.
2) When considering comparable dust concentrations, the dust deposition flux calculated using the Y22 scheme is larger than the deposition flux simulated by the ZS14 scheme.

In summary, the dust deposition process is complex, and the simulation of dust deposition is influenced not only by the wind and temperature fields (reflected in turbulent surface shear stress) but also constrained by the available dust supply. Considering the effects of turbulent shear stress, the Y22 scheme simulates a larger dust deposition velocity than the ZS14 scheme. However, as the simulated dust deposition fluxes still remain significantly lower than the observed data, the application of the Y22 scheme to long-term (e.g. monthly) dust deposition simulations needs further investigation.

6. Summary and conclusion

6.1 Summary

Although an increase in dust deposition velocity is commonly observed in convective ABLs, the current numerical models fail to replicate this phenomenon. Furthermore, there are no hypotheses that can be experimentally or numerically tested to explain this enhancement. Therefore, the main objective of this thesis is to propose a method for quantifying the increased dust deposition velocity under convective ABL conditions and to bridge the gap between the currently employed deposition schemes and observational data.

The dust deposition through eddy diffusion is parametrized using surface shear stress. However, due to the stochastic nature of surface shear stress and its moments, it is significantly influenced by ABL stability. In this study, it is assumed that the turbulent surface shear stress should be considered in the dust deposition scheme. As a result, the following four objectives within the framework of this thesis should be addressed:

1) Investigating the relationship between surface shear stress and both ABL stability and background wind conditions
2) Developing a new dust deposition scheme that considers the effects of ABL stability
3) Evaluating the performance and effectiveness of the newly developed dust deposition scheme through comprehensive comparisons with observational data
4) Implementing the refined dust deposition scheme into a regional atmospheric model

In this study, all four of the aforementioned research objectives were successfully addressed and investigated within the confines of this thesis. The effects of ABL stability on the surface shear stress were thoroughly investigated through numerical experiments. A new dust deposition scheme was formulated, taking into consideration the stochastic nature of the dust deposition process. The proposed scheme was validated against field and wind tunnel observations to ensure its accuracy and reliability. Subsequently, the scheme was successfully implemented into a regional atmospheric model. Moving forward, Section 6.2 provides a concise summary of the main findings of this thesis.

Section 6.3 discusses the limitations encountered throughout the study. Finally, this thesis concludes with Section 6.4, which offers a research outlook.

6.2 Main achievements

1) By resolving the high-resolution large eddies with WRF-LES/D, the value of stochastic surface shear stress exhibits greater fluctuations under convective conditions compared to neutral and stable conditions.

2) The instantaneous surface shear stresses differ significantly from Reynolds shear stresses, and the probability density distribution of the instantaneous shear stress can be described by the Weibull distribution function.

3) The shape and scale parameters of the Weibull distribution can be directly estimated from macroscopic atmospheric variables, which are available diagnostic quantities in regional atmospheric models. In particular, the shape parameter of the Weibull distribution decreases exponentially as the magnitude of the reciprocal of the Obukhov length, denoted as $|L_o^{-1}|$, increases. The scale parameter increases linearly as a function of the Reynolds shear stress u_* and the vertical scaling velocity w_*.

4) The probability density distribution of the instantaneous shear stress at various heights below 50 m is also observed to follow a Weibull distribution. The scale parameter increases with ascending height.

5) A new deposition scheme, named the Y22 scheme, is proposed, which is founded on the statistic of instantaneous deposition velocity. In contrast to the ZS14 scheme, which relies only on Reynolds shear stress, the new Y22 scheme describes the dust deposition velocity by considering the stochastic nature of the surface shear stress.

6) Under convective conditions, the dust deposition velocity from the Y22 scheme, $V_{d,\mathrm{Y22}}$, is larger than that of the ZS14 scheme, $V_{d,\,zs14}$. The difference between the two increases with increasing ABL instability. Under strong convective conditions on the sand surface, the relative difference between the Y22 scheme and the simulation can be reduced from approximately 50% to around 10% compared to the ZS14 scheme.

7) When comparing the performance of the Y22 scheme and the ZS14 scheme within the weather scale model WRF, the Y22 scheme predicts a higher dust deposition

velocity under convective conditions compared to the ZS14 scheme. Consequently, when dust concentrations within the simulated grid exhibit similar magnitude for both schemes, the Y22 scheme results in a larger simulated dust deposition flux compared to the ZS14 scheme.

In conclusion, a new parameterization scheme for turbulent dust deposition under convective conditions has been successfully developed. The new scheme is applicable at the large-eddy scale and requires specific input parameters, including u_*, w_*, L_O, $\overline{\theta}$ and land-use types, and no more new input parameters than previous dust deposition schemes. This project is the first comprehensive investigation of the turbulent characteristics of particle deposition, and its findings will be of interest to improve the accuracy of particle deposition predictions on regional or global scales.

6.3 Discussion

The Y22 scheme is proposed based on the WRF-LES/D simulations, utilizing a homogeneous surface with a monotype of obstacle. However, in nature, non-homogeneous surfaces are more common, characterized by non-uniform distributions of roughness elements or a mixture of multiple-sized roughness elements in a single area. Unfortunately, this study does not include testing the Y22 scheme on inhomogeneous surfaces.

While atmospheric turbulence over sand, grass, and water surfaces with specified roughness length is thoroughly tested in this thesis, the simulation and momentum parameterization of atmospheric turbulence for other land-use categories have not been investigated. Consequently, the coefficients used in the formulas for calculating the scale parameter and shape parameter may not be applicable to land-use types other than sand, grass, and water surfaces. Thus, the applicability of the Y22 scheme is limited to situations where the land-use category falls within these three types and is also homogeneous. Further research and validation would be necessary to extend the scheme's usability to non-homogeneous surfaces and different land-use categories.

In addition, the application of the MOST to WRF-LES/D poses challenges due to several reasons (Shao et al., 2013). Firstly, the derivation of MOST assumes horizontal homogeneity with negligible advection effects. However, at the large-eddy scale, these assumptions may not hold. The MOST similarity functions are empirically derived using averaged boundary-layer measurements, typically over 15 to 30 min or several kilometers. This study cannot precisely determine the altitude range of atmospheric turbulence affected by the application of the MOST.

Regarding the application of the Y22 scheme in WRF, it successfully reproduces the enhancement in dust deposition velocity in the convective ABL. However, it underestimates dust deposition on longer timescales. This discrepancy occurs because the high dust deposition velocity leads to a reduction in simulated dust concentration. The dust deposition rates calculated using the Y22 scheme encompass two contributions: a Weibull distribution of instantaneous shear stress and the value of the ZS14 scheme within that distribution. Consequently, if the range of variation of the instantaneous shear stress specified to generate the Weibull distribution is too extensive, it could result in several unreliable dust deposition values. Additionally, when applying the ZS14 scheme to WRF-Chem, the parameterizations used in it require careful calibration.

6.4 Outlook

The limitations identified in the above discussion suggest several priorities for future research:

1) The current horizontal grid resolution used in this study is 10 m. To advance the research, it is essential to evaluate the impact of varying grid resolutions on the stress distribution results and the newly developed deposition scheme.

2) The parameters utilized in the ZS14 scheme should be further tested for more land-use categories. Additionally, it is crucial to calculate the atmospheric momentum distribution models for a broader range of land-use categories using WRF-LES/D.

3) For the application of the Y22 scheme to regional-scale dust calculations, it is necessary to confine the range of variation in surface shear stresses calculated using the Weibull distribution within the simulation grid.

By addressing these priorities, future research can build upon the current study's findings and contribute to a more comprehensive understanding of dust deposition processes in various atmospheric conditions and land-use scenarios.

Reference

Bergametti, G., Marticorena, B., Rajot, J. L., Foret, G., Alfaro, S. C. and Laurent, B.: Size-Resolved Dry Deposition Velocities of Dust Particles: In Situ Measurements and Parameterizations Testing, J. Geophys. Res. Atmos., 123(19), 11,080-11,099, doi:10.1029/2018JD028964, 2018.

Boucher, O., Randall, D., Artaxo, P., Bretherton, C., Feingold, G., Forster, P., Kerminen, V., Kondo, Y., Liao, H., Lohmann, U., Rasch, P., Satheesh, S., Sherwood, S., Stevens, B. and Zhang, X.: Clouds and Aerosols. Contribution of Working Group I to the Fifth Assessment Report of the Intergovernmental Panel on Climate Change., 2013.

Broecker, W. S. and Henderson, G. M.: The sequence of events surrounding Termination II and their implications for the cause of glacial-interglacial CO2 changes, Paleoceanography, 13(4), doi:10.1029/98PA00920, 1998.

Burba, G., Madsen, R. and Feese, K.: Eddy covariance method for CO2 emission measurements in CCUS applications: Principles, instrumentation and software, in Energy Procedia, vol. 40., 329-336, 2013.

Buseck, P. R. and Schwartz, S. E.: Tropospheric Aerosols, in Treatise on Geochemistry: Second Edition, vol. 5., 2013.

Businger, J. A.: Evaluation of the accuracy with which dry deposition can be measured with current micrometeorological techniques., J. Clim. Appl. Meteorol., 25(8), 1100–1124, doi:10.1175/1520-0450(1986)025<1100:EOTAWW>2.0.CO;2, 1986.

Chamberlain, A. C.: Deposition of airborne radioiodine vapor, Nucleonics, 8, 22–25, 1953.

Chamberlain, A. C.: Transport of Lycopodium spores and other small particles to rough surfaces, Proc. R. Soc. London. Ser. A. Math. Phys. Sci., 296, 45–70, doi:10.1098/rspa.1967.0005, 1967.

Chow, F. K. and Moin, P.: A further study of numerical errors in large-eddy simulations, J. Comput. Phys., 184(2), doi:10.1016/S0021-9991(02)00020-7, 2003.

Colella, K. J. and Keith, W. L.: Measurements and scaling of wall shear stress fluctuations, Exp. Fluids, 34(2), 253–260, doi:10.1007/s00348-002-0552-2, 2003.

Cottet, G. H., Jiroveanu, D. and Michaux, B.: Vorticity dynamics and turbulence models for Large-Eddy Simulations, Math. Model. Numer. Anal., 37(1), doi:10.1051/m2an:2003013, 2003.

Csanady, G. T.: Turbulent Diffusion of Heavy Particles in the Atmosphere, J. Atmos. Sci., 20, 201–208, doi:10.1175/1520-0469(1964)021<0322:codohp>2.0.co;2, 1963.

Damay, P.: Détermination expérimentale de la vitesse de dépôt sec des aérosols submicroniques en milieu naturel : influence de la granulométrie , des paramètres micrométéorologiques et du couvert. Thèse de Doctorat, Université de Rouen, 2010.

Damay, P. E., Maro, D., Coppalle, A., Lamaud, E., Connan, O., Hébert, D., Talbaut, M. and Irvine, M.: Size-resolved eddy covariance measurements of fine particle vertical fluxes, J. Aerosol Sci., 40(12), 1050–1058, doi:10.1016/j.jaerosci.2009.09.010, 2009.

Davidson, C. I., Miller, J. M. and Pleskow, M. A.: The influence of surface structure on predicted particle dry deposition to natural grass canopies, Water. Air. Soil Pollut., 18(1–3), doi:10.1007/BF02419401, 1982.

Deardorff, J. W.: A numerical study of three-dimensional turbulent channel flow at large Reynolds numbers, J. Fluid Mech., 41(2), doi:10.1017/S0022112070000691, 1970.

Deardorff, J. W.: Numerical Investigation of Neutral and Unstable Planetary Boundary Layers, J. Atmos. Sci., 29(1), doi:10.1175/1520-0469(1972)029<0091:nionau>2.0.co;2, 1972.

Deardorff, J. W.: Stratocumulus-capped mixed layers derived from a three-dimensional model, Boundary-Layer Meteorol., 18(4), 495–527, doi:10.1007/BF00119502, 1980.

Droppo, J. G.: Improved Formulations for Air-Surface Exchanges Related to National Security Needs: Dry Deposition Models., Pacific Northwest National Lab. (PNNL), Richland, WA (United States), 2006.

Fick, A.: V. On liquid diffusion , London, Edinburgh, Dublin Philos. Mag. J. Sci., 10(63), doi:10.1080/14786445508641925, 1855.

Fowler, D., Pilegaard, K., Sutton, M. A., Ambus, P., Raivonen, M., Duyzer, J., Simpson, D., Fagerli, H., Fuzzi, S., Schjoerring, J. K., Granier, C., Neftel, A., Isaksen, I. S. A., Laj, P., Maione, M., Monks, P. S., Burkhardt, J., Daemmgen, U., Neirynck, J., Personne, E., Wichink-Kruit, R., Butterbach-Bahl, K., Flechard, C., Tuovinen, J. P., Coyle, M., Gerosa, G., Loubet, B., Altimir, N., Gruenhage, L., Ammann, C., Cieslik, S., Paoletti, E., Mikkelsen, T. N., Ro-Poulsen, H., Cellier, P., Cape, J. N., Horváth, L., Loreto, F., Niinemets, Ü., Palmer, P. I., Rinne, J., Misztal, P., Nemitz, E., Nilsson, D., Pryor, S., Gallagher, M. W., Vesala, T., Skiba, U., Brüggemann, N., Zechmeister-Boltenstern, S., Williams, J., O'Dowd, C., Facchini, M. C., de Leeuw, G., Flossman, A., Chaumerliac, N. and Erisman, J. W.: Atmospheric composition change: Ecosystems-Atmosphere interactions, Atmos. Environ., 43(33), 5193–5267, doi:10.1016/j.atmosenv.2009.07.068, 2009.

Gallagher, M. W., Beswick, K. M., Duyzer, J., Westrate, H., Choularton, T. W. and Hummelshøj, P.: Measurements of aerosol fluxes to speulderforest using a micrometeorological technique, Atmos. Environ., 31(3), 359–373, doi:10.1016/S1352-2310(96)00057-X, 1997.

Garratt, J. R.: Review: the atmospheric boundary layer, Earth Sci. Rev., 37(1–2), doi:10.1016/0012-8252(94)90026-4, 1994.

Gieré, R. and Querol, X.: Solid particulate matter in the atmosphere, Elements, 6(4), doi:10.2113/gselements.6.4.215, 2010.

Giorgi, F.: A particle dry-deposition parameterization scheme for use in tracer transport models, J. Geophys. Res., doi:10.1029/jd091id09p09794, 1986.

Gregory, P. H.: The dispersion of air-borne spores, Trans. Br. Mycol. Soc., 28(1–2), 26–72, doi:10.1016/s0007-1536(45)80041-4, 1945.

Grell, G. A. and Freitas, S. R.: A scale and aerosol aware stochastic convective parameterization for weather and air quality modeling, Atmos. Chem. Phys., 14(10), doi:10.5194/acp-14-5233-2014, 2014.

Grell, G. A., Peckham, S. E., Schmitz, R., McKeen, S. A., Frost, G., Skamarock, W. C. and Eder, B.: Fully coupled "online" chemistry within the WRF model, Atmos. Environ., 39(37), doi:10.1016/j.atmosenv.2005.04.027, 2005.

Heinold, B., Tegen, I., Schepanski, K., Tesche, M., Esselborn, M., Freudenthaler, V., Gross, S., Kandler, K., Knippertz, P., Müller, D., Schladitz, A., Toledano, C., Weinzierl, B., Ansmann, A., Althausen, D., Müller, T., Petzold, A. and Wiedensohler, A.: Regional modelling of Saharan dust and biomass-burning smoke: Part I: Model description and evaluation, Tellus, Ser. B Chem. Phys. Meteorol., 63(4), doi:10.1111/j.1600-0889.2011.00570.x, 2011.

Hicks, B. B.: Dry deposition of acid particles to natural surfaces., Environmental Science Research. Springer, Boston, MA, 1979.

Hicks, B. B., Baldocchi, D. D., Meyers, T. P., Hosker, R. P. and Matt, D. R.: A preliminary multiple resistance routine for deriving dry deposition velocities from measured quantities, Water. Air. Soil Pollut., 36(3–4), doi:10.1007/BF00229675, 1987.

Hicks, B. B., Saylor, R. D. and Baker, B. D.: Dry deposition of particles to canopies-A look back and the road forward, J. Geophys. Res., 121(24), 14691–14707, doi:10.1002/2015JD024742, 2016.

Hinds, W. C.: Aerosol technology: properties, behaviour, and measurement of airborne particles., 1982.

Hong, S. Y., Noh, Y. and Dudhia, J.: A new vertical diffusion package with an explicit treatment of entrainment processes, Mon. Weather Rev., 134(9), doi:10.1175/MWR3199.1, 2006.

Hummelshøj, P., Jensen, N. O. and Larsen, S. E.: Particle dry deposition to a sea surface, Precip. Scav. Atmos. Exch. Hemisph. Publ. Corp. Washingt., 5562, 829–840, 1992.

Iacono, M. J., Delamere, J. S., Mlawer, E. J., Shephard, M. W., Clough, S. A. and Collins, W. D.: Radiative forcing by long-lived greenhouse gases: Calculations with the AER radiative transfer models, J. Geophys. Res. Atmos., 113(13), doi:10.1029/2008JD009944, 2008.

Jickells, T. D., An, Z. S., Andersen, K. K., Baker, A. R., Bergametti, C., Brooks, N., Cao, J. J., Boyd, P. W., Duce, R. A., Hunter, K. A., Kawahata, H., Kubilay, N., LaRoche, J., Liss, P. S., Mahowald, N., Prospero, J. M., Ridgwell, A. J., Tegen, I. and Torres, R.: Global iron connections between desert dust, ocean biogeochemistry, and climate, Science (80-.)., 308(5718), doi:10.1126/science.1105959, 2005.

Kaimal, J. C. and Finnigan, J. J.: Atmospheric boundary layer flows: their structure and measurement, Oxford university press., New York, 1994.

Kawamura, R.: Study of sand movement by wind., University of Clifornia Hydraulic Engineering Laboratory, 1964.

Kind, R. J.: One-dimensional aeolian suspension above beds of loose particles-A new concentration-profile equation, Atmos. Environ. Part A, Gen. Top., 26(5), 927–931, doi:10.1016/0960-1686(92)90250-O, 1992.

Klose, M. and Shao, Y.: Large-eddy simulation of turbulent dust emission, Aeolian Res., 8, 49–58, doi:10.1016/j.aeolia.2012.10.010, 2013.

Klose, M., Shao, Y., Li, X., Zhang, H., Ishizuka, M., Mikami, M. and Leys, J. F.: Further development of a parameterization for convective turbulent dust emission and evaluation based on field observations, J. Geophys. Res., 119(17), 10441–10457, doi:10.1002/2014JD021688, 2014.

Kolmogorov, A. N.: Dissipation of energy in the locally isotropic turbulence, Proc. R. Soc. London. Ser. A Math. Phys. Sci., 434(1890), 15–17, 1991.

Lamaud, E., Chapuis, A., Fontan, J. and Serie, E.: Measurements and parameterization of aerosol dry deposition in a semi-arid area, Atmos. Environ., 28(15), 2461–2471, doi:10.1016/1352-2310(94)90397-2, 1994.

Leonard, A.: Energy cascade in large-eddy simulations of turbulent fluid flows, Adv. Geophys., 18(PA), 237–248, doi:10.1016/S0065-2687(08)60464-1, 1975.

Li, G., Zhang, J., Herrmann, H. J., Shao, Y. and Huang, N.: Study of Aerodynamic Grain Entrainment in Aeolian Transport, Geophys. Res. Lett., 47(11), e2019GL086574, doi:https://doi.org/10.1029/2019GL086574, 2020.

Liu, B. Y. H. and Agarwal, J. K.: Experimental observation of aerosol deposition in turbulent flow, J. Aerosol Sci., 5(2), doi:10.1016/0021-8502(74)90046-9, 1974.

Liu, D., Ishizuka, M., Mikami, M. and Shao, Y.: Turbulent characteristics of saltation and uncertainty of saltation model parameters, Atmos. Chem. Phys., 18(10), 7595–7606, doi:10.5194/acp-18-7595-2018, 2018.

Liu, S., Shao, Y., Hintz, M. and Lennartz-Sassinek, S.: Multiscale decomposition for heterogeneous land-atmosphere systems, J. Geophys. Res., 120(3), doi:10.1002/2014JD022258, 2015.

Lovett, G. M.: Atmospheric deposition of nutrients and pollutants in North America: An ecological perspective, Ecol. Appl., 4(4), doi:10.2307/1941997, 1994.

Mahowald, N. M., Engelstaedter, S., Luo, C., Sealy, A., Artaxo, P., Benitez-Nelson, C., Bonnet, S., Chen, Y., Chuang, P. Y., Cohen, D. D., Dulac, F., Herut, B., Johansen, A. M., Kubilay, N., Losno, R., Maenhaut, W., Paytan, A., Prospero, J. M., Shank, L. M. and Siefert, R. L.: Atmospheric iron deposition: Global distribution, variability, and human perturbations, Ann. Rev. Mar. Sci., 1, doi:10.1146/annurev.marine.010908.163727, 2009.

Malcolm, L. P. and Raupach, M. R.: Measurements in an air settling tube of the terminal velocity distribution of soil material, J. Geophys. Res., 96, 15,275-15,286, 1991.

Martin, J. H., Coale, K. H., Johnson, K. S., Fitzwater, S. E., Gordon, R. M., Tanner, S. J., Hunter, C. N., Elrod, V. A., Nowicki, J. L., Coley, T. L., Barber, R. T., Lindley, S., Watson, A. J., Van Scoy, K., Law, C. S., Liddicoat, M. I., Ling, R., Stanton, T., Stockel, J., Collins, C., Anderson, A., Bidigare, R., Ondrusek, M., Latasa, M., Millero, F. J., Lee, K., Yao, W., Zhang, J. Z., Friederich, G., Sakamoto, C., Chavez, F., Buck, K., Kolber, Z., Greene, R., Falkowski, P., Chisholm, S. W., Hoge, F., Swift, R., Yungel, J., Turner, S., Nightingale, P., Hatton, A., Liss, P. and Tindale, N. W.: Testing the iron hypothesis in ecosystems of the equatorial Pacific Ocean, Nature, 371(6493), doi:10.1038/371123a0, 1994.

Meyers, J. and Sagaut, P.: Evaluation of Smagorinsky variants in large-eddy simulations of wall-resolved plane channel flows, Phys. Fluids, 19(9), doi:10.1063/1.2768944, 2007.

Monahan, A. H.: The probability distribution of sea surface wind speeds. Part I: Theory and SeaWinds observations, J. Clim., 19(4), 497–520, doi:10.1175/JCLI3640.1, 2006.

Monin, A. S.: The Atmospheric Boundary Layer, Annu. Rev. Fluid Mech., 2(1), 225–250, doi:10.1146/annurev.fl.02.010170.001301, 1970.

Monin, A. S. and Obukhov, A. M.: Basic Laws of Turbulence Mixing in the Ground Layer of the Atmosphere, Tr. Akad. Nauk. SSSR Geophiz. Inst., 24(151), 1954.

Monin, A. S. and Yaglom, A. M.: Statistical Fluid Mechanics, Volume II: mechanics of turbulence, Courier Corporation, 2013.

Montgomery, R. B.: VERTICAL EDDY FLUX OF HEAT IN THE ATMOSPHERE, J. Meteorol., 5(6), doi:10.1175/1520-0469(1948)005<0265:vefohi>2.0.co;2, 1948.

Morrison, H., Thompson, G. and Tatarskii, V.: Impact of cloud microphysics on the development of trailing stratiform precipitation in a simulated squall line: Comparison of one- and two-moment schemes, Mon. Weather Rev., 137(3), doi:10.1175/2008MWR2556.1, 2009.

Nemitz, E. and Sutton, M. A.: Gas-particle interactions above a Dutch heathland: III. Modelling the influence of the NH₃-HNO₃-NH₄NO₃ equilibrium on size-segregated particle fluxes, Atmos. Chem. Phys., 4(4), 1025–1045, doi:10.5194/acp-4-1025-2004, 2004.

Obukhov, A. M.: Characteristics of the micro-structure of the wind in the surface layer of the atmosphere, Izv AN SSSR, ser Geofiz, 3, 1951.

Okin, G. S., Mahowald, N., Chadwick, O. A. and Artaxo, P.: Impact of desert dust on the biogeochemistry of phosphorus in terrestrial ecosystems, Global Biogeochem. Cycles, 18(2), doi:10.1029/2003GB002145, 2004.

Pellerin, G., Maro, D., Damay, P., Gehin, E., Connan, O., Laguionie, P., Hébert, D., Solier, L., Boulaud, D., Lamaud, E. and Charrier, X.: Aerosol particle dry deposition velocity above natural surfaces: Quantification according to the particles diameter, J. Aerosol Sci., 114, 107–117, doi:10.1016/j.jaerosci.2017.09.004, 2017.

Peters, K. and Eiden, R.: Modelling the dry deposition velocity of aerosol particles to a spruce forest, Atmos. Environ. Part A, Gen. Top., 26(14), doi:10.1016/0960-1686(92)90108-W, 1992.

Petroff, A. and Zhang, L.: Development and validation of a size-resolved particle dry deposition scheme for application in aerosol transport models, Geosci. Model Dev., doi:10.5194/gmd-3-753-2010, 2010.

Petroff, A., Mailliat, A., Amielh, M. and Anselmet, F.: Aerosol dry deposition on vegetative canopies. Part I: Review of present knowledge, Atmos. Environ., 42(16), 3625–3653, doi:10.1016/j.atmosenv.2007.09.043, 2008a.

Petroff, A., Mailliat, A., Amielh, M. and Anselmet, F.: Aerosol dry deposition on vegetative canopies. Part II: A new modelling approach and applications, Atmos. Environ., 42(16), doi:10.1016/j.atmosenv.2007.12.060, 2008b.

Pope, S. B.: Turbulent flows, Cambridge university press., 2000.

Porch, W. M.: Fast-response light scattering measurements of aerosol suspension in a desert area, Atmos. Environ., 8(9), 1974.

Rana, S., Anderson, W. and Day, M.: Turbulence-Based Model for Subthreshold Aeolian Saltation, Geophys. Res. Lett., 47(15), 1–9, doi:10.1029/2020GL088050, 2020.

Raupach, M. R.: Drag and drag partition on rough surfaces, Boundary-Layer Meteorol., 60(4), 375–395, doi:10.1007/BF00155203, 1992.

Rauterkus, R.: Large eddy simulation of arctic stratocumulus. Ph.D. thesis, Universität zu Köln, Germany, 2021.

Robinson, S. K.: Coherent motions in the turbulent boundary layer, Annu. Rev. Fluid Mech., 23(1), doi:10.1146/annurev.fl.23.010191.003125, 1991.

Rosenfeld, D., Rudich, Y. and Lahav, R.: Desert dust suppressing precipitation: A possible desertification feedback loop, Proc. Natl. Acad. Sci. U. S. A., 98(11), doi:10.1073/pnas.101122798, 2001.

Schmitt, F. G.: About Boussinesq's turbulent viscosity hypothesis: historical remarks and a direct evaluation of its validity, Comptes Rendus - Mec., 335(9–10), doi:10.1016/j.crme.2007.08.004, 2007.

Sehmel, G. A.: Particle and gas dry deposition: A review, Atmos. Environ., 14(9), 983–1011, doi:10.1016/0004-6981(80)90031-1, 1980.

Seinfeld, J. H. and Pandis, S. N.: Atmospheric chemistry and physics: from air pollution to climate change, 2nd Edition, John Wiley & Sons., New York, 2006.

Seinfeld, J. H., Bretherton, C., Carslaw, K. S., Coe, H., DeMott, P. J., Dunlea, E. J., Feingold, G., Ghan, S., Guenther, A. B., Kahn, R., Kraucunas, I., Kreidenweis, S. M., Molina, M. J., Nenes, A., Penner, J. E., Prather, K. A., Ramanathan, V., Ramaswamy, V., Rasch, P. J., Ravishankara, A. R., Rosenfeld, D., Stephens, G. and Wood, R.: Improving our fundamental understanding of the role of aerosol–cloud interactions in the climate system, Proc. Natl. Acad. Sci., 113(21), 5781–5790, doi:10.1073/PNAS.1514043113, 2016.

Shao, Y.: Physics and Modelling of Wind Erosion., Springer Netherlands, 2008.

Shao, Y. and Yang, Y.: A theory for drag partition over rough surfaces, J. Geophys. Res. Earth Surf., 113(2), 1–9, doi:10.1029/2007JF000791, 2008.

Shao, Y., Wyrwoll, K. H., Chappell, A., Huang, J., Lin, Z., McTainsh, G. H., Mikami, M., Tanaka, T. Y., Wang, X. and Yoon, S.: Dust cycle: An emerging core theme in Earth system science, Aeolian Res., 2(4), 181–204, doi:10.1016/j.aeolia.2011.02.001, 2011a.

Shao, Y., Ishizuka, M., Mikami, M. and Leys, J. F.: Parameterization of size-resolved dust emission and validation with measurements, J. Geophys. Res. Atmos., 116(8), doi:10.1029/2010JD014527, 2011b.

Shao, Y., Liu, S., Schween, J. H. and Crewell, S.: Large-Eddy Atmosphere-Land-Surface Modelling over Heterogeneous Surfaces: Model Development and Comparison with Measurements, Boundary-Layer Meteorol., 148(2), 333–356, doi:10.1007/s10546-013-9823-0, 2013.

Shao, Y., Zhang, J., Ishizuka, M., Mikami, M., Leys, J. and Huang, N.: Dependency of particle size distribution at dust emission on friction velocity and atmospheric boundary-layer stability, Atmos. Chem. Phys., 20(21), 12939–12953, doi:10.5194/acp-20-12939-2020, 2020.

Skamarock, W. C., Klemp, J. B., Dudhi, J., Gill, D. O., Barker, D. M., Duda, M. G., Huang, X.-Y., Wang, W. and Powers, J. G.: A Description of the Advanced Research WRF Version 3, Tech. Rep., (June), 113, doi:10.5065/D6DZ069T, 2008.

Slinn, S. A. and Slinn, W. G. N.: Predictions for particle deposition on natural waters, Atmos. Environ., 14(9), 1013–1016, doi:10.1016/0004-6981(80)90032-3, 1980.

Slinn, W. G. N.: Predictions for particle deposition to vegetative canopies, Atmos. Environ., 16(7), 1785–1794, doi:10.1016/0004-6981(82)90271-2, 1982.

Smagorinsky, J.: General circulation experiments with the primitive equations, Mon. Weather Rev., 91(3), doi:10.1175/1520-0493(1963)091<0099:gcewtp>2.3.co;2, 1963.

Sokolik, I. N. and Toon, O. B.: Direct radiative forcing by anthropogenic airborne mineral aerosols, Nature, 381(6584), doi:10.1038/381681a0, 1996.

Sportisse, B.: A review of current issues in air pollution modeling and simulation, Comput. Geosci., 11(2), doi:10.1007/s10596-006-9036-4, 2007.

Stull, R. B.: An introduction to boundary layer meteorology, Springer Netherlands, doi:10.1007/978-94-009-3027-8, 1988.

Swinbank, W. C.: The measurement of vertical transfer of heat and water vapor by eddies in the lower atmosphere, J. Atmos. Sci., 8(3), 135-145, doi:10.1175/1520-0469(1951)008<0135:tmovto>2.0.co;2, 1951.

Tegen, I. and Lacis, A. A.: Modeling of particle size distribution and its influence on the radiative properties of mineral dust aerosol, J. Geophys. Res. Atmos., 101(14), doi:10.1029/95jd03610, 1996.

Venkatram, A. and Pleim, J.: The electrical analogy does not apply to modeling dry deposition of particles, Atmos. Environ., 33(18), 3075–3076, doi:10.1016/S1352-2310(99)00094-1, 1999.

Voldner, E. C. and Sirois, A.: Monthly mean spatial variations of dry deposition velocities of oxides of sulphur and nitrogen, Water. Air. Soil Pollut., 30(1–2), doi:10.1007/BF00305187, 1986.

Walcek, C. J. and Taylor, G. R.: Theoretical Method for Computing Vertical Distributions of Acidity and Sulfate Production Within Cumulus Clouds., J. Atmos. Sci., 43(4), 339–355, doi:10.1175/1520-0469(1986)043<0339:ATMFCV>2.0.CO;2, 1986.

Walcek, C. J., Brost, R. A., Chang, J. S. and Wesely, M. L.: SO2, sulfate and HNO3 deposition velocities computed using regional landuse and meteorological data, Atmos. Environ., 20(5), 949–964, doi:10.1016/0004-6981(86)90279-9, 1986.

Wesely, M. L. and Hicks, B. B.: Dry deposition and emission of small particles at the surface of the earth, Conference: 4. symposium on turbulence, diffusion and air pollution, Reno, NV, United States, 1979.

Wesely, M. L., Hicks, B. B., Dannevik, W. P., Frisella, S. and Husar, R. B.: An eddy-correlation measurement of particulate deposition from the atmosphere, Atmos. Environ., 11(6), doi:10.1016/0004-6981(77)90076-2, 1977.

Wesely, M. L., Cook, D. R. and Hart, R. L.: Fluxes of gases and particles above a deciduous forest in wintertime, Boundary-Layer Meteorol., 27(3), 237–255, doi:10.1007/BF00125000, 1983.

Wesely, M. L., Cook, D. R. and Hart, R. L.: Measurements and parameterization of particulate sulfur dry deposition over grass., J. Geophys. Res., doi:10.1029/jd090id01p02131, 1985a.

Wesely, M. L., Cook, D. R. and Hart, R. L.: Sulfur Dry Deposition Over Grass, J. Geophys. Res., 90(4), 2131–2143, 1985b.

Williams, R. M.: A model for the dry deposition of particles to natural water surfaces, Atmos. Environ., 16(8), doi:10.1016/0004-6981(82)90464-4, 1982.

Wyngaard, J. C.: Scalar fluxes in the planetary boundary layer - Theory, modeling, and measurement, Boundary-Layer Meteorol., 50(1–4), doi:10.1007/BF00120518, 1990.

Yang, Y. and Shao, Y.: A scheme for scalar exchange in the urban boundary layer, Boundary-Layer Meteorol., 120(1), 111–132, doi:10.1007/s10546-005-9033-5, 2006.

Yin, X., Jiang, C., Shao, Y., Huang, N. and Zhang, J.: Large-eddy-simulation study on turbulent particle deposition and its dependence on atmospheric-boundary-layer stability, Atmos. Chem. Phys., 22(7), 4509–4522, doi:10.5194/acp-22-4509-2022, 2022.

Zhang, J.: A Study on Dust Dry Deposition : Wind-tunnel Experiment and Improved Parameterization, Ph.D. thesis, Universität zu Köln, Germany, 2013.

Zhang, J. and Shao, Y.: A new parameterization of particle dry deposition over rough surfaces, Atmos. Chem. Phys., 14(22), 12429–12440, doi:10.5194/acp-14-12429-2014, 2014.

Zhang, L., Gong, S., Padro, J. and Barrie, L.: A size-segregated particle dry deposition scheme for an atmospheric aerosol module, Atmos. Environ., doi:10.1016/S1352-2310(00)00326-5, 2001.

Zheng, X., Jin, T. and Wang, P.: The Influence of Surface Stress Fluctuation on Saltation Sand Transport Around Threshold, J. Geophys. Res. Earth Surf., 125(5), 0–2, doi:10.1029/2019JF005246, 2020.

List of abbreviations

MOST	Monin-Obukhov Similarity Theory
WRF	Weather Research and Forecasting Model
ABL	Atmospheric boundary layer
USGS	U.S. Geological Survey
UTC	universal time code
PDF	probability density distribution
LES	large-eddy simulation
LST	local standard time
TI-V	turbulent intensity of deposition velocity
TI-S	turbulent intensity of fluctuating shear stress
SGS	subgrid scaled
ACF	autocorrelation function

List of symbols

A_{in}	empirical parameter for the micro-roughness characteristics
B_f	Brunt-Väisälä frequency [s^{-1}]
D_p	dust particle diameter [μm]
E, E_B, E_{im}, E_{in}	total, Brownian diffusion-induced, impaction-induced, and interception-induced collection efficiencies [/]
G	particle gravity [N]
$G(\vec{x}-\vec{\varsigma})$	filter function
F_d, $F_{d,T}$, $F_{d,B}$	total, eddy diffusion-induced, and molecular diffusion-induced dust deposition fluxes [kg m^2 s^{-1}]
H_0	surface heat flux [W m−2]
K_B	Boltzmann constant [J K^{-1}]
K_β	Height-Dependent Slope for Weibull Distribution's Scale Parameter
K_m, K_h, K_p	eddy viscosity for momentum, heat, and particle [m^2 s^{-1}]
L_O	Obukhov length [m]
Pr	Prandtl number
R	collection reduced by rebound
Re	Reynolds number
RE	Relative difference
Ri	gradient Richardson number
Sc, Sc_T	Schmidt number, turbulent Schmidt number
S_t	Stokes number
S_{ij}	filtered strain rate tensor [s^{-1}]
T, T_V	temperature, virtual absolute temperature [K]
T_p, $\hat{T}_p$	particle response time, dimensionless particle relaxation time [s]
TI-S	turbulent intensity of deposition velocity
TI-V	turbulent intensity of shear stress
RE	relative difference of variable X and Y
U	wind speed at top boundary of ABL [m s^{-1}]
U_a	wind speed $U_a = \left(u^2 + v^2 + w^2\right)^{1/2}$ [m s^{-1}]

U_p	dust particle velocity [m s^{-1}]
V_d	dust deposition velocity [m s^{-1}]
V_{d,τ_f}	shear stress distribution-corrected dust deposition velocity [m s^{-1}]
V_{d,τ_R}	Reynolds shear stress induced dust deposition velocity [m s^{-1}]
$V_{d,LES}$	WRF-LES/D simulated mean dust deposition velocity [m s^{-1}]
c	dust concentration [kg m^{-3}]
c_d	drag coefficient for vegetation
c_p	specific heat for moist air at constant pressure [J kg^{-1} K^{-1}]
c_u	Cunningham correction factor
c_v	viscous drag coefficient for vegetation
d_c	roughness element diameter [m]
e	subgrid turbulent kinetic energy [m^2 s^{-2}]
f	Coriolis factor
f_{drag}	aerodynamic drag [N]
g	gravitational acceleration [m s^{-2}]
k_p	molecular diffusivity [m^2 s^{-1}]
l, l_x, l_y, l_z	mixing length and mixing length in *x*-, *y*- and *z*- direction [m]
m_p	dust particle mass [kg]
p	pressure [Pa]
q	humidity [kg m^{-3}]
r	mixing ratio for unsaturated air
r_0, r_a, r_g, r_s	aerodynamic, gravitational, and surface collection resistance [s m^{-1}]
u, v, w	wind components in x-, y- and z- direction [m s^{-1}]
u_r, v_r, w_r	relative particle-to-air velocity in *x*-, *y*- and *z*- directions [m s^{-1}]
u_h	wind speed at height *h* in the roughness element layer [m s^{-1}]
u_*	friction velocity [m s^{-1}]
w_*	vertical scaling velocity [m s^{-1}]
u_*	Reynolds friction velocity [m s^{-1}]
w_t	terminal velocity [m s^{-1}]
z_0	roughness length [m]
z_l	inversion layer height [m]
z_r	reference height [m]
z_h	height of the roughness element [m]

Greek symbols

α	shape parameter in Weibull distribution
β	scale parameter in Weibull distribution
κ	von Kármán constant
γ_1	skewness of Weibull distribution
σ, σ_τ, σ_{V_d}	standard deviation of the turbulent wind, shear stress, and deposition velocity
η	fraction of cover
λ	frontal area index
λ_e	effective area index
η_{V_d}	ratio of averaged dust deposition velocity using different friction velocity distribution
λ_m	particle mean free path [m]
μ_a	dynamic viscosity of air [kg $m^{-1}s^{-1}$]
ν	kinematic viscosity of air [m^2 s^{-1}]
ϕ_m, ϕ_h	stability function for momentum and heat
ψ_m	Integral of the stability function
τ	total shear stress on the surface [m^2 s^{-2}]
τ_c	pressure drag on roughness elements [m^2 s^{-2}]
τ_R	Reynolds shear stress in kinematic unit [m^2 s^{-2}]
τ_f	instantaneous momentum flux in kinematic unit [m^2 s^{-2}]
τ_g	grid-resolved shear stress in kinematic unit [m^2 s^{-2}]
τ_{sg}	sub-grid shear stress in kinematic unit [m^2 s^{-2}]
ρ_a, ρ_p	air density, dust particle density [kg m^{-3}]
θ	potential temperature [K]
ε_{ijk}	Levi-Civita-Pseudo-Tensor
δ_{ij}	Kronecker delta
$\Re$	specific constant of air
$\overline{X}$	Reynolds-averaged value of X
X'	Turbulent component of X
$\lvert X\rvert$	absolute value of X

$\widetilde{X}$	large-eddy scale component of X
X_g	grid-resolved scale component of X
X_{sg}	sub-grid scale component of X

Acknowledgement

I thank the China Scholarship Council (CSC) for funding this work over a span of four years. Additionally, I extend my thanks to the Cologne Highly Efficient Operating Platform for Science (CHEOPS) for facilitating all the simulations carried out during this research.

A special word of gratitude goes to my supervisor, Prof. Dr. Yaping Shao. I am sincerely thankful for the invaluable opportunity to pursue my PhD candidacy under his guidance. His patient inspiration, support, and encouragement during my doctoral studies have been deeply appreciated. I am particularly grateful for the insightful discussions about my work. Prof. Dr. Shao's remarkable insights and suggestions have significantly contributed to my understanding of this research and have greatly enhanced my thesis.

I would also like to extend my heartfelt thanks to Prof. Dr. Jie Zhang for providing numerous valuable comments on my work. Thanks to my second supervisor, Prof. Dr. Ning Huang at Lanzhou University, for the support provided during the field experiments. Thanks to Dr. Eric J.R. Parteli for his help and encouragement in the early stages of this work.

Thanks to my colleagues from Prof. Dr. Yaping Shao' modelling group. Despite not spending extensive time together, your assistance during the past few years has been invaluable. Thanks to Markus Karrer, Jan Chylík, Guang Li, Jonathan Kostelecky, Andrea Burgos and José Dias for their helpful comments on my thesis. My appreciation also goes to Dr. Karin Boessenkool and Frau Dagmar Janzen for their assistance in providing the necessary documents.

I express heartfelt gratitude to my beloved husband, Cong Jiang, for his unwavering support during moments of confusion and for his uplifting encouragement during times of difficulty. I am grateful for his willingness to engage in discussions about my work, which has provided me with invaluable inspiration.

Last but not least, I extend my gratitude to my family. They are the most important people in my life, and their unwavering care and support from the very beginning have been instrumental in my journey.

Erklärung zur Dissertation

Hiermit versichere ich an Eides statt, dass ich die vorliegende Dissertation selbstständig und ohne die Benutzung anderer als der angegebenen Hilfsmittel und Literatur angefertigt habe. Alle Stellen, die wörtlich oder sinngemäß aus veröffentlichten und nicht veröffentlichten Werken dem Wortlaut oder dem Sinn nach entnommen wurden, sind als solche kenntlich gemacht. Ich versichere an Eides statt, dass diese Dissertation noch keiner anderen Fakultät oder Universität zur Prüfung vorgelegen hat; dass sie - abgesehen von unten angegebenen Teilpublikationen und eingebundenen Artikeln und Manuskripten - noch nicht veröffentlicht worden ist sowie, dass ich eine Veröffentlichung der Dissertation vor Abschluss der Promotion nicht ohne Genehmigung des Promotionsausschusses vornehmen werde. Die Bestimmungen dieser Ordnung sind mir bekannt. Darüber hinaus erkläre ich hiermit, dass ich die Ordnung zur Sicherung guter wissenschaftlicher Praxis und zum Umgang mit wissenschaftlichem Fehlverhalten der Universität zu Köln gelesen und sie bei der Durchführung der Dissertation zugrundeliegenden Arbeiten und der schriftlich verfassten Dissertation beachtet habe und verpflichte mich hiermit, die dort genannten Vorgaben bei allen wissenschaftlichen Tätigkeiten zu beachten und umzusetzen. Ich versichere, dass die eingereichte elektronische Fassung der eingereichten Druckfassung vollständig entspricht.

Köln, 11. February 2023

Xin Yin

Xin Yin

Teilpublikationen:

Erstautor Publikationen:

Yin, X., Jiang, C., Shao, Y., Huang, N. and Zhang, J.: Large-eddy-simulation study on turbulent particle deposition and its dependence on atmospheric-boundary-layer stability, Atmos. Chem. Phys., 22(7), 4509–4522, doi:10.5194/acp-22-4509-2022, 2022.

Co-Autoren Publikationen:

Jiang C., Parteli E. J. R., Xia Q., Shao Y.: A regional hydrological model for arid and semi-arid river basins with consideration of irrigation. Environmental Modelling & Software, 157(2022), 105531, doi: 10.1016/j.envsoft.2022.105531, 2022.